

WEAK LENSING AND COSMOLOGY IN THE DARK ENERGY SURVEY

Lucas Frozza Secco

A DISSERTATION

in

Physics and Astronomy

Presented to the Faculties of the University of Pennsylvania

in

Partial Fulfillment of the Requirements for the  
Degree of Doctor of Philosophy

2020

Supervisor of Dissertation



---

Dr. Bhuvnesh Jain, Walter H. and Leonore C. Annenberg Professor

Graduate Group Chairperson



---

Dr. Joshua R. Klein, Edmund J. and Louise W. Kahn Professor

Dissertation Committee:

Dr. Adam Lidz, Associate Professor

Dr. Justin Khoury, Professor

Dr. Randall Kamien, Vicki and William Abrams Professor

Dr. Gary Bernstein, Reese W. Flower Professor

# Acknowledgments

These few of pages of acknowledgements are, in fact, more important for me than the following hundred pages of equations and technical text in this thesis. I have been lucky and privileged beyond all of my expectations to meet the amazing people I have met, and to share beautiful moments with them over the past few years. This acknowledgement is for the people who were by my side, geographically close or far away, during this long journey.

First and foremost, I would like to thank Bhuvnesh Jain, my PhD advisor, collaborator and friend. For the past 5 years, Bhuv didn't only help me navigate the academic world, teach me cosmology and guide my work, he has also been a kind, humane presence which I have numerous times counted on for advice – personal as much as scientific. I consider myself lucky for having had Bhuv as a mentor and for sharing with him and his group countless scientific discussions as well as hilarious anecdotes.

I would also like to thank the cosmologists and astrophysicists from whom I learned profusely and who, in one way or another, have been my secondary mentors.

In particular, I would like to thank my seniors in the Dark Energy Survey: Scott Dodelson, Gary Bernstein & Dragan Huterer, who are, along with Bhuv, some of the great scientists I look up to, not only in terms of brilliancy but also for their exceptionally friendly nature. I'm also deeply indebted to Elisabeth Krause, Michael Troxel and Niall MacCrann, who “taught me the ropes” of weak lensing and survey science and who have been kind to share their knowledge and experience with me. I also thank, most especially, the “extended Penn group”: Eric Baxter, Carles Sanchez, Ling Lin, Vivian Miranda, Riccardo Penco, Chihway Chang, Marco Raveri, Mike Jarvis, Cyrille Doux & Amanda Farah, with whom I laughed and from whom I learned continuously, on a daily basis, for years. I deeply miss, already, meeting them just down the hall to discuss life, our scientific projects and to play more ping-pong matches than our time should have allowed.

I thank my great colleagues and friends from Philly for keeping me sane and happy, for all the board game nights, for the beers and ping-pong and chess, for the nights we went out and realized “we’re too old for this”, and, most importantly, for sharing the days when life felt more miserable than we could endure alone: Tae-hyeon Shin, Shivam Pandey, Mariana Carrillo-Gonzalez, Guram Kartvelishvili, Tasha Billings, Dillon Brout, David Sliski, Anushrut Sharma, Sean Ridout & Cathy Li.

I especially thank the Brazilian-Philadelphians who, in this foreign country where I arrived with no history and no family, made me feel safe and made me

feel like I never left home: Pedro Bernardineli, Débora Souza, Maurício Linhares, Thaís Cabral, Gustavo Silveira, Nyna Hernandez, Taís Fiorentin, Mariana Bonfim & Fernanda Novais. I'm forever indebted for the periodic doses of Caipirinha, Brazilian food and Portuguese language they offered me through the years. I also thank all the friends I left in Brazil, but with whom I never lost touch and never will, for being the distant family that never failed to burst with joy every time I flew back.

Finally, I want to thank the people who are the foundation of the man I have become, and without whom all of this would have been pointless. I thank Junran Yang, my best friend and my future wife, for the beautiful days we have spent together, for helping me up all the times I fell and for saying "yes" to spending the rest of our lives together. I also thank my family, Amauri Secco, Eleanir Secco and Luise Secco, for so many things I couldn't possibly begin to list, and therefore can only call love. I finally thank my cats, Cannoli and Whiskey, for constantly keeping things out of control and for reminding myself and Junran to never take ourselves too seriously.

I have been too lucky and too privileged. In a world with so much fear and in a time of hatred and disease, I could sit back and think of light and galaxies. I have seen the Universe while so many can't even see justice. I don't think that makes me guilty, but I do think it makes me responsible to use my knowledge for the good of all, always.

## ABSTRACT

### WEAK LENSING AND COSMOLOGY IN THE DARK ENERGY SURVEY

Lucas Frozza Secco

Bhuvnesh Jain

In this PhD Thesis, we present studies which aim at understanding and testing the fundamental assumptions of the  $\Lambda$ CDM cosmological model. We initially show that weak gravitational lensing can be derived as a consequence of General Relativity, and that it can be applied to astronomical data from the Dark Energy Survey (DES) in order to constrain the amplitude of matter fluctuations in the universe. This constraint can be used as an end-to-end cosmological test when it is compared to inferences from the Cosmic Microwave Background. We further extend the cosmological model to account for non-standard parameters which can point to novel physics, and use DES data to assess their statistical significance. We finally show that the Cold Dark Matter (CDM) paradigm can also be fundamentally tested with observational data using morphological signatures of disk galaxies in cluster environments if CDM is self-interacting.

# Contents

|  |           |
|--|-----------|
| Acknowledgements . . . . .                                     | ii        |
| Abstract . . . . .   | v         |
| <b>1 Introduction</b>  | <b>1</b>  |
| 1.1 Observational Cosmology . . . . .                          | 1         |
| 1.2 Weak Lensing . . . . .                                     | 10        |
| 1.3 The Dark Energy Survey Data . . . . .                      | 28        |
| <b>2 Weak Lensing Constraints from DES-Y1 Data</b>             | <b>33</b> |
| 2.1 A Model for the Signal . . . . .                           | 33        |
| 2.2 Systematic Uncertainties . . . . .                         | 37        |
| 2.2.1 Intrinsic Alignments . . . . .                           | 37        |
| 2.2.2 Nonlinear Power Spectrum and Baryons . . . . .           | 43        |
| 2.2.3 Point-Spread Function Modeling Errors . . . . .          | 46        |
| 2.2.4 Photometric Redshift Uncertainties . . . . .             | 49        |
| 2.2.5 Multiplicative Shear Errors . . . . .                    | 52        |
| 2.3 Covariance Matrix . . . . .                                | 53        |
| 2.4 Cosmological Constraints in $\Lambda$ CDM + wCDM . . . . . | 55        |
| <b>3 Constraints on Extended Cosmological Models</b>           | <b>66</b> |
| 3.1 Revisiting the $\Lambda$ CDM Paradigm . . . . .            | 66        |
| 3.2 Extended Cosmologies . . . . .                             | 70        |
| 3.2.1 Spatial Curvature . . . . .                              | 71        |
| 3.2.2 Extra Relativistic Particle Species . . . . .            | 73        |
| 3.2.3 Time-evolving Equation of State of Dark Energy . . . . . | 74        |
| 3.2.4 Modified Gravity . . . . .                               | 76        |
| 3.3 Validation and Results . . . . .                           | 79        |
| 3.4 Conclusions . . . . .                                      | 90        |
| <b>4 Dark Matter in the Universe</b>                           | <b>92</b> |
| 4.1 Introduction: Beyond the CDM Paradigm . . . . .            | 92        |
| 4.2 Analytic and Numerical Models for Galaxy Warps . . . . .   | 96        |
| 4.2.1 SIDM as a Drag Force . . . . .                           | 96        |
| 4.2.2 The Cluster and Subhalo System . . . . .                 | 100       |

|       |   |     |
|-------|---|-----|
| 4.2.3 | Numerical Simulation . . . . .                            | 104 |
| 4.2.4 | An Analytical Prediction of the Results . . . . .         | 106 |
| 4.3   | Results . . . . .   | 111 |
| 4.3.1 | Measuring the Warping of Disks . . . . .                  | 111 |
| 4.3.2 | Measuring the Enhanced Disk Thickness . . . . .           | 120 |
| 4.3.3 | Variations of the Cluster and Galaxy Properties . . . . . | 126 |
| 4.3.4 | Tests of Numerical Approximations . . . . .               | 128 |
| 4.4   | Discussion . . . . .                                      | 131 |

# Chapter 1

## Introduction

### 1.1 Observational Cosmology

Over the past few decades, cosmology has seen the variety and the size of available data sets increase enormously. In particular, wide-field imaging astronomical surveys, those which collect images of the sky in relatively broad bands around the optical spectrum of light, have benefited from a massive increase in data quality and quantity. As a direct example, 20 years ago, around 100 thousand galaxies over an area just under  $1\text{deg}^2$  were utilized for a first measurement of weak lensing correlations with high statistical significance [109], while present-day Dark Energy Survey Year-1 and Year-3 data sets contain around 30 and over 100 *million* galaxies over  $1,500\text{deg}^2$  and  $4,500\text{deg}^2$ , respectively. This means that 2 decades after a first detection of *cosmic shear*, the main subject of this work, survey data sizes have



increased by 3 orders of magnitude. Furthermore, the operations of the Vera Rubin Observatory<sup>1</sup>, scheduled to start full science operations in less than 3 years, will collect over 20 Terabytes of data per night and create, over a decade, catalogs of around 20 *billion* galaxies over an area of 18,000deg<sup>2</sup>.

The many consequences of such an increase in the amounts of data and the associated, massive increase in signal-to-noise will be discussed at length in the following sections, but at this point these rough numbers hopefully suffice to show that cosmology lives a historic era of wealth of data. Physicists and astronomers of a century ago were presented with General Relativity by Einstein and thus obtained, for the first time in human history, a mathematical tool to explore the Cosmos. The physicists and astronomers of this generation are presented with the challenge of turning cosmology into *precision science*.

In order to tackle this challenge, we must construct well-defined cosmological observables. A basic notion in modern cosmology, supported by early observations of E. Hubble [49], is that the distance between galaxies in the present-day universe is growing in such a way that, the further a galaxy is from us, the observers, the larger its receding velocity. A simple backwards extrapolation of this fact leads to the conclusion that objects in the universe were closer together in the past. A mathematical understanding of a universe that seems to expand as time passes is obtained with Einstein's field equations. With a *metric* that dictates the local ge-

---

<sup>1</sup><https://www.lsst.org/>

ometry of space-time and fulfills some desired symmetries (e.g. spatial homogeneity and isotropy) and an assumption of a universe that is filled with  $i$  components whose densities are given by  $\rho_i$ , we obtain the Friedman equation

$$H^2(t) \equiv \left( \frac{\dot{a}(t)}{a(t)} \right)^2 = \frac{8\pi G}{3} \sum_i \rho_i \quad (1.1.1)$$

where  $a(t)$  is the scale factor that measures the size of the universe as a function of time and  $G$  is Newton's constant. If we define a critical density  $\rho_{\text{crit}}(t) = 3H^2(t)/8\pi G$  and normalize individual components by that value at the present-day time  $t = t_0$  such that  $\Omega_i(t) \equiv \rho_i(t)/\rho_{\text{crit}}(t = t_0)$ , we can rewrite eq. (1.1.1) as

$$H^2(t) = H_0^2 \sum_i \Omega_i(t) \quad (1.1.2)$$

where we have also defined  $H_0^2 = 8\pi G\rho_{\text{crit}}(t_0)/3$ . Conservation of energy in Einstein's equations also tells us that the density of a certain component  $\rho_i$  is related to the scale factor  $a$ :

$$\frac{\dot{\rho}}{\rho} = -3(1 + \omega) \frac{\dot{a}}{a} \quad (1.1.3)$$

where we have introduced the important *equation of state* parameter  $\omega$  which relates the pressure  $p$  of a particular type of component in the universe to its energy density:

$$p = \omega\rho. \quad (1.1.4)$$

Radiation, matter (dust) and the vacuum have different equation of state parameters which relate to their degrees of freedom. In particular, we have  $\omega = \frac{1}{3}$  and 0 for radiation and matter, and  $\omega = -1$  for the vacuum (a fact we will return to

later). Using these values to solve eq. (1.1.3) for the densities and plugging their results back into eq. (1.1.2) with the  $\rho_{\text{crit}}$  normalization, we can write the evolution of the scale factor as encapsulated by  $H(a)$  as

$$H(a) = H_0 \sqrt{\Omega_m a^{-3} + \Omega_r a^{-4} + \Omega_\Lambda} \quad (1.1.5)$$

where  $\Omega_i$  are present-day normalized densities and the subscripts  $i=m, r$  and  $\Lambda$  conveniently refer to matter, radiation and the vacuum. Equation (1.1.5) also describes how each energy density decays forward in time (as a function of increasing  $a$ ), implying that the structure of matter and radiation in the universe becomes sparser and colder, and eventually becomes dominated by a constant term  $\Omega_\Lambda$ . As that happens, the solution of equation 1.1.5 in terms of the scale factor  $a$  dictates that the expansion of the universe is *accelerated* and, further into the future, exponential.

In an expanding universe with galaxies receding faster at larger distances from the observer, radiation wavelengths are *redshifted*. We can then define the redshift  $z$  of an object, which in practice is the real observable, as

$$1 + z = \frac{1}{a}. \quad (1.1.6)$$

A final remark is that, also from the Friedman equations, we obtain a *distance-redshift* relation given by

$$\chi(z) = \frac{1}{H_0} \int_0^z \frac{dz'}{\sqrt{\Omega_m (1+z')^3 + \Omega_r (1+z')^4 + \Omega_\Lambda}} \quad (1.1.7)$$

where  $\chi$  is a so-called *comoving* distance which factors out the scale factor  $a(t)$ .

The discussion above regards a smooth, unperturbed universe, where matter and radiation simply follow the background expansion starting from a dense state. The universe we observe is far too different from this picture. In reality, we see matter density perturbation grow and become galaxies and galaxy clusters, and feedback processes from baryonic physics can significantly heat up these high density environments even though the background is only getting colder. To describe the observable universe, we therefore need to study perturbations around the background.

We start by defining the density contrast of the total matter in the universe as a function of 3-D position  $\mathbf{r}$  and time (redshift)  $z$  as

$$\delta(\mathbf{r}, z) = \frac{\rho(\mathbf{r}, z) - \bar{\rho}}{\bar{\rho}} \quad (1.1.8)$$

where  $\bar{\rho}$  is the matter density averaged over some large enough volume. With this definition, we can suitably generalize the Poisson equation in terms of the density contrast and in an expanding background as

$$\nabla^2 \phi(\mathbf{r}, z) = \frac{4\pi G}{c^2} \bar{\rho}(z) a^2(z) \delta(\mathbf{r}, z) \quad (1.1.9)$$

An important aspect of this work (and of observational cosmology in general) is that we are *not* concerned with predicting  $\delta(\mathbf{r})$  at some specific position  $\mathbf{r}$ . Instead, we will seek to treat the density field as a realization of some stochastic initial conditions and make predictions for the statistical moments of this field and their evolution in time.

From the definition (1.1.8), we see that the first moment (the mean) of the density contrast is null:

$$\langle \delta(\mathbf{r}) \rangle = 0. \quad (1.1.10)$$

The lowest order we care about is, thus, the second moment of the density field (also known as a 2-point correlation). It is convenient, however, to express that in terms of the Fourier transform of the field, in which case the 2pt correlation is called the 3-D *matter power spectrum*  $P(k, z)$ :

$$\langle \delta(\mathbf{k}, z) \delta^*(\mathbf{k}', z) \rangle = (2\pi)^3 \delta_D(\mathbf{k} - \mathbf{k}') P(k, z) \quad (1.1.11)$$

where  $\delta_D$  is the 3-D Dirac delta function that ensures that power spectrum depends only on the magnitude of wavenumbers  $k$  (another manifestation of the isotropy assumption). It will become clear that  $P(k, z)$  is one of our main quantities of interest.

In order to relate the power spectrum defined above to a set of cosmological parameters such as  $\Omega_m$  and  $\Omega_\Lambda$  and assumptions on the actual cosmological model, we need to describe how the perturbations  $\delta(k, z)$  evolve in time. While more details can be found in e.g. [24], the basic argument is that a continuity equation for matter, interpreted as a fluid, can be written in the expanding background dictated by the Friedman equations and then decomposed into a stochastic initial condition  $\Phi(\mathbf{k})$ , a transfer function  $T(k)$  that determines which wavenumbers get to evolve given the causal horizon of the universe and a function  $G(z)$  that determines

their amplitude growth with time such that

$$\delta(\mathbf{k}, z) \propto \Phi(\mathbf{k})T(k)G(z). \quad (1.1.12)$$

The power spectrum of the quantity above can then be (schematically) written as

$$P(k, z) \propto A_s k^{n_s-1} T^2(k) G^2(z), \quad (1.1.13)$$

where  $A_s$  and  $n_s$  are the primordial amplitude of matter fluctuations and the so-called spectral index of the primordial matter power spectrum, respectively. Along with  $\Omega_m$  and  $\Omega_\Lambda$ , these two new numbers also define a cosmological model.

Different astrophysical probes such as the clustering of galaxies or the weak gravitational lensing patterns on the sky can offer information about the power spectrum in different length-scale regimes and cosmic times. Instead of trying to constrain the entire shape of the  $P(k, z)$  function, however, it is practical to define a new parameter which, much like  $A_s$ , characterizes the amplitude of the power spectrum. This parameter is defined as the 3-D power spectrum amplitude filtered within a window function of some radius. The form of the filter and the relevant radius are arbitrary, but conventionally it has been widely adopted to be a (real-space) top-hat function with a radius of  $8 \text{ Mpc } h^{-1}$ . We thus define the so-called  $\sigma_8$ :

$$\sigma_8^2 \equiv \int \frac{d^3k}{(2\pi)^3} |W_8(k)|^2 P_{\text{lin}}(k), \quad (1.1.14)$$

where  $W_8(k)$  is the Fourier transform of the top-hat filter and we use the linear

power spectrum. Notice that, under this definition,  $\sigma_8$  is simply the variance of the density field  $\delta(\mathbf{r})$  within the sphere of radius  $8 \text{ Mpc } h^{-1}$ .

We thus arrive at a particularly important issue in modern cosmology. Cosmological parameters can be measured at different cosmic times depending on the astrophysical probe under consideration. In particular, we can make a distinction between the amplitude parameter  $A_s$ , related to the primordial amplitude of fluctuations at early cosmic times (high redshift), and the parameter  $\sigma_8$ , measured most notably by late-time (low redshift) probes. While a concordance cosmological model would imply that both measurements agree, that may not be the case with recent experimental data.

The Cosmic Microwave Background (CMB) inference of  $\sigma_8$  comes from its own measurement of  $A_s$ ,  $n_s$  and other parameters via the statistics of fluctuations on temperature and polarization, which is then propagated into the power spectrum  $P(k)$  and its amplitude. That measurement is, therefore, coming almost exclusively from the high-redshift universe<sup>2</sup>. This propagation, however, assumes a cosmological model.

A large number of observational probes have established that the “vanilla” cosmological model is one whose gravitational evolution is dictated by General Relativity (GR) and the components of the universe are dominated by a *cosmological*

---

<sup>2</sup>A caveat about this statement is that the CMB temperature field also experiences lensing by the large scale structure of the universe, which in turn couples the low-redshift universe to the high-redshift observables.

*constant* which maps into the term  $\Omega_\Lambda$  in eq. (1.1.5) as well as some form of collisionless (or *cold*) matter that does not emit radiation, the so-called Cold Dark Matter (CDM). This model is called  $\Lambda$ CDM and is at the heart of modern cosmology.

So, in other words, while the CMB measures to great accuracy the cosmological parameters at early cosmic times and infers  $\sigma_8$  at late times given the fiducial cosmological model assumption, weak gravitational lensing can measure  $\sigma_8$  *directly at late times*. Comparing the late and early time measurements provides an end-to-end test of the cosmological paradigm. This is where gravitational lensing (and other low-redshift probes) become a crucial cosmological observable. If discrepancies exist between these inferences, then a possible consequence is that new physics is required in our models.

Interestingly, discrepancies do seem to exist in the measurement of  $\sigma_8$  as inferred from the CMB and the lensing of galaxies [42, 43, 101]. This so-called “ $\sigma_8$  tension” has been claimed to be between the  $2\sigma$  (95% confidence level) and  $3\sigma$  (99.7% c.l.), and while these results are recent and still under debate, most of the current discussions are, understandably, around the potential systematic uncertainties that can bias either the CMB measurements, or lensing, or both.

As far as this work is concerned, this is a brief description of the state of modern cosmology. We now describe the fundamentals of Weak Lensing (WL) and, still in this introductory piece, the Dark Energy Survey data utilized to obtain WL cosmology constraints.



## 1.2 Weak Lensing

One of the most striking consequences of General Relativity is that light trajectories are bent in a gravitational field in such a fashion somewhat similar to classic optics. From this analogy we draw the name “gravitational lensing”. We will specify later the “strong” and “weak” lensing regimes, but for now let us show that GR predicts a deflection angle when photons travel across a gravitational field.

In order to do that, let us define the geodesic equation that dictates the motion of an object in a covariant form (i.e. a form that is invariant under coordinate transformations):

$$\frac{d^2 x^\alpha}{d\lambda^2} = -\Gamma_{\mu\nu}^\alpha \frac{dx^\mu}{d\lambda} \frac{dx^\nu}{d\lambda} \quad (1.2.1)$$

where  $\lambda$  is an arbitrary parameter with respect to which the trajectory  $x^\alpha = x^\alpha(\lambda)$  is varied (e.g. time, if we’re dealing with a massive object). The symbol  $\Gamma_{\mu\nu}^\alpha$  is called a “connection”, and Einstein summation is implied. When the right-hand side of eq. (1.2.1) is null, we of course recover a purely inertial motion, so the term that goes with  $\Gamma_{\mu\nu}^\alpha$  can be thought of as a “force” acting on the object, deflecting it away from its unperturbed path.

Let us consider the path of light itself, in the absence of a gravitational field. Without going into much detail, which can be found in [18, 24, 25], consider the metric tensor for such a spacetime as  $\eta_{\mu\nu}$ . Consider also that the line element in spacetime is given by

$$ds^2 = \eta_{\mu\nu} \frac{dx^\mu}{d\lambda} \frac{dx^\nu}{d\lambda}. \quad (1.2.2)$$

Light is special and we cannot parametrize its trajectory in terms of “proper” time (the time experienced by the observer in motion), but we can use again some arbitrary parameter  $\lambda$ . Additionally, from Special Relativity, we have  $ds^2 = 0$  for light rays. The equations of motion for light in a flat spacetime  $\eta_{\mu\nu}$  are, thus:

$$\eta_{\mu\nu} \frac{dx^\mu}{d\lambda} \frac{dx^\nu}{d\lambda} = 0; \quad \frac{d^2 x^\alpha}{d\lambda^2} = 0. \quad (1.2.3)$$

By using the definition of the connection:

$$\Gamma_{\mu\nu}^\alpha = \frac{\partial x^\alpha}{\partial \lambda^\beta} \frac{\partial^2 \lambda^\beta}{\partial x^\mu \partial x^\nu}$$

and some chain rules, one can finally show, using only the Equivalence Principle<sup>3</sup> (E.P.) that light trajectories are bent away from their “inertial” path by transforming eqs. (1.2.3) into an arbitrary gravitational field determined by the metric  $g_{\mu\nu}$  to obtain:

$$g_{\mu\nu} \frac{dx^\mu}{d\lambda} \frac{dx^\nu}{d\lambda} = 0; \quad \frac{d^2 x^\alpha}{d\lambda^2} + \Gamma_{\mu\nu}^\alpha \frac{dx^\mu}{d\lambda} \frac{dx^\nu}{d\lambda} = 0, \quad (1.2.4)$$

where we see that a term proportional to  $\Gamma_{\mu\nu}^\alpha$ , a “deflecting force” is now acting on the path of light.

While the E.P. suffices to show that light is bent by a gravitational field, we can go further and calculate *how much* it is deflected by, in terms of an angle. We start this derivation again with eq. (1.2.1), but now relate the 4-D vector  $x^\alpha$  and its derivative to the relativistic 4-momentum:

$$\frac{dx^\alpha}{d\lambda} \equiv p^\alpha = (E/c, p^i), \quad (1.2.5)$$

---

<sup>3</sup>The E.P. is the requirement that equations of motion must be invariant under a transformation into an arbitrary gravitational field, i.e. all observers must experience the same physical laws.

where  $E$  is the energy,  $c$  is the speed of light and  $p$  is the momentum<sup>4</sup>. Under this assumption, we have

$$\frac{dx^i}{d\lambda} = \frac{dx^i}{dt} \frac{dt}{d\lambda} = \frac{E}{c} \frac{dx^i}{d\lambda} \quad (1.2.6)$$

and, to first order and considering that the change in energy is small, the geodesic equation can be written as

$$\frac{E^2}{c^2} \frac{d^2 x^i}{dt^2} = -\Gamma_{\mu\nu}^i p^\mu p^\nu. \quad (1.2.7)$$

In the Newtonian limit, we can write the metric  $g_{\mu\nu}$  by relating it to the classical gravitational of a point mass:

$$g_{00} = c^2 \left( 1 - \frac{2GM}{rc^2} \right) \quad (1.2.8)$$

$$g_{ij} = -\delta_{ij} \left( 1 + \frac{2GM}{rc^2} \right) \quad (1.2.9)$$

where  $G$  is Newton's gravitational constant,  $M$  is the deflecting mass,  $r$  is the radius from that mass and  $\delta_{ij}$  is the Kronecker delta. Using eqs. (1.2.8) and (1.2.9) and the definition of the connection in terms of the metric (commonly known as Christoffel symbol), we can write eq. (1.2.7) as

$$\frac{d^2 x^i}{dt^2} = -\frac{2GMx^i}{r^3}. \quad (1.2.10)$$

Equation (1.2.10) can be solved with the geometry of the problem specified in figure 1.1 to yield a deflection angle of

$$\delta\theta = \frac{4GM}{c^2 b}, \quad (1.2.11)$$

---

<sup>4</sup>We shall use the conventional notation that greek indices run over 4 dimensions, and latin indices run over 3 spatial dimensions.

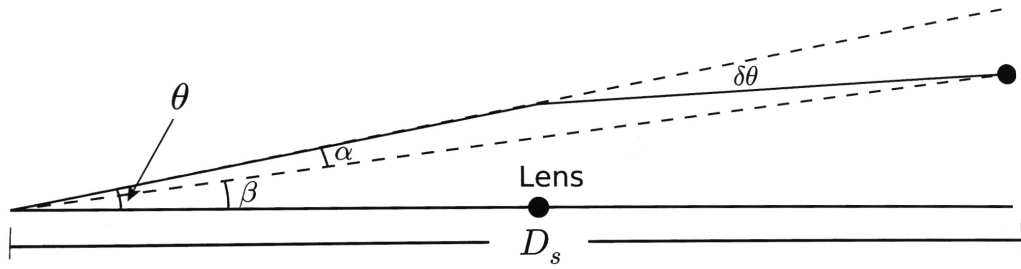


Figure 1.1: The geometry of the problem of a light ray propagating from a source at a distance  $D_S$  from the right, and being deflected by a point mass  $M$  at  $D_L$  by an angle  $\delta\theta$ . Figure extracted from [25].

where  $b$  is the impact parameter of the light ray.

It is fair to pause for a moment and appreciate the fact that equation (1.2.11) triggered not only the birth of an entire field of astronomy and the creativity of uncountable scientists over a century, but also massive investments in engineering and technology over the recent decades to design and create experiments that employ this knowledge to understand the cosmos. These few pages will not do it justice, so we kindly ask the reader to lower their standards when approaching the rest of this text.

In an astronomical setting, the impact parameter  $b$  happens at an angle that is typically small enough, and the deflector (which from now on we are entitled to call a *lens*) is usually at such large radial distances  $D_L$  from the observer that we can

write  $b = \theta D_L$  and obtain the Einstein radius for some massive lens  $M$ :

$$\theta_E \equiv \sqrt{\frac{4GM}{D_L c^2}}. \quad (1.2.12)$$

We can discern between 2 different lensing regimes using  $\theta_E$ . When the angular separation  $\theta'$  between a *source* and its deflecting lens is smaller than  $\theta_E$  (or larger but still close enough to it), we can observe multiple source images (or source images that form arcs). This regime is called *strong lensing*, and while it is somewhat easily identifiable, it is also statistically rare as the angular separations involved are generally small and require unlikely near-alignments of massive objects along the line of sight. The distortions caused on images when  $\theta' \gg \theta_E$ , however, are extremely small and typically dominated by many forms of astrophysical and observational noise, but are at the same time present in a very large number of source images. This second regime is called *weak lensing* and is the main subject of the rest of this work.

The point-mass deflection characterized by eq. (1.2.11) is too simplistic if we aim to describe weak lensing in the universe, so let us first generalize that concept. We certainly want to define lensing deflections caused by an arbitrary gravitational potential along the line of sight of the observer. It is easy to implement this generalization by going back to the metric components (1.2.8) and (1.2.9) and change the point-mass potential  $GM/r$  by the 3-D gravitational potential  $-\phi$ . Consider also that, instead of taking derivatives with respect to time  $t$ , we differentiate with respect to the radial distance to towards the source, which is, with the distance-

redshift relation, a good approximation for cosmic time even though we are neglecting time dilations caused by lensing. In cartesian coordinates where  $z$  is the radial distance and the  $i = 1, 2$  components of  $x^i$  are coordinates on the plane of the sky, change derivatives to  $z/c$  and we can finally write the geodesic equation (1.2.10) as

$$\frac{d^2 x^i(z)}{dz^2} = -\frac{2}{c^2} \frac{\partial \phi(x^i, z)}{\partial x^i}. \quad (1.2.13)$$

Integrating eq. (1.2.13) and changing the notation from  $x^i$  (with  $i = 1, 2$ ) to more intuitive 2-D vectors on the plane of the sky that match the geometry on Figure 1.1, we obtain the *lens equation*

$$\vec{\beta} = \vec{\theta} - \vec{\alpha}(\vec{\theta}), \quad (1.2.14)$$

where we define the deflection angle  $\vec{\alpha}$  as

$$\alpha^i(\vec{\theta}) = \frac{1}{c^2} \frac{\partial \Phi(\vec{\theta})}{\partial \theta^i} \quad (1.2.15)$$

in terms of the gravitational potential projected along the line of sight towards the source physically located at  $\vec{\beta}$ :

$$\Phi(\vec{\theta}) = \frac{2}{D_S} \int_0^{D_S} dD_L \frac{D_{SL}}{D_L} \phi(x^i = D_L \theta^i, D_L), \quad (1.2.16)$$

where  $D_{SL} = D_S - D_L$  is the distance between the lens and the source. We can make a couple of important remarks about the last few equations. One is that there is no deflection  $\vec{\alpha}$  if the projected potential is not varying over the plane of the sky. This means that a uniform massive sheet would not cause a lensing deflection. Another remark is that the factor  $D_{SL}/D_L$  tells us that if the lensing structure at a distance

$D_L$  is too close to the source at  $D_S$ , the lensing signal vanishes. Similarly, if the source is too close to the observer and  $D_S \rightarrow 0$ , the projected potential is also negligible and there is also no lensing signal. We can also show by going back to figure 1.1 that

$$\vec{\theta}D_S = \vec{\beta}D_S + \delta\vec{\theta}D_{SL},$$

and using the lens equation we just derived to get

$$\vec{\theta}D_S = \vec{\beta}D_S + \vec{\alpha}D_S$$

we end up with the useful identity

$$\vec{\alpha} = \frac{D_{SL}}{D_S}\delta\vec{\theta}. \tag{1.2.17}$$

So far we have succeeded in showing how gravitational lensing displaces the observed image of a small source given an arbitrary 3-D gravitational potential  $\phi(x^i, z)$  and its 2-D counterpart projected on the plane of the sky  $\Phi(\vec{\theta})$ , often called the “lensing potential”. We now increase the level of complexity by another step, and consider an *extended* source image. We are approaching the observational case of realistic astronomical sources such as extended galaxies on the sky. As we start delving into real astronomy, we must learn the astronomical jargon and the completely arbitrary definitions and nomenclature that come with it.

We first define the *luminosity* of an object as the total energy emitted by that object per unit time (it can also be given in terms of the astronomical magnitude system by the “absolute bolometric magnitude”). The luminosity is generally not

an observable quantity, so we also need to define the *apparent brightness* (or simply *brightness*) of an object as the amount of energy per unit time that reaches some detecting area (such as the observer's retina, a telescope CCD, etc). Brightness, thus, certainly depends on the distance between the object and the observer, and in general also depends on whether or not any absorption of light occurs between the emitter and the observer.

Since the *flux* (energy per time per area) of an extended object decreases with the square of its distance from the observer, but at the same time the physical area encompassed by some fixed angle increases with the square of the distance, we can also define a quantity that is invariant of distance: the *surface brightness* of an object. The energy per time received from a given source is then equal to the surface brightness of that source multiplied by its angular size.

What matters most for us is that lensing *preserves the surface brightness*, i.e. it does not magically increase the energy of emitted photons, but it does *change the observed flux* of an object because it allows the observer to collect photons from a larger sky area. This is easier to see by referring back to figure 1.1: in the presence of a lens, the observer of the lensed image sees the angular area  $d^2\theta$  encompassed by a radius  $\vec{\theta}$ . If no deflection occurred, the observer would see a smaller angular area  $d^2\beta$  of radius  $\vec{\beta}$ . The statement that the surface brightness  $\mathcal{S}$  is unchanged is  $\mathcal{S}^{\text{un-lensed}}(\vec{\beta}) = \mathcal{S}^{\text{lensed}}(\vec{\theta})$  and the ratio of lensed to un-lensed flux is called the



magnification  $\mu$  defined as

$$\mu = \frac{\mathcal{S}^{\text{lensed}} d^2\theta}{\mathcal{S}^{\text{un-lensed}} d^2\beta} = \frac{d^2\theta}{d^2\beta}. \quad (1.2.18)$$

Using the lens equation (1.2.14), this Jacobian can be written as a  $2 \times 2$  matrix:

$$\frac{\partial\beta_i}{\partial\theta_j} = \begin{pmatrix} 1 - \frac{\partial\alpha_x}{\partial\theta_x} & -\frac{\partial\alpha_x}{\partial\theta_y} \\ -\frac{\partial\alpha_y}{\partial\theta_x} & 1 - \frac{\partial\alpha_y}{\partial\theta_y} \end{pmatrix} = I - \Psi_{ij}, \quad (1.2.19)$$

where  $I$  is the identity matrix and  $\Psi_{ij}$  is the ‘‘distortion tensor’’ defined right below. Since we already know how to relate the deflection angle  $\alpha$  to the lensing potential  $\Phi$  through equation (1.2.15), we can tell that the off-diagonal terms have to be the same<sup>5</sup>. So the distortion tensor  $\Psi_{ij}$ , which ultimately dictates how the lensed area gets transformed, needs 3 degrees of freedom. To take advantage of the trace of that tensor as one of the degrees of freedom, we can write it using equation (1.2.15):

$$\Psi_{ij} = \begin{pmatrix} \kappa + \gamma_1 & \gamma_2 \\ \gamma_2 & \kappa - \gamma_1 \end{pmatrix} \quad (1.2.20)$$

with  $\kappa$ ,  $\gamma_1$  and  $\gamma_2$  defined as

$$\kappa \equiv \frac{1}{2c^2} \left( \frac{\partial^2\Phi}{\partial\theta_x^2} + \frac{\partial^2\Phi}{\partial\theta_y^2} \right) = \frac{1}{2c^2} \nabla^2\Phi, \quad (1.2.21)$$

$$\gamma_1 \equiv \frac{1}{2c^2} \left( \frac{\partial^2\Phi}{\partial\theta_x^2} - \frac{\partial^2\Phi}{\partial\theta_y^2} \right), \quad (1.2.22)$$

$$\gamma_2 = \frac{1}{c^2} \frac{\partial^2\Phi}{\partial\theta_x\partial\theta_y}. \quad (1.2.23)$$

---

<sup>5</sup>Since the potential has the symmetry  $\partial_x\partial_y\Phi = \partial_y\partial_x\Phi$

To understand how the distortion tensor transforms the shapes of extended objects, consider setting  $\gamma_1 = \gamma_2 = 0$  and solving the equation that defines the Jacobian (1.2.19). In that case, we get

$$\frac{d\beta_1}{d\theta_1} = 1 - \kappa; \quad \frac{d\beta_2}{d\theta_2} = 1 - \kappa,$$

which can be solved and Taylor expanded for  $\kappa \ll 1$  to yield  $\vec{\theta} = (1 + \kappa)\vec{\beta}$ . Assuming the true source is a circle of radius  $\beta$ , this means the observed image at  $\vec{\theta}$  is also a circle enlarged by a factor  $(1 + \kappa)$ . Applying the same reasoning while setting  $\kappa = \gamma_2 = 0$ , we get

$$\frac{d\beta_1}{d\theta_1} = 1 - \gamma_1; \quad \frac{d\beta_2}{d\theta_2} = 1 + \gamma_1,$$

which can be solved to yield  $(1 - \gamma_1)^2\theta_1^2 + (1 + \gamma_1)^2\theta_2^2 = \beta^2$ , which describes an ellipse. A similar thing happens for nonzero  $\gamma_2$ .

We thus reach an important conclusion: the independent modes by which lensing distorts an extended object is by uniformly dilating or shrinking it ( $\kappa > 0$  and  $\kappa < 0$  respectively), or also by imparting a *shear* on images (through  $\gamma_{1,2}$ ) which effectively makes them more elliptical. These effects are summarized in figure 1.2.

We are close to connecting the shapes of observed objects to the gravitationally induced shear they pick up from the intervening matter. Observed shapes are normally characterized in terms of *ellipticities*. We can show below how shears ( $\gamma_1, \gamma_2$ ) relate to a certain definition of ellipticities ( $e_1, e_2$ ). For a more complete treatment of this relation, and in particular how to make sure ellipticities are actually unbiased estimators of the shears, see [8].







|            | < 0   | > 0  |
|------------|---|--|
| $\kappa$   |  |  |
| $\gamma_1$ |  |  |
| $\gamma_2$ |  |  |

Figure 1.2: The 3 different degrees of freedom captured by the distortion tensor  $\Psi_{ij}$ . While  $\kappa$  shrinks/enlarges a circular image,  $\gamma_{1,2}$  shear the image making it more elliptical. (Copyright: TallJimbo - Own work, CC BY-SA 3.0, <https://commons.wikimedia.org/w/index.php?curid=4179196>.

Modified for this work.)

Let us quantify the ellipticity in terms of the moments of the surface brightness as

$$q_{ij} = \int d^2\theta \mathcal{S}^{\text{observed}}(\vec{\theta})\theta_i\theta_j, \quad (1.2.24)$$

and, based on these moments, let us define the ellipticity components in an analogy to how one would quantify the axis ratios of an ellipse, which is bound between the values (0,1) as

$$e_1 \equiv \frac{q_{11} - q_{22}}{q_{11} + q_{22}}; \quad e_2 \equiv \frac{2q_{12}}{q_{11} + q_{22}}. \quad (1.2.25)$$

Using the Jacobian (1.2.19) and converting from the image plane at  $\theta_i$  to the source

plane at  $\beta_i$ , we can write the ellipticities to first order in the shear as<sup>6</sup>

$$e_i \approx \frac{2\gamma_i}{1 - \kappa}. \quad (1.2.26)$$

For the most part in the weak lensing regime, we will be dealing with galaxies that live in lines of sight that are not too dramatically impacted by foreground structure. This means that, for a large fraction of galaxies in a weak lensing sample, we can assume  $\kappa \ll 1$  and disregard the denominator of (1.2.26). This approximation is a fairly good one and is often called the “reduced shear” approximation. Under this approximation, lensing effects are reduced to 2 degrees of freedom, namely the shears.

A more recent treatment of the connection between the observed shapes and the theoretic shears follows [91]. Instead of the approximations that led to eq. (1.2.26), consider a measurement of 2-D galaxy shapes  $e_i$  as a Taylor expansion around zero gravitational lensing:

$$e_i = e_i|_{\gamma=0} + \left. \frac{\partial e_i}{\partial \gamma_j} \right|_{\gamma=0} \gamma_j + \dots \quad (1.2.27)$$

where  $\gamma = 0$  represents the absence of lensing. For 2-D shapes and shears,  $R_{ij} \equiv \partial e_i / \partial \gamma_j$  is a  $2 \times 2$  matrix called *shear response*, and encapsulates, to first order, how the ellipticity estimator  $e_i$  changes under a small shear  $\gamma_j$ :

$$R_{ij} = \begin{pmatrix} \partial e_1 / \partial \gamma_1 & \partial e_2 / \partial \gamma_1 \\ \partial e_1 / \partial \gamma_2 & \partial e_2 / \partial \gamma_2. \end{pmatrix} \quad (1.2.28)$$

---

<sup>6</sup>The factor of 2 is a convention here that can be eliminated with a different definition of eqs. (1.2.25).

With this in mind, the ellipticity becomes estimator of shear if we assume that, over large enough ensembles and in the absence of systematic uncertainties the orientation of unlensed galaxies is random such that  $\langle e_i \rangle_{\gamma=0} = 0$ :

$$\langle e_i \rangle \approx \langle R_{ij} \gamma_j \rangle. \quad (1.2.29)$$

The average here is actually taken on each entry of the matrix  $R_{ij}$ . We can approximately invert this relation by measuring  $e_i$  the response matrix  $R_{ij}$  for each galaxy in the sample:

$$\langle \gamma_i \rangle \approx \langle R_{ij} \rangle^{-1} \langle R_{ij} \gamma_j \rangle. \quad (1.2.30)$$

While some of these matrix operations are poorly defined, we have found in [113] that the mean response matrix is roughly diagonal, and eq. (1.2.30) can in fact be applied to each component  $i = (1, 2)$  separately.

Some of the derivations above start to show how tough weak lensing can be in terms of statistics and required data. Current galaxy surveys such as the DES have reached of order 100 million observed galaxies, so these operations above need to be applied to each of them, turning this problem into a computational challenge. As we will see later, the actual magnitude of  $\gamma_i$  in the weak lensing regime is or order 0.01 or less, while intrinsic noise is usually around  $40\times$  larger at 0.40 (recall that our ellipticity and shear definitions are bound between the values of [0,1]).

We can now relate the measured galaxy shapes  $e_{1,2}$  to an estimator of the gravitational shears  $\gamma_{1,2}$ , which brings us closer to the goal of connecting lensing observables to theory. In order to do that, let us recast some of our definitions in 2-D

Fourier space<sup>7</sup>. Equations (1.2.21)-(1.2.23) translate nicely into harmonic space:

$$\kappa(\vec{\ell}) = -\frac{\ell^2}{2c^2}\Phi(\vec{\ell}) \quad (1.2.31)$$

$$\gamma_1(\vec{\ell}) = \frac{-\ell_x^2 + \ell_y^2}{2c^2}\Phi(\vec{\ell}) \quad (1.2.32)$$

$$\gamma_2(\vec{\ell}) = \frac{-\ell_x\ell_y}{c^2}\Phi(\vec{\ell}) \quad (1.2.33)$$

We can choose to define, without loss of generality, the vector  $\vec{\ell}$  with a magnitude  $\ell$  and an angle  $\phi_\ell$  with respect to a fixed  $x$ -axis, such that the  $x$  component is  $\ell_x = \ell \cos \phi_\ell$  and rewrite the shears above as

$$\gamma_1(\vec{\ell}) = -\frac{\ell^2}{2c^2}\Phi(\vec{\ell}) \cos(2\phi_\ell); \quad \gamma_2(\vec{\ell}) = -\frac{\ell^2}{2c^2}\Phi(\vec{\ell}) \sin(2\phi_\ell). \quad (1.2.34)$$

A final definition we can make is to take linear combinations of  $\gamma_1$  and  $\gamma_2$  as our modeled signal. Let us define two orthogonal  $E$  and  $B$  modes as:

$$E(\vec{\ell}) \equiv -\gamma_1(\vec{\ell}) \cos(2\phi_\ell) - \gamma_2(\vec{\ell}) \sin(2\phi_\ell) = -\frac{\ell^2\Phi(\vec{\ell})}{2c^2}, \quad (1.2.35)$$

$$B(\vec{\ell}) \equiv \gamma_1(\vec{\ell}) \sin(2\phi_\ell) - \gamma_2(\vec{\ell}) \cos(2\phi_\ell) = 0. \quad (1.2.36)$$

Two important things must be noted about our choice of linear combinations of  $\gamma_{1,2}$  that make up the  $E/B$  modes. The first one is that  $E(\vec{\ell})$  is equal to  $\kappa(\vec{\ell})$ , so the convergence field  $\kappa$  contains the  $E$  signal of interest. The other important thing is that we realize the  $B$ -mode part of the signal vanishes. This is strictly tied to all of the assumptions we have made so far (i.e. that gravity is causing all of

---

<sup>7</sup>Our convention here will be  $f(\vec{\ell}) = \int d^2\theta e^{-i\vec{\ell}\cdot\vec{\theta}} f(\vec{\theta})$  and  $f(\vec{\theta}) = \int \frac{d^2\ell}{(2\pi)^2} e^{i\vec{\ell}\cdot\vec{\theta}} f(\vec{\ell})$

the lensing, that the shears  $\gamma$  measured on galaxies are unbiased, etc). Even when all of these assumptions are true, there is still statistical noise in both the  $E$  and  $B$  pieces of the signal, so the results in eqs. (1.2.35) and (1.2.36) are only true on average. Nevertheless, with eq. (1.2.36) we have made taken an important step towards finding a set of “null tests” for weak lensing galaxy samples.

Knowing that  $\kappa$  contains the most valuable part of the signal, let us combine eqs. (1.2.21) and (1.2.16) to get

$$\kappa(\vec{\theta}) = \frac{1}{c^2} \int_0^{D_S} dD_L \frac{D_{SL} D_L}{D_S} \nabla^2 \phi. \quad (1.2.37)$$

We see that the Laplacian of the 3-D gravitational potential appears in the integrand and we can immediately replace it by the cosmological version of the Poisson equation (1.1.9):

$$\kappa(\vec{\theta}) = \int_0^{D_S} dD_L W(D_S, D_L) \delta(D_L \vec{\theta}, D_L) \quad (1.2.38)$$

where we have defined a certain window function  $W$  given by

$$W(D_S, D_L) = \frac{D_{SL} D_L}{D_S} \frac{4\pi G}{c^2} \bar{\rho}(a) a^2(D_L). \quad (1.2.39)$$

We can polish the notation of both of these last equations by, firstly, using instead of  $D_L$  and  $D_S$  the *angular diameter distances*  $D_A(z)$  to the lenses and to the sources, respectively. This quantity relates to the comoving distance (1.1.7) via  $D_A = \chi(z)/(1+z)$  such that, eg.  $D_L = D_A(z_L) = \chi(z_L)/(1+z_L)$ . Secondly, it was through the deflection of sources at a single redshift “slice” that we arrived at the geometric factor  $D_{SL} D_L / D_S$ . In reality, the source galaxies spread over a

wide range in redshift (radial distance) and their distribution is characterized by a galaxy number density  $n(z)$ . Also, since eq. (1.2.39) depends on  $\bar{\rho}$ , we can replace it by  $\Omega_m$  using eq. (1.1.2). With these modifications, we end up with the so-called *lensing efficiency kernel*

$$W(\chi) = \frac{3H_0^2\Omega_m}{2c^2} \frac{\chi}{a(\chi)} \int_0^\infty dz \frac{dn(z)}{dz} \frac{\chi(z) - \chi}{\chi(z)} \quad (1.2.40)$$

and the notation of eq. (1.2.38) is also simplified to

$$\kappa(\vec{\theta}) = \int d\chi W(\chi) \delta(\chi\vec{\theta}, \chi). \quad (1.2.41)$$

We can finally go back to the point made earlier, which led to eq. (1.1.11), that cosmological observables tend to be statistical. Again, we are interested in predictions that relate to the matter power spectrum  $P(k, z)$  and the cosmological parameters that define it. Equation (1.2.41) gives us a direct way to do that: we just need to look at the 2nd moment of the convergence. The 2-D analogous of eq. (1.1.11) using the Fourier transform of (1.2.41) is then

$$\langle \kappa(\vec{\ell}) \kappa(\vec{\ell}') \rangle = (2\pi)^2 \delta_D(\vec{\ell} - \vec{\ell}') C_{\kappa\kappa}(\ell) \quad (1.2.42)$$

where  $C_{\kappa\kappa}(\ell)$  is the (2-D harmonic space) power spectrum of the convergence. Identifying the power spectrum wavelength  $k$  with  $\ell/\chi$  and using eqs. (1.2.41), (1.2.42) and (1.1.11), we can finally write the convergence power spectrum in terms of the matter power spectrum<sup>8</sup>:

$$C_{\kappa\kappa}(\ell) = \int d\chi \frac{W(\chi)^2}{\chi^2} P\left(\frac{\ell}{\chi}; \chi\right). \quad (1.2.43)$$

---

<sup>8</sup>The so-called Limber approximation is needed here: the integral is formally over along the



We will refer to this as the *cosmic shear power spectrum*. It carries very interesting information: the lensing signal is a projection of the power spectrum, weighted by some lensing efficiency kernel that is determined by the distribution of source galaxies  $n(z)$ . As we will show later, this lensing kernel is relatively broad given our present-day uncertainties on  $n(z)$  and the mixes information from different wavelengths  $k$  of the power spectrum. Nevertheless, for a survey like the DES, this kernel peaks at fairly low redshifts (around  $z = 0.5$ ), which means the lensing signal is mostly affected by structure around those cosmic times. If the observed source galaxies reach higher redshifts, so does the kernel and consequently the lensing signal probes earlier cosmic times.

A final addition to this theoretical modeling of cosmic shear is that we will compute 2-point correlations by splitting the redshift distribution into a few wide slices. The reasoning is that, since sources at different redshifts probe different cosmic times, cross-correlations between different *redshift bins* contain geometrical information on distances. An example of redshift binning is shown in Figure 1.3, extracted from the DES Y1 cosmic shear results. We thus generalize the shear power spectrum (1.2.43) as

$$C_{\kappa\kappa}^{ij}(\ell) = \int d\chi \frac{W^i(\chi)W^j(\chi)}{\chi^2} P\left(\frac{\ell}{\chi}; \chi\right), \quad (1.2.44)$$

---

radial direction of 2 lines of sight, but we assume that modes that are transverse to these lines of sight are more important than those in the radial direction, so our result is simplified. This is a very good approximation for the shear power spectrum, missing only a couple percent of the signal at very large angular scales that are essentially not used in our analysis.

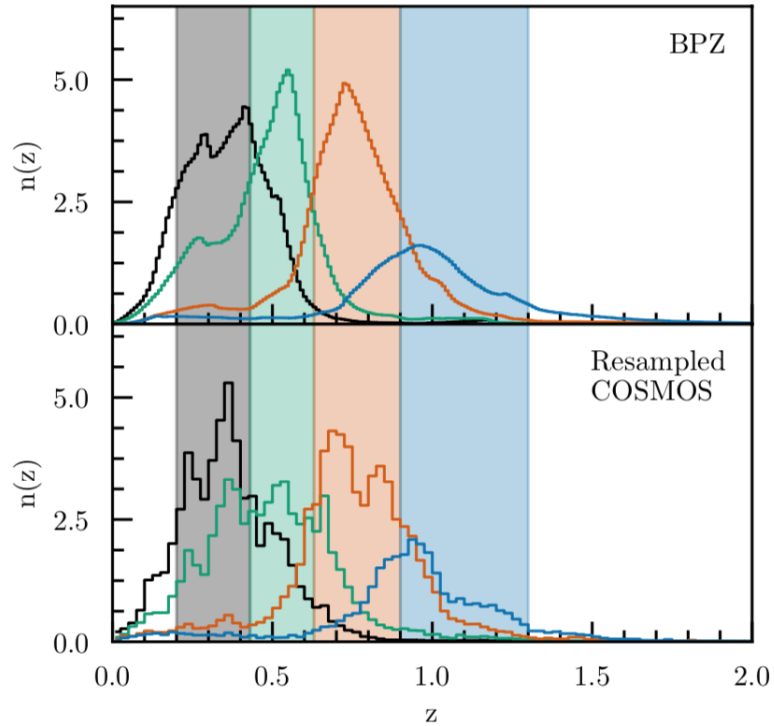


Figure 1.3: The redshift distribution of source galaxies  $n(z)$  in DES Y1, split into 4 different bins. Top and bottom panels show different calibration methods, and wide bands show the nominal edges of each redshift bin with its specific distribution of galaxies,  $n^i(z)$ . Extracted from [101].

where each kernel  $W^i(\chi)$  is computed with eq. (1.2.40) from the distribution of galaxies inside a specific redshift bin,  $n^i(z)$ .

To finalize this section, we note that, up to this point, we have been describing the pristine cosmic shear signal in the absence of any real-data complications. These complications are of statistical, systematic and computational origin. As is similar to any experimental endeavor, the vast majority of the time spent by researchers

revolves around addressing the systematic and statistical uncertainties of the data in computationally feasible ways. The remaining of this dissertation focuses on those aspects of cosmic shear.

### 1.3 The Dark Energy Survey Data

Here we describe the data collected and utilized by the Dark Energy Survey, and summarize the procedure for creating the shape catalogs from which we measure cosmic shear correlation functions<sup>9</sup>.

The Dark Energy Survey (DES) is a five and a half year observing program using the 570 megapixel DECam [32] on the Blanco telescope at the Cerro Tololo Inter-American Observatory (CTIO). The nominal DES wide-field survey images 5,000deg<sup>2</sup> of the southern sky to 24th *i*-band limiting magnitude in the *grizY* bands spanning 0.40-1.06  $\mu\text{m}$ . The survey tiling strategy ultimately consists of ten overlapping 90 second exposures in each of *griz* and 45s exposures in *Y* over the full wide-field area.

The DES Year 1 (Y1) shape catalogs used in this work are based on observations taken between Aug. 31, 2013 and Feb. 9, 2014 during the first full season of DES operations. DES Y1 wide-field observations were targeted to a large region overlapping the South Pole Telescope (SPT) survey footprint extending between approximately  $60\text{deg} < \delta < 40\text{deg}$ , and a much smaller area overlapping the “Stripe

---

<sup>9</sup>Originally presented in [101], to which LFS contributed in the writing and analysis.

82" region of the Sloan Digital Sky Survey (SDSS), which is not included in this analysis.

The observed area was limited in the DES Y1 period to reach a sufficient number of overlapping exposures across the observed footprint. In practice, this resulted in a total area of about  $1,514\text{deg}^2$  with a mean depth of three exposures, after masking potentially bad regions not used for weak lensing [27].

The DES Year 3 (Y3) data, conversely, reached the full footprint of the survey taking data between the years of 2014 and 2015, but at a somewhat shallower depth (on average 5 exposures) than the expected full data, with over 400 million objects before the masking of galaxies not utilized in the WL shape catalogs. After preliminary maskings of bad regions, the DES Y3 survey area is of around  $4,200\text{deg}^2$ . As we shall note later, the increase in statistical power from DES Y1 to Y3 in the WL signal thus comes mostly from this almost three-fold increase in survey area. The final shape catalog production and validation in DES Y3 is still ongoing and publications are in preparation. The footprint of DES Y1 (green) and Y3 (blue) are shown in Fig. 1.4.

The DES Y1 data incorporated a variety of improvements over the DES Science Verification (SV) data used in preliminary DES weak lensing analyses, including updates to the telescope and systems components and to data processing. These are discussed in detail in [27], which describes the production and validation of a ‘Gold’ catalog of 137 million objects prior to the ‘bad region’ masking referred

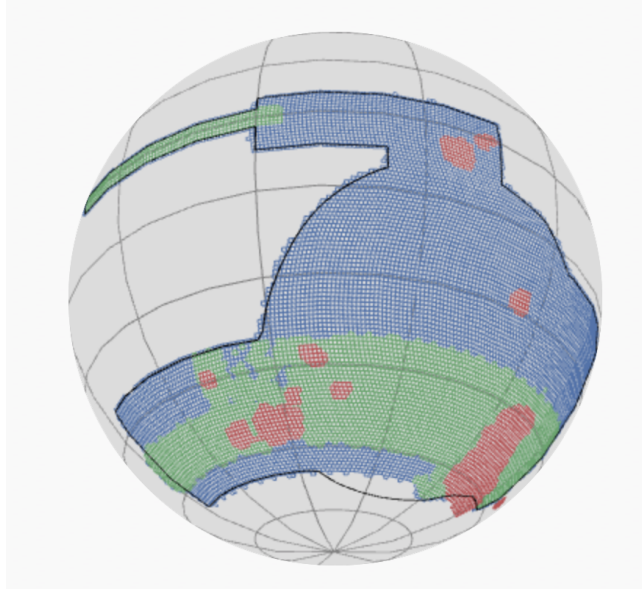


Figure 1.4: The footprint of DES Y1 (in green) and DES Y3, which cover roughly  $1,400 \text{ deg}^2$  and  $4,200 \text{ deg}^2$  square degrees of the southern sky.

to above, and in [113], where the Metacalibration shape catalog production and validation is described.

Metacalibration is a method to calibrate a shear statistic, such as a mean shear estimate or shear two-point function, from available imaging data, without requiring significant prior information about galaxy properties or calibration from image simulations [50,91]. Metacalibration has been tested with complex image simulations and shown to be accurate at the part per thousand level [91]. The implementation used in DES Y1 is described in detail in [113], where the ellipticity is measured using a single Gaussian model that is fit to the galaxy image in the *riz* bands. The galaxy image is then artificially sheared and the ellipticity remeasured to con-

construct the shear response matrix via numerical derivatives of the ellipticity. We do this by deconvolving the Point-Spread Function (PSF), applying a shear, and then reconvolving by a symmetrized version of the PSF.

This results in one unsheared and four sheared versions of the shape catalog (one for each direction ( $\pm$ ) and component of shear), all of which include flux measurements for photo-z estimation. Some limitations in the application of Metacalibration to DES Y1 data are discussed in [113], which leads us to assign a non-zero mean for the Gaussian prior assumed in this analysis on the shear calibration of  $m = 0.012 \pm 0.013$ . This error budget is dominated by our estimate of the unaccounted effects of contaminating light from neighboring objects on the shear estimation.

With Metacalibration, corrections are calculated for both the response of the shape estimator to a shear and the response of object selections to a shear. The Metacalibration procedure produces a noisy estimate of the shear response  $R_\gamma$  for each galaxy, which is then averaged to produce  $\langle R_\gamma \rangle$ . The induced selection bias is calculated only in the mean  $\langle R_S \rangle$ . These quantities are in general 2x2 matrices of the ellipticity components. The explicit calculation of these corrections using the four sheared catalogs is described in Secs. 4.1 & 7.4 of [113]. The application of these corrections depends on the details of the shear statistic that is being calibrated.

In this work we adopt a number of approximations that simplify this process. First, we assume that the shear response is independent of environment, and thus

not dependent on the separation of galaxies. Under this assumption, the correction to the shear two-point function is simply the square of the mean response (see section 3.2 in [91]). We further make the assumption that the correction is independent of the relative orientation of galaxies, so that the mean response can be calculated without the shape rotations that are applied when measuring the shear two-point function. We find that the mean response matrices are consistent with being diagonal, which further simplifies the calibration procedure. While these assumptions appear to be valid for the DES Y1 analysis, fully testing the propagation of the full rotated selection response through the shear two-point function is carried out for DES Y3, wherein we find no significant change with respect to the DES Y1 procedure. Furthermore, there should be no additive correction of the response necessary for Metacalibration, due to the symmetric reconvolution function used during the metacalibration process.

## Chapter 2

# Weak Lensing Constraints from DES-Y1 Data

### 2.1 A Model for the Signal

In order to derive cosmology constraints from cosmic shear data, we need two things: a predictive physical model, which we can reasonably assume to underlie the data, and a reliable implementation of that model. This statement implies a number of requirements; first, on the scales fit any systematic deviations from, or effects omitted from, the model must be comfortably subdominant to uncertainties on the data. If this is not the case, our model may compensate for the additional features in the data, resulting in biases. Second, the implementation must be free of bugs and numerically stable at all points within the prior volume. Although



apparently trivial, the testing and code comparison required to produce such as code is a sizeable task (see [59]). Finally, the model must be evaluated quickly at any given point in parameter space. This point is particularly important, given that our cosmological model posterior has  $\sim 15$  parameters that will be described later, and typically requires  $\mathcal{O}(10^6)$  or more realizations.

For all parameter inference presented in this work, we use the approach of Bayesian statistics and assume the *Likelihood function* to be a multivariate Gaussian:

$$\ln\mathcal{L}(\Theta) = -\frac{1}{2} \sum_{i,j} \left( D_i - \tilde{D}_i(\Theta) \right) C_{ij}^{-1} \left( D_j - \tilde{D}_j(\Theta) \right) \quad (2.1.1)$$

where  $\Theta$  is the full parameter vector with a particular set of values,  $D_i$  is the  $i$ th element of the tomographic data vector of length  $N_D = N_\theta N_z (N_z + 1)$ , and  $\tilde{D}_i(\Theta)$  is the corresponding theory prediction. The covariance matrix  $\mathbf{C}$  is a  $N_D \times N_D$  block. In principle  $\mathbf{C}$  is a function of  $\Theta$ , but we follow all previous cosmic shear analyses in the literature in using a fixed covariance matrix, e.g. [59, 101]. The *Posterior distribution* on parameters is evaluated as the product of  $\mathcal{L}(\Theta)$  and the prior  $\mathcal{P}(\Theta)$ , and sampling is carried out within the CosmoSIS<sup>1</sup> [112] framework, using the Multinest [30], emcee [33] and Polychord [39] samplers.

Cosmic shear is a quantity with two components, based on two 2<sup>nd</sup> order angular derivatives of the lensing potential,  $\Phi$  as given by  $\gamma_1$  and  $\gamma_2$ . For points along the 1 axis, these components give a simple definition of the tangential and cross-shear

---

<sup>1</sup><https://bitbucket.org/joezuntz/cosmosis>

components:  $\gamma_t = -\gamma_1$ ,  $\gamma_\times = \gamma_2$ . There are thus three 2-point functions to consider for the E-mode in eq. (1.2.35). However, the expectation value of the cross correlation  $\langle \gamma_t \gamma_\times \rangle$  changes sign under a parity transformation, so in order to conserve parity this contribution must vanish, and this measurement contains no cosmological information. We are then left with 2 correlation functions of interest, which can be constructed from linear combinations of  $\gamma_{t,\times}$  [85]:

$$\xi_{\pm}(\theta) = \langle \gamma_t \gamma_t \rangle \pm \langle \gamma_\times \gamma_\times \rangle. \quad (2.1.2)$$

Notice that this definition represents the correlation functions in *real space*. So far, our definitions have been restricted to Fourier space and boil down to eq. (1.2.44). We thus need to transform from  $C_{\kappa\kappa}(\ell)$  into eq. (2.1.2), which can be done through a Bessel transform assuming the sky is approximately flat for the angular separations of interest (which normally range from 2.5 to 250 arcminutes). We then get

$$\xi_{+/-}^{ij} = \int \frac{\ell d\ell}{2\pi} J_{0/4}(\ell\theta) C_{\kappa\kappa}^{ij}(\ell), \quad (2.1.3)$$

where  $J_{0/4}(x)$  are the 0th/4th order Bessel functions of the first kind.

It is understandable that 2 functions are necessary to characterize the 2pt cosmic shear signal if we connect it to a spin-2 field that can be expressed in terms of a real and an imaginary component,

$$\gamma = \gamma_t + i\gamma_\times,$$

which is equivalent to an amplitude and a rotation angle. We could then re-write eq. (2.1.2) as  $\xi_+ \equiv \langle \gamma \gamma^* \rangle$  and  $\xi_- \equiv \langle \gamma \gamma \rangle$ . As defined,  $\xi_{\pm}$  are often called “natural

components” of the shear field [86], since the linear combination we’ve chosen is such that  $\xi_+$  is invariant under a change in coordinate system.

In practice we do not have direct access to the shear field, but rather estimate it via per-galaxy ellipticities (but see [7] for an alternative approach). Correlating galaxies in a pair of redshift bins  $i, j$  we define,

$$\xi_{\pm}^{ij}(\theta) = \frac{\sum_{ab} w^a w^b (\hat{e}_{t,a}^i \hat{e}_{t,b}^j \pm \hat{e}_{\times,a}^i \hat{e}_{\times,b}^j)}{\sum_{ab} w_a w_b R_a R_b}, \quad (2.1.4)$$

where the sums run over pairs of galaxies  $(a, b)$ , drawn from redshift bins  $(i, j)$ , for which the angular separation falls within the range  $|\theta - \Delta\theta|$  and  $|\theta + \Delta\theta|$ .

Equation 2.1.4 should be thought of as the observational version of our theory calculation that reached eq. (2.1.2). Both  $\xi_+$  and  $\xi_-$  are measured in four tomographic bins for DES Y1, and using twenty log-spaced  $\theta$  bins between 2.5 and 250 arcminutes.

While expression (2.1.4) is general, we set all weights to unity and effectively weight galaxies only through the response matrix  $R$  defined in (1.2.30). The response factors are obtained from Metacalibration (see Section ) and account for shear and selection biases  $R_{\alpha} = R_{\gamma,\alpha} + R_{S,\alpha}$ . Each component of the response is averaged, such that  $R = (R_{11} + R_{22})/2$ . It is also worth bearing in mind here that although the responses are computed on a per-galaxy basis, they are noisy, and so only meaningful on the level of the statistical ensemble within each redshift bin. In DES Y1 [101], the shape components that enter eq. (2.1.4) are not raw ellipticities, but are first corrected for residual mean shear, such that  $\hat{e}_k^i \equiv e_k^i - \langle e_k \rangle_i$ . Here the

lower index  $k$  is an ellipticity component  $k \in (1, 2)$ , and the angle brackets denote averaging galaxies within redshift bin  $i$ .

We show the resulting two point functions as measured in the DES Y1 data in Figure 2.1, extracted from [101], alongside a best fitting theory predictions. Each panel shows a redshift bin pair, and in each one the shaded region shows scales removed by the cuts discussed in the next section. These measurements are made using the software TreeCorr<sup>2</sup> [51].

## 2.2 Systematic Uncertainties

We now turn our attention to the many astrophysical effects that can be present in the signal shown in Figure 2.1. Any such effects that are not included in the model have the potential to bias the model parameters when we estimate their posterior distributions. This is an area of great interest and the core of many present-day weak lensing analyses. While we cannot offer a comprehensive view of this quickly evolving field of research, we approach some of the main systematics that are mitigated in the DES Y1 (and also Y3) analysis.

### 2.2.1 Intrinsic Alignments

Galaxies are not idealised tracers of the underlying matter field, but rather astrophysical bodies, which are subject to local interactions. To account for this added

---

<sup>2</sup><https://github.com/rmjarvis/TreeCorr>

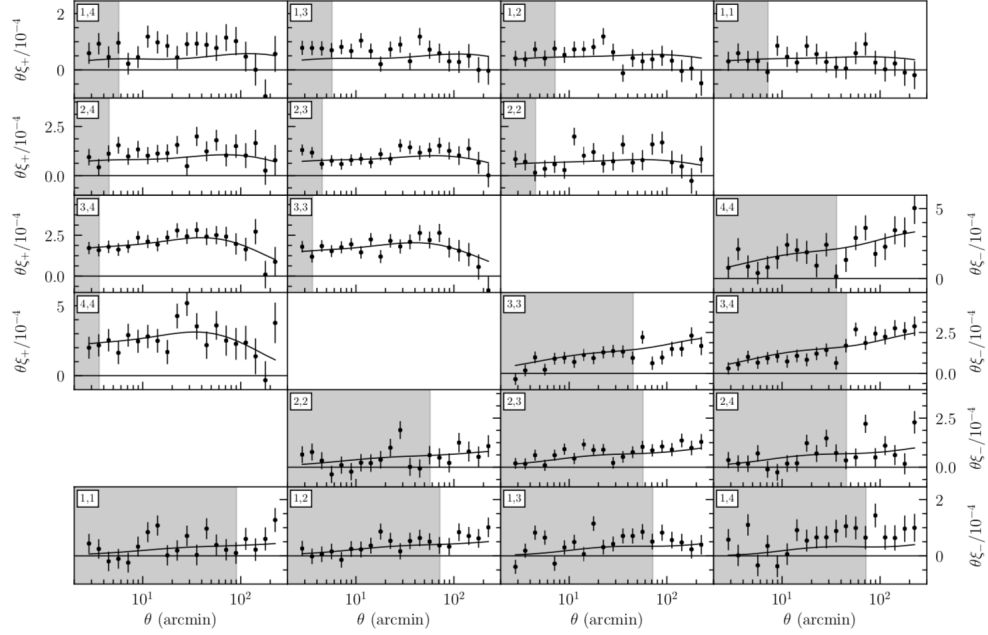


Figure 2.1: The measurement of  $\xi_{\pm}(\theta)$  from the DES Y1 data. Solid lines correspond to the best-fitting cosmological and nuisance parameter values as inferred from their posterior distributions. Each panel corresponds to a different combination of redshift bins, and grey bands correspond to angular scales eliminated from the analysis (see section 2.2).

complexity, the observed shape of a galaxy can be decomposed into two parts, the shear induced by gravitational lensing (G) and the intrinsic shape (I) induced by the local environment:  $\gamma = \gamma^G + \gamma^I$ . In this section, we consider only the correlated intrinsic component rather than the intrinsic “shape noise”, which contributes to the covariance but not the signal.

The term *intrinsic alignments* (IAs) covers two contributions from environmental interactions: (a) intrinsic shape - intrinsic shape correlations between physically nearby galaxies, and (b) shear-intrinsic correlations between galaxies on neighbouring lines of sight. Known as II and GI contributions, respectively, and contributing on similar scales to the cosmological lensing signal, these terms constitute a significant systematic in weak lensing analyses. Including IA contributions, the observed E-mode angular power spectrum is written

$$C_{EE}^{ij}(\ell) = C_{GG}^{ij}(\ell) + C_{GI}^{ij}(\ell) + C_{IG}^{ij}(\ell) + C_{II,EE}^{ij}(\ell). \quad (2.2.1)$$

Nonlinear models of IA, as discussed below, can also produce a non-zero B-mode power spectrum:

$$C_{BB}^{ij}(\ell) = C_{II,BB}^{ij}(\ell). \quad (2.2.2)$$

Assuming the Limber approximation as before, the two IA  $C(\ell)$ s are given by:

$$C_{GI}^{ij}(\ell) = \int_0^{\chi_H} d\chi \frac{W^i(\chi)n^j(\chi)}{\chi^2} P_{GI} \left( \frac{\ell}{\chi}, z(\chi) \right), \quad (2.2.3)$$

and

$$C_{II}^{ij}(\ell) = \int_0^{\chi_H} d\chi \frac{n^i(\chi)n^j(\chi)}{\chi^2} P_{II} \left( \frac{\ell}{\chi}, z(\chi) \right), \quad (2.2.4)$$

These expressions are generic, and are valid regardless of which model is used to predict  $P_{GI}$  and  $P_{II}$ .

It is typically assumed that the correlated component of galaxy shapes is determined by the large-scale cosmological tidal field. The simplest relationship, which should dominate on large scales and for central galaxies, involves the “tidal alignment” of galaxy shapes, producing a linear dependence [20, 46]. In this case, one can relate the intrinsic shape component the gravitational potential at the time of formation:

$$(\gamma_1^I, \gamma_2^I) = C_1(z) \left( \frac{\partial^2}{\partial x^2} - \frac{\partial^2}{\partial y^2}, 2 \frac{\partial^2}{\partial x \partial y} \right) \phi_*, \quad (2.2.5)$$

where the proportionality factor  $C_1(z)$  captures the response of intrinsic shape to the tidal field and is discussed below. More complex alignment processes, including “tidal torquing”, relevant for determining the angular momentum of spiral galaxies, are captured in a nonlinear perturbative framework, which we refer to as “TATT” (Tidal Alignment and Tidal Torquing; [15]). Although the terms in the model can be associated with physical mechanisms, they can also be viewed as effective contributions to intrinsic shape correlations from small-scale physics. See also [84, 102, 107] for further discussion of the perturbative approach and [34] for a halo model treatment of IA.

Within the TATT framework, three parameters capture the relevant responses to the large-scale tidal fields:  $C_1$ ,  $C_2$ , and  $C_\delta$ , corresponding respectively to a linear

response to the tidal field (tidal alignment), a quadratic response (tidal torquing), and a response to the product of the density and tidal fields (see [15] for more details). To date, the most frequently used intrinsic alignment model in the literature is known as the Nonlinear Alignment Model (NLA; [16,45]), an empirically-based modification of the Linear Alignment (LA) model of [20,46], in which the fully nonlinear tidal field is used to calculate the tidal alignment term. Within the ‘‘TATT’’ framework, the NLA model corresponds to only  $C_1$  being non-zero. Within this model, the the GI and II power spectra have the same shape as the nonlinear matter power spectrum, but are modulated by  $C_1(z)$  (note the sign convention):

$$P_{\text{GI}}(k) = -C_1(z)P_{\kappa}(k), \quad P_{\text{II}}(k) = C_1^2(z)P_{\kappa}(k). \quad (2.2.6)$$

More generally, in the TATT model, the GI and II power spectra are constructed according to equations 37-39 in [15], with the  $k$ -dependent contributions modulated by the prefactors  $C_1$ ,  $C_2$ , and  $C_{\delta}$ . In this work, these  $k$ -dependent terms are evaluated using FAST-PT [29,67], as implemented in COSMOSIS. The model is set out in some depth in [15] and we refer the reader to that paper for technical details. The prefactors are given by

$$C_1(z) = -A_1 \bar{C}_1 \frac{\rho_{\text{crit}} \Omega_{\text{m}}}{D(z)} \left( \frac{1+z}{1+z_0} \right)^{\alpha_1}. \quad (2.2.7)$$

$$C_2(z) = 5A_2 \bar{C}_1 \frac{\rho_{\text{crit}} \Omega_{\text{m}}}{D^2(z)} \left( \frac{1+z}{1+z_0} \right)^{\alpha_2}. \quad (2.2.8)$$

$\bar{C}_1$  is a normalisation constant, by convention fixed at a value  $\bar{C}_1 = 5 \times 10^{-14} M_{\odot} h^{-2} \text{Mpc}^2$ , obtained from SuperCOSMOS (see [17]). Related to this convention, the leading



factor of 5 in equation 2.2.8 is included to account for the difference in the windowed variance produced by the TA and TT power spectra. With this factor included, the TA and TT contributions to  $P_{\text{II}}$  at  $z = 0$ , averaged over this window, should be roughly the same if  $A_1 = A_2$ , aiding in the interpretation of the best fitting values. Note that this is a matter of convention only, and does not affect our final cosmological results in any way.

The denominator  $z_0$  is a pivot redshift, which we fix to the value 0.62.<sup>3</sup> The dimensionless amplitudes  $(A_1, A_2)$  and power law indices  $(\alpha_1, \alpha_2)$  are free parameters in this model.

As mentioned above, the model also includes a  $C_{1\delta}$  contribution, corresponding to the product of the density and tidal fields. This term is originally motivated by the modulation of the IA signal due to the galaxy density weighting (i.e. the fact that the shape field is preferentially sampled in overdense regions [14]). In this case, within the TATT model, we have

$$C_{1\delta} = b_{\text{TA}} C_1, \tag{2.2.9}$$

where  $b_{\text{TA}}$  is the linear bias of source galaxies contributing to the tidal alignment signal. In our baseline analysis, rather than fixing  $b_{\text{TA}}$  to this bias value, we sample over it with a wide prior, allowing the  $C_{1\delta}$  contribution to capture a broader range of

---

<sup>3</sup>This value was chosen in Y1 to be approximately equal to the mean source redshift. Although our cosmological results are insensitive to this choice, it is relevant to how one interprets our IA constraints, and we maintain this value for the Y3 analysis

nonlinear alignment contributions. We note that this is a departure from previous studies to have used this model [15, 82, 101], all of which held  $b_{\text{TA}} = 1$  fixed.

As noted above, in the limit  $A_2, b_{\text{TA}} \rightarrow 0$ , the TATT model reduces to the NLA model. It is thus useful to think of NLA as a sub-space of the more complete TATT model, rather than a distinct alternative model. Given the sensitivity of IAs to the details of the galaxy selection, and in the absence of informative priors, we choose to marginalise all five IA parameters ( $A_1, A_2, \alpha_1, \alpha_2, b_{\text{TA}}$ ), governing the amplitude and redshift dependence of the IA terms, with wide flat priors. While a redshift evolution in the form of a power-law, captured by the index  $\alpha_i$ , is a common assumption, the  $A(z)$  coefficient could, in theory, have a more complicated redshift dependence. We seek to test the impact of this assumption by rerunning our analysis with a more flexible parameterization, whereby the IA amplitude in each redshift bin  $A_i$  is allowed to vary independently. It is finally worth remarking that the TATT model predicts a non-zero B-mode power spectrum  $P_{\text{II},BB}$ . We typically find B-modes small enough so they can be neglected.

### 2.2.2 Nonlinear Power Spectrum and Baryons

We have so far implied that an exact prediction can be made for the matter power spectrum  $P(k)$ . This is not, however, entirely true. There exist significant uncertainties regarding how Dark Matter clusters on relatively small astrophysical scales (of order 10 Mpc) that come mostly from the fact that numerically computing  $P(k)$

generally makes the assumption that the overdensities being described are small, such that the density contrast defined in eq. (1.1.8) is  $\delta \ll 1$ . This approximation ensures that structure formation equations such as the continuity equation remains linear in  $\delta$ . That is certainly not the case for the most massive structures in the universe, galaxy clusters, which normally reach  $\delta \gtrsim 200$ , in which case we have to deal with *nonlinear* scales in the matter power spectrum.

Furthermore, complicated baryonic feedback processes become important when overdensities are large, and the assumption that gravity alone dictates the distribution of matter starts breaking down. Approximations in the nonlinear clustering of matter on small scales, including the impact of baryonic effects, are a key modeling choice for the cosmic shear signal.

To model the nonlinear matter power spectrum, we use HALOFIT [94] with updates from [99]. These prescriptions are basically fitting formulas for different cosmologies which are calibrated by expensive sets of simulations.

Another component that can modify the power spectrum on nonlinear scales<sup>4</sup> is a nonzero neutrino mass. Generally, neutrinos do not cluster on scale below their free-streaming length, so they can cause a suppression on the matter clustering. The impact of neutrino mass on the matter power spectrum is implemented in HALOFIT from [13], which introduces some additional uncertainty of potentially up to 20%. Our definition of angular scales that are removed from the analysis,

---

<sup>4</sup>Neutrinos also affect the linear regime of the power spectrum by increasing the clustering amplitude on very large physical scales.

however, alleviates concerns regarding the neutrino mass, since they encompass any physical scales that could be affected by neutrino physics.

Since the modeling of nonlinear astrophysics is highly uncertain, our fiducial analysis removes scales that could be significantly biased by baryonic effects. For scale selection, these effects are modeled as a re-scaling of the nonlinear matter power spectrum

$$P(k, z) \rightarrow \frac{P(k, z)_{\text{DM+Baryons}}}{P(k, z)_{\text{DM}}} P(k, z) \quad (2.2.10)$$

where “DM” refers to the power spectrum from the OWLS (OverWhelmingly Large Simulations project) dark-matter-only simulation, while “DM+Baryon” refers to the power spectrum from the OWLS AGN simulation [83, 104]. OWLS is a suite of hydrodynamic simulations with different sub-grid prescriptions for baryonic effects. We use this particular OWLS simulation for two reasons. First, it is the one which deviates most from the dark matter-only case in the relevant scales of the matter power spectrum; given we are cutting scales based on the size of this deviation, this is a conservative choice. Secondly, McCarthy et al. [66] find that of the OWLS, the AGN simulation best matches observations of galaxy groups in the X-ray and optical, so arguably it is the most realistic.

We remove any angular scales  $\theta_i$  from the  $\xi_{\pm}(\theta_i)$  data vector that would have a fractional contribution from baryonic effects exceeding 2% at any physical scale. This removes a significant number of data points, particularly in  $\xi_{-}$ , on small scales. In general we find that our cuts in scale to remove parts of the cosmic shear data

vector contaminated by potential baryonic effects are sufficient to alleviate any potential bias due to uncertainties in modeling nonlinear matter clustering.

### 2.2.3 Point-Spread Function Modeling Errors

A robust treatment of the Point-Spread Function (PSF) is crucial for unbiased cosmic shear measurements. The PSF is a “blurring” of galaxy images caused by a combination of many sources: atmospheric turbulence, telescope optics, etc. These contamination manifest on galaxy images as a convolution of the image with a PSF kernel. This kernel needs to be modeled and the PSF deconvolved from galaxy images in order for an appropriate measurement of the shapes  $(e_1, e_2)$  to be obtained.

Imperfect modeling or deconvolution of the PSF can produce coherent additive and multiplicative shear biases, both of which contaminate the cosmic shear signal [72]. In [113], we identified spatially correlated ellipticity errors in the PSF modeling. We model the impact of PSF model ellipticity errors on the inferred shear using the linear relation

$$\delta e_{\text{sys}} = \beta(e_p - e_*) = \beta q \tag{2.2.11}$$

where  $e_p$  is the PSF model ellipticity,  $e_*$  is the true PSF ellipticity and therefore  $q$  is the PSF model ellipticity residual. We use this model as a first-order approximation for realistic PSF uncertainties. If, as well as PSF modeling errors, there are also errors in the deconvolution of the PSF model from the galaxy image, one might

also expect a systematic bias that is proportional to the PSF model ellipticity (sometimes this term is referred to as PSF leakage), such that the model for the shear bias becomes

$$\delta e_{\text{sys}} = \alpha e_p + \beta q \quad (2.2.12)$$

Note that we have no reason to expect non-zero  $\alpha$  from Metacalibration, since it uses a circularized PSF (that is, the PSF is first rotated several times about its center before the deconvolution, so there is no preferred “leakage direction” and therefore no  $\alpha$  term). On the other hand we expect all shear estimation algorithms to have a non-zero  $\beta$ ; even a ‘perfect’ shear estimator has to assume a PSF model, and errors in that PSF model will propagate to errors in the shear estimation (Paulin-Henriksson et al. [72] estimate  $\beta$  for an un-weighted moments shear estimator). In [113], we measure a significant correlation between the estimated shear and the PSF model ellipticity. This could be evidence for nonzero  $\alpha$ , but could also arise from correlations between the PSF model ellipticity and the PSF ellipticity residuals even for  $\alpha = 0$ . We demonstrate below that the latter is the most likely explanation.

While we have an estimate of  $e_p$  at each galaxy position, we can only estimate  $q$  at the position of stars. This comes from the very nature of PSF estimation. Since stars are too small to be resolved by the telescope, their brightness profile is formally a delta function on the CCD pixel where the star is located. Therefore, since the convolution of a delta function with some kernel results in the kernel itself, the observed shape of the star becomes the estimate for the PSF kernel.

Since PSF's are known at the location of stars, we use cross-correlations between the galaxy and star samples in order to simultaneously estimate  $\alpha$  and  $\beta$ . To do this, we use the following cross-correlations

$$\langle e_{\text{obs}} e_p \rangle = \alpha \langle e_p e_p \rangle + \beta \langle q e_p \rangle \quad (2.2.13)$$

$$\langle e_{\text{obs}} q \rangle = \alpha \langle e_p q \rangle + \beta \langle q q \rangle \quad (2.2.14)$$

Note that in the above, the angle-brackets as usual denote correlations of spin-2 quantities; we use the  $\xi_+(\theta)$  statistic for all of these. The equations above provide a means to find  $\alpha$  and  $\beta$ , which are taken to be free parameters, because we can measure the correlations  $\langle e_p e_p \rangle$ ,  $\langle q e_p \rangle$ ,  $\langle e_p q \rangle$  and  $\langle q q \rangle$  from the star catalog described in [113]. Solving for  $\alpha$  and  $\beta$  we find, as expected, that  $\alpha$  is consistent with zero and  $\beta \sim -1$ . Constraints for each separate redshift bin are shown in Figure 2.2. Given these estimates of  $\beta$ , we estimate the impact of PSF model ellipticity errors on our cosmological parameter inference as follows.

The expected systematic contamination of  $\xi_{ij}$ , where  $ij$  denotes the redshift bin pair, is

$$\xi_+^{\text{PSF}} = \langle \beta_i \beta_j \rangle (\langle q q \rangle - \langle q_1 \rangle^2 - \langle q_2 \rangle^2) \quad (2.2.15)$$

where the second and third terms on the RHS arise because we are subtracting the mean ellipticity from each tomographic bin to correct for scale-independent additive biases. We expect that on large scales (where additive biases are most significant),  $\beta$  is uncorrelated between galaxies, and therefore make the assumption that  $\langle \beta_i \beta_j \rangle =$

| Redshift bin | $\beta_{\text{METACALIBRATION}}$ |
|--------------|----------------------------------|
| 1            | $-0.72 \pm 0.26$                 |
| 2            | $-0.99 \pm 0.32$                 |
| 3            | $-0.72 \pm 0.32$                 |
| 4            | $-1.31 \pm 0.43$                 |

Figure 2.2: Constraints on  $\beta$ , the proportionality constant when assuming a linear relationship between inferred shear and PSF model ellipticity residual. Errors quoted are 68% confidence intervals. Extracted from [101].

$\langle\beta_i\rangle\langle\beta_j\rangle$ . The measured  $\langle qq\rangle$  (also known as the first “ $\rho$ -statistic”,  $\rho_1$  [80]), and the best-fit  $\beta$  values from Figure 2.2, we produce a contaminated prediction of our data vector, which we then analyze using our parameter estimation framework to check for biases in cosmological parameters that this level of contamination would induce. We thus verify that the level of impact on cosmological parameters is entirely negligible.

## 2.2.4 Photometric Redshift Uncertainties

A tomographic cosmic shear measurement requires an assignment of each source galaxy to a redshift bin  $i$ , and its interpretation requires an accurate estimation of the redshift distribution of galaxies in each redshift bin,  $n_i(z)$ . The procedures for doing so, and for assigning uncertainties to  $n_i(z)$ , are described fully in [48]. In this analysis, galaxies in the shape catalogs are assigned to the four redshift bins



listed shown in Figure 1.3 by the mean of the photo- $z$  posterior  $p(z)$  estimated from DES *griz* flux measurements. The redshift distribution of each bin is constructed by stacking a random sample from the  $p(z)$  of each galaxy. The photo- $z$  posteriors used for bin assignment and  $n_i(z)$  estimation in the fiducial analysis of DES Y1 are derived using the Bayesian photometric redshift (BPZ) methodology [6].

One notable complication when compared to previous cosmic shear studies is the direct correction of photo- $z$  induced selection biases in Metacalibration, which requires calculating the impact that shearing a galaxy image has on the photometric redshift determination. We thus construct a total of six versions of our photo- $z$  estimates based on various photometric measurements: a) the original Multi-Epoch Multi-Object Fitting (MOF) *griz*-band photometry, b) the measurements of *griz*-band photometry from the unsheared Metacalibration galaxy fit, and c) four versions of the *griz*-band photometry from the four sheared Metacalibration galaxy fits. In all cases, the redshift distribution  $n_i(z)$  of each bin is reconstructed using BPZ estimates from MOF, which gives a better estimate of the shape of the redshift distribution.

To calculate the Metacalibration selection bias correction due to redshift selection, we then construct the galaxy selection in each tomographic bin from the photo- $z$  estimates using both the unsheared Metacalibration photometry and the four sheared photometries. We use these five selections, in addition to all other selection criteria such as signal-to-noise cuts, to construct the component of the

selection bias correction  $R_s$  utilized in Section 2.1.

Our adopted model for the redshift distribution assumes that the true redshift distribution in each bin is related to our measured distribution such that:

$$n_i(z) \rightarrow n_i(z + \Delta z), \quad (2.2.16)$$

where  $\Delta z$  is the difference in the mean redshift of the true and measured  $n(z)$ . Notice that this effect propagates down to the correlation functions  $\xi_{\pm}$  starting from the kernel definition in eq. (1.2.40). This is a sufficient description of the photo- $z$  uncertainty for the current cosmic shear analysis, since deviations in the shape of the  $n(z)$  are subdominant to the impact of the mean  $z$ , for reasonable variance in the shape at the level of precision necessary for the DES Y1 analysis.

We derive constraints on  $\Delta z_i$  for the estimated redshift distributions by comparison of the mean redshift in each bin to that from two independent methods:

1. The mean, high-quality photo- $z$  of a sample of galaxies from the COSMOS2015 catalog [62], matched to resemble the source galaxies in *griz* flux and pre-seeing size [48].

2. In the lowest three redshift bins, the clustering of source galaxies with *Red-magic*<sup>5</sup> galaxies at  $0.15 < z < 0.85$ , for which accurate and precise photometric redshifts can be derived from DES photometry.

We will refer to these as the ‘COSMOS’ and ‘WZ’ redshift validation methods,

---

<sup>5</sup>We will define this galaxy sample later, when combining cosmic shear with galaxy clustering results in DES Y1

respectively. Their constraints on  $\Delta z_i$  are independent and consistent for the first three bins and of comparable uncertainty. We thus combine them to provide a Bayesian prior on the systematic parameters  $\Delta z_i$  at the level of  $\pm 0.02$ .

Estimation of the redshift distribution of the lensing source galaxies is one of the most difficult components of a broad-band cosmic shear survey like DES. Along with the use of two independent methods to constrain  $\Delta z_i$ , Sec. IX C in [101] has presented several tests of the robustness of the DES Y1 cosmological results to the methods and assumptions of our  $n_i(z)$  estimates.

### 2.2.5 Multiplicative Shear Errors

Some systematic uncertainties can cause a *multiplicative* error in the ellipticity estimates. One could characterize multiplicative (and also additive) errors as

$$e^{a,i} = (1 + m_i)e_{\text{true}}^{a,i} + c_i \quad (2.2.17)$$

where  $a$  refers to the two shear components ( $a = 1, 2$ ), and  $i$  refers to a redshift bin. In DES Y1, we show that no additive errors  $c_i$  can cause a significant impact on our analysis, in particular those coming from PSF errors in equation (2.2.11), so we simply consider  $c_i \rightarrow 0$  from now on. The multiplicative bias  $m_i$ , however is harder to rule out. It can come, in principle, from the PSF leakage explored in the previous section (which was actually shown to be negligible in DES Y1) as well as *blending* errors, whereby the shapes of galaxies whose images overlap on a given line of sight are severely biased. If multiplicative biases cannot be ruled out, they

propagate into biases on the tomographic correlation functions that look like

$$\xi_{\pm}^{ij} = (1 + m_i)(1 + m_j)\xi_{\pm,\text{true}}^{ij}. \quad (2.2.18)$$

Since we cannot rule out the impact of these multiplicative errors, we perform image simulations to determine a prior on how large these contaminations can be, and eventually marginalize over the nuisance parameters  $m_i$ ,  $m_j$  in our inference. We use a Gaussian prior on  $m_i$  of  $0.012 \pm 0.023$  for Metacalibration.

## 2.3 Covariance Matrix

The previous sections motivated a large part of the analysis. Since we want to be able to compute a Likelihood function to predict a Posterior on cosmological parameters, we also need a *covariance matrix* for the data and its inverse in order to compute the likelihood expressed in eq. (2.1.1). Obtaining covariance matrices is an area of active research; methods can be broadly separated into 3 categories: estimation from numerical simulations, estimation from data directly, and analytical modeling/computation. We briefly summarize the current state of affairs as it is most relevant for this work.

Firstly, estimating the precision matrix from a set of large, high-resolution numerical simulations using a standard Maximum Likelihood estimator is computationally prohibitively expensive even for single probe analyses [26] (like cosmic shear alone); this is even more an issue for the multi-probe case (as when including galaxy

clustering probes), where covariances are substantially larger. The main reason for these computational costs is the intrinsic noise properties of the estimator, which means we require a large ensemble of independent realizations of numerical simulations. Promising approaches can be separated into two main categories. The first is data compression, which reduces the dimensionality of the covariance matrix. Second, recently new estimators with significantly improved noise properties are being explored.

As a second method, covariance matrices from the data directly (through bootstrap or Jackknife estimators) avoids any assumptions about cosmological or other model parameters that need to be specified in the numerical simulation approach (and in the theoretical modeling approach). However, given the limited survey area, it is difficult to obtain a sufficiently large number of regions of sky for the method to work, and it is unclear if these regions can be treated as independent.

Finally, the analytic computation of weak lensing covariances was detailed in Schneider et al. [87] and Joachimi et al. [52], which derive straightforward expressions for Fourier and configuration space covariances under the assumption that density field is Gaussian, so that the four-point correlation of the density field can be expressed as the product of two-point correlations. On small and intermediate scales this assumption is inaccurate; analytical expressions of non-Gaussian weak lensing covariances were derived in e.g. Takada and Jain [98]. These expressions were generalized to a  $3 \times 2$ pt analysis in [58]. The main advantage of an analytical

(inverse) covariance matrix is the lack of a noisy estimation process, which substantially reduces the computational effort in creating a large number of survey realizations; the disadvantage is that the modeling of the non-Gaussian covariance terms, which employs a halo model is less precise compared to sophisticated numerical simulations.

For the DES Y1 analysis we implemented the third option, analytical modeling, for several reasons. First, the software CosmoLike, set in detail in [58], has an analytical covariance implementation that is fast enough to compute a configuration space covariance. Second, as noted above there is no estimator noise in this calculation. Third, the non-Gaussian terms in our covariance are sub-dominant and hence corresponding uncertainties are unimportant. To validate the analytic option, we generate 1,200 “lognormal” realizations of the DES Y1 survey footprint using the software FLASK [110]. The resulting covariance matrix can be seen in Figure 2.3, which shows both the analytic estimate as well as the FLASK estimates.

## 2.4 Cosmological Constraints in $\Lambda$ CDM wCDM

We finally have all the necessary pieces to obtain the cosmological constraints from the cosmic shear data measured and shown in Figure 2.1. But firstly, we should summarize the priors on cosmology and nuisance parameters that are used for the Bayesian analysis. These priors are shown in Figure 2.4. Notice, in particular, that we use the simplest model for the intrinsic alignment contamination, the NLA model

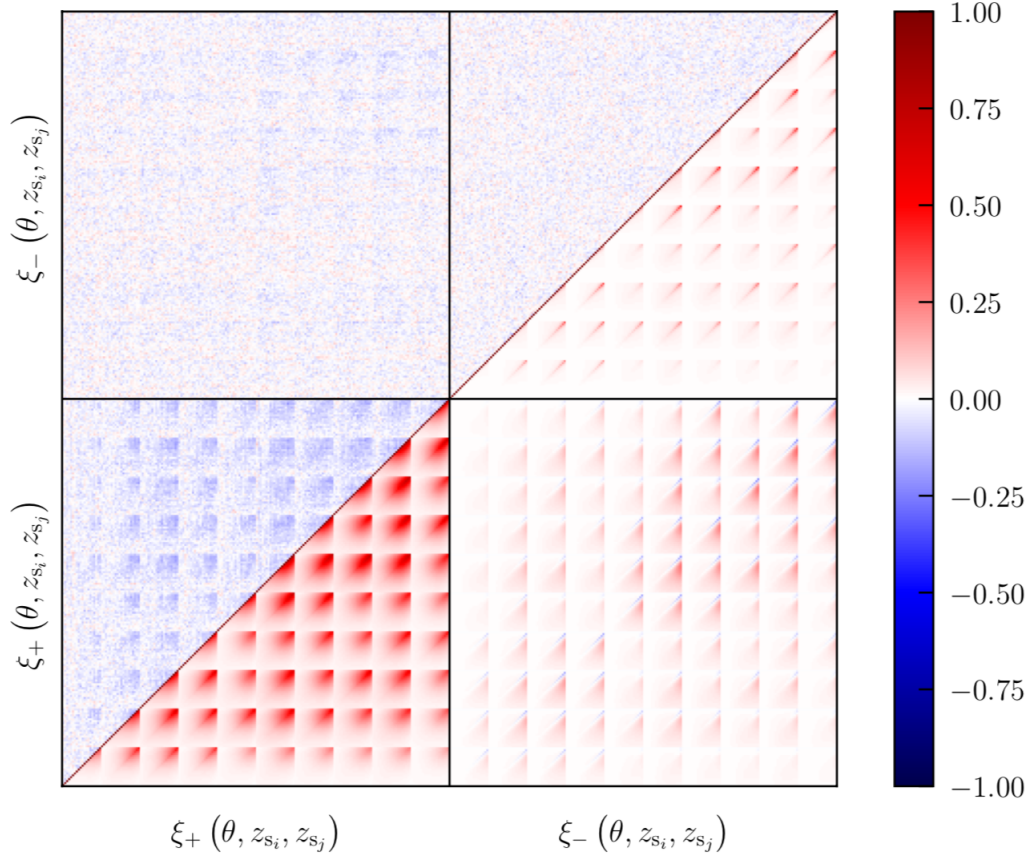


Figure 2.3: The covariance matrix for the cosmic shear data. Since the covariance matrix is symmetric, we plot on the upper triangle the difference between the FLASK and analytic CosmoLike estimates, and in the bottom triangle the CosmoLike estimate alone. The important aspect of this plot is that the upper triangle shows mostly residuals around zero and almost no actual structure, which means the validation of the analytic covariance with FLASK survey realizations is fit for our purposes.

expressed in eq. (2.2.6), which is parametrized by 2 parameters: an amplitude  $A$  and a redshift evolution power-law parameter  $\eta$ .

We make a distinction of 2 different cosmological models under consideration:  $\Lambda$ CDM and  $w$ CDM. The first one corresponds to the vanilla cosmological model wherein Dark Energy is a cosmological constant  $\Omega_\Lambda$  shown in eq. (1.1.5), which implies that the equation of state parameter for dark energy is fixed at  $w = -1$ . When we free this parameter and marginalize over it, we have a model in which dark energy is dynamical and evolves in redshift. Presently, there are no statistically significant cosmological measurements that infer  $w \neq -1$ .

Given the size and quality of the DES Y1 shape catalogs, we are able to make a highly significant statement about the robustness of the standard  $\Lambda$ CDM cosmological model. Our measurements of cosmic shear probe the evolution of nonlinear fluctuations in the underlying matter field and expansion of space across a very large volume around  $z \approx 0.6$ . By comparison, equally constraining measurements of the CMB at  $z = 1100$  use information from linear perturbations in the radiation field to constrain the same model eight billion years before light left the galaxies we now observe in DES. Comparing the prediction of these very different probes at the same redshift via the parameter  $S_8$  allows us to test whether these results are consistent within the  $\Lambda$ CDM model to high precision. We define  $S_8$  as a lensing amplitude parameter that exploits the degeneracy between the matter density  $\Omega_m$



| Parameter                                     | Range           | Prior          |
|---|-----------------|----------------|
| <b>Cosmological</b>                           |                 |                |
| $A_s \times 10^9$                             | 0.5 ... 5.0     | Flat           |
| $\Omega_m$                                    | 0.1 ... 0.9     | Flat           |
| $\Omega_b$                                    | 0.03 ... 0.07   | Flat           |
| $\Omega_\nu h^2$                              | 0.0006 ... 0.01 | Flat           |
| $H_0$ (km s <sup>-1</sup> Mpc <sup>-1</sup> ) | 55 ... 90       | Flat           |
| $n_s$   | 0.87 ... 1.07   | Flat           |
| $w$   | -2.0 ... -0.333 | Fixed/Flat     |
| $\Omega_k$                                    | 0.0             | Fixed          |
| $\tau$  | 0.08            | Fixed          |
| <b>Systematic</b>                             |                 |                |
| $(m^1 - m^4) \times 10^2$                     | -10 ... 10      | $1.2 \pm 2.3$  |
| $\Delta z^1 \times 10^2$                      | -10 ... 10      | $0.1 \pm 1.6$  |
| $\Delta z^2 \times 10^2$                      | -10 ... 10      | $-1.9 \pm 1.3$ |
| $\Delta z^3 \times 10^2$                      | -10 ... 10      | $0.9 \pm 1.1$  |
| $\Delta z^4 \times 10^2$                      | -10 ... 10      | $-1.8 \pm 2.2$ |
| <b>Astrophysical</b>                          |                 |                |
| $A$   | -5.0 ... 5.0    | Flat           |
| $\eta$  | -5.0 ... 5.0    | Flat           |
| $z_0$   | 0.62            | Fixed          |

Figure 2.4: Priors on cosmological and nuisance parameters utilized in the DES Y1 analysis published in [101].

and the variance in a  $8\text{Mpc } h^{-1}$  radius  $\sigma_8$  as defined in eq. (1.1.14) as

$$S_8 = \sigma_8 \sqrt{\Omega_m/0.3}. \quad (2.4.1)$$

While this parameter picks out only the well constrained amplitude of the correlation functions  $\xi_{\pm}$ , we can simply recast the entire discussion on Section 1.1 regarding the  $\sigma_8$  tension in terms of this new parameter.

Using the fiducial modeling choices described in the previous sections, we use cosmic shear from the first year of the Dark Energy Survey to constrain both the  $\Lambda\text{CDM}$  and  $w\text{CDM}$  models with varying neutrino mass to produce tight cosmological constraints from cosmic shear. In [2], our cosmic shear results are further combined with galaxy-galaxy lensing and galaxy clustering to significantly improve these constraints. When comparing with external data, it is important to note that we vary  $\Omega_{\nu}h^2$  in our fiducial analysis, and thus all results we compare to, and so the central values and uncertainties of parameters may differ from those previously published for these data.

We marginalize over a total of 6 cosmological parameters in the fiducial  $\Lambda\text{CDM}$  model, including a free neutrino mass density, and 10 systematic or astrophysical parameters. These are listed in 2.4. Our fiducial  $\Lambda\text{CDM}$  constraints in the  $\sigma_8 - \Omega_m$  and  $S_8 - \Omega_m$  planes are shown in Figure 2.5. The DES Y1 cosmic shear constraints are shown by the gray filled contours, while the previous best real-space cosmic shear constraints from the KiDS survey [44] are shown in blue, and Planck constraints from the CMB [75] in filled green, for comparison. Both 68% and 95% confidence

levels are shown. For consistency, previous constraints have been reanalyzed in the parameter space used in this work (see Fig. 2.4), including varying  $\Omega_\nu h^2$ . We show the impact of fixing that neutrino parameter in our fiducial  $\Lambda$ CDM analysis in Fig. 2.6.

These constraints on  $S_8$  are also visually summarized in Fig. 2.7, where we distinguish variations on the fiducial setup that are not necessarily expected to give consistent results (e.g., by neglecting astrophysical systematics) by an asterisk. We find a 3.5% fractional uncertainty on  $S_8 = 0.782 \pm 0.027$  at 68% CL, which is a factor of 2.5 improvement over the constraining power of our Science Verification results. We see similar improvements in the constraint on  $\Omega_m$ , which is more representative of the gain in the direction of degeneracy. We expect further significant improvements with subsequent years of DES data such as DES Y3, which are more than tripling the sky coverage of our shape catalogs and double the effective integrated exposure time per galaxy.

For  $w$ CDM, we marginalize over a total of 7 cosmological parameters, including a free neutrino mass density, and 10 systematic or astrophysical parameters. These are again listed in Fig. 2.4. Our fiducial  $w$ CDM constraints are shown in Fig. 2.8. We find a 4.8% fractional uncertainty on  $S_8 = 0.777 \pm 0.036$  at 68% CL, which is more than a factor 2 improvement over the constraining power of our Science Verification results. We find a dark energy equation-of-state  $w = 0.95 \pm 0.33$  using DES cosmic shear alone.

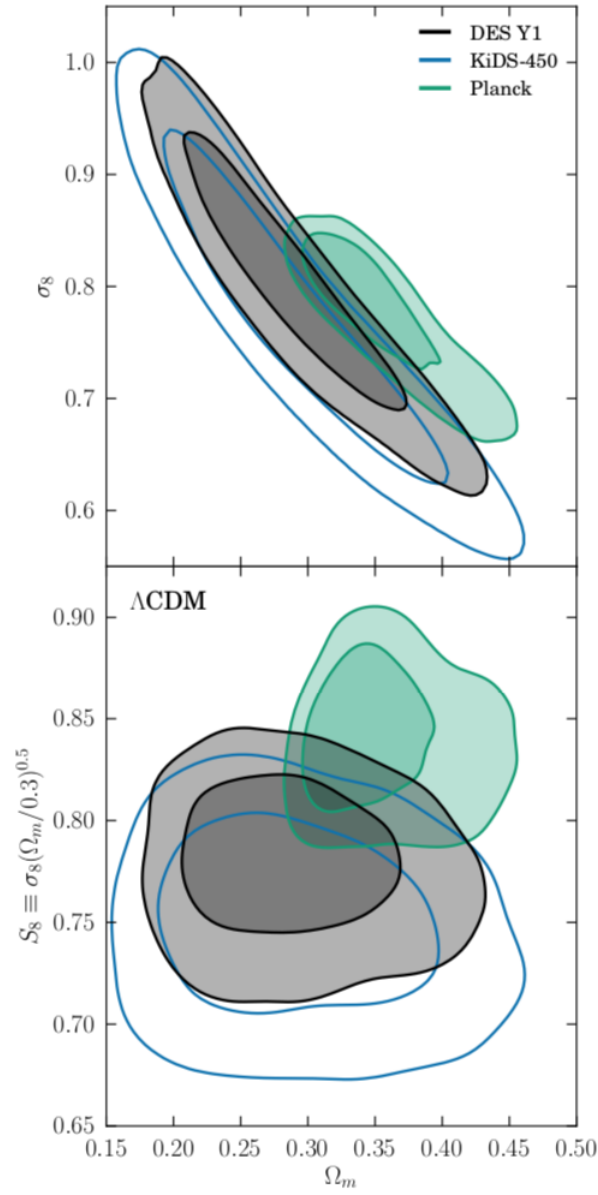


Figure 2.5: The posterior distribution on cosmological parameters from DES Y1 [101], KiDS [44] and Planck [75]. The  $S_8$  tension referred to in Section 1.1 is interpreted in this figure as the mild inconsistency between results from the Planck satellite and low- $z$  probes such as DES and KiDS.

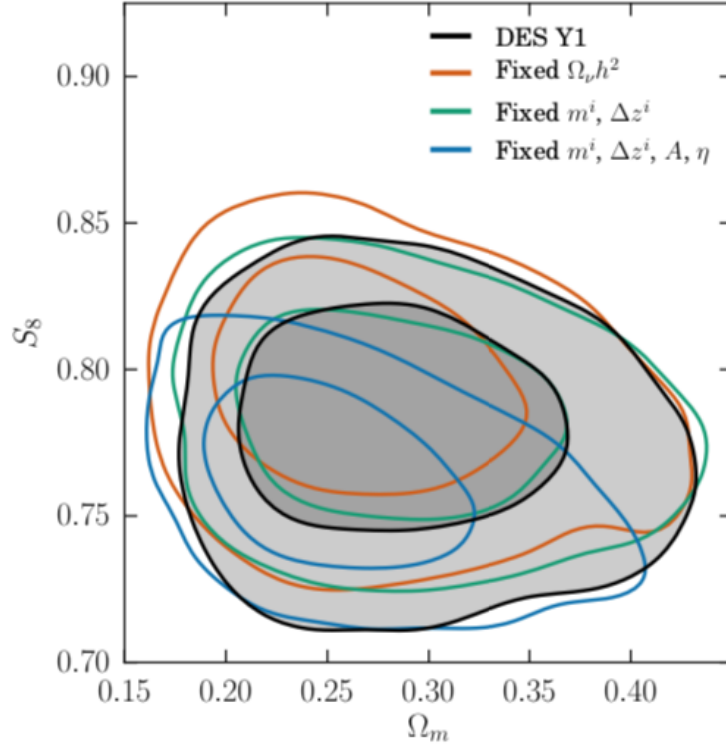


Figure 2.6: The posterior distribution on cosmological parameters from DES Y1 [101] while fixing the neutrino mass parameter  $\Omega_\nu h^2$  as well as changing analysis choices regarding the nuisance parameters  $\Delta z$  and shear calibration biases  $m_i$ .

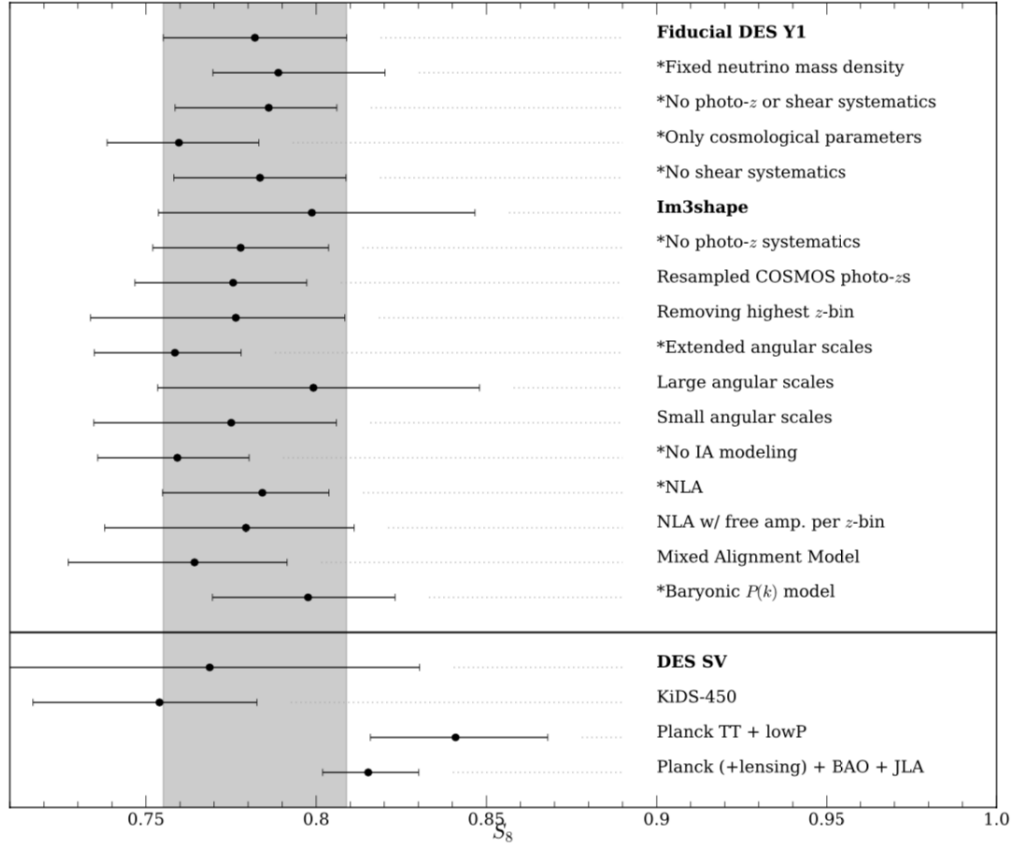


Figure 2.7: The marginalized 1-D posterior distribution on  $S_8$  from DES Y1 [101], under different assumptions and analysis choices. The remarkable fact that any specific choice of parametrization leads to differences within  $1\sigma$  (68% C.L.) of the fiducial constraints is reassuring and shows the robustness of our cosmic shear results.

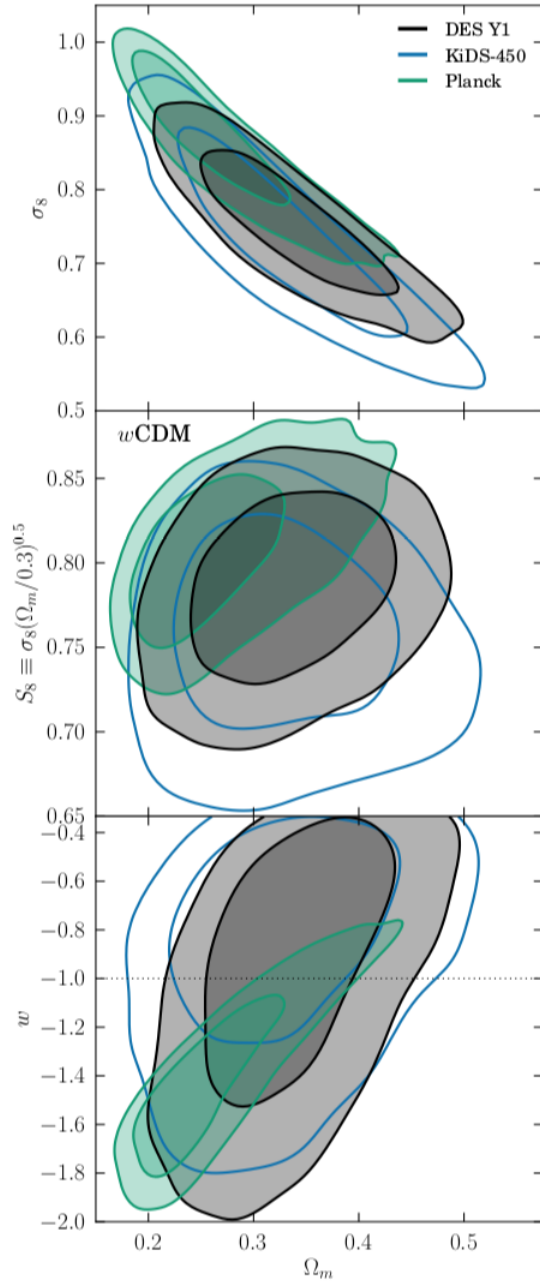


Figure 2.8: The marginalized 2-D posterior distributions in  $w$ CDM from DES Y1 [101]. While cosmic shear alone has a relatively weak constraining power on  $w$ , we obtain  $w = 0.95 \pm 0.33$ , a result which is consistent with  $\Lambda$ CDM at 68% CL.

While we find an equally good fit for  $w$ CDM as we did for  $\Lambda$ CDM, we can further compare the relative Bayesian evidence for each model via the Bayes factor. The Bayesian evidence, or probability of observing a dataset  $\mathbf{D}$  given a model  $M$  with parameters  $\mathbf{p}$ , is

$$P(\mathbf{D}|M) = \int d^N p P(\mathbf{D}|\mathbf{p}, M)P(\mathbf{p}|M) \quad (2.4.2)$$

and the Bayes factor comparing the evidence for the  $w$ CDM and  $\Lambda$ CDM models is then

$$K = \frac{P(\mathbf{D}|wCDM)}{P(\mathbf{D}|\Lambda CDM)}. \quad (2.4.3)$$

The interpretation of the Bayes factor can be characterized in multiple ways, e.g [56].

We find  $\log(K) = 1.4$ , which indicates no preference for a model which allows  $w \neq 1$ .



# Chapter 3

## Constraints on Extended Cosmological Models

### 3.1 Revisiting the $\Lambda$ CDM Paradigm

We now turn our attention to models that go beyond the usual explorations of what cosmological model is more appropriate to describe the observable universe<sup>1</sup>. Let us recall what we know of the vanilla cosmological paradigm.

Evidence for dark matter [114] and the discovery of cosmic acceleration and thus evidence for dark energy [73, 78] were pinnacle achievements of cosmology in the 20th century. Yet because of the still-unknown physical mechanisms behind these two components, understanding them presents a grand challenge for the present-day generation of cosmologists. Dark matter presumably corresponds to an as-

---

<sup>1</sup>This chapter was extracted from [3], to which LFS contributed in the writing and analysis.

yet undiscovered elementary particle whose existence, along with couplings and other quantum properties, is yet to be confirmed and investigated. Dark energy is even more mysterious, as there are no compelling models aside, arguably, from the simplest one of vacuum energy.

Dark matter and dark energy leave numerous unambiguous imprints in the expansion rate of the universe and in the rate of growth of cosmic structures as a function of time. The theoretical modeling and direct measurements of these signatures have led to a renaissance in data-driven cosmology. Numerous ground- and space-based sky surveys have dramatically improved our census of dark matter and dark energy over the past two decades, and have led to a consensus model with 5% energy density in baryons, 25% in cold (nonrelativistic) dark matter (CDM), and 70% in dark energy. These probes, reviewed in [35, 108], include the cosmic microwave background, galaxy clustering including the location of the baryon acoustic oscillation (BAO) feature and the impact of redshift space distortions (RSD); distances to type Ia supernovae (SNe Ia); weak gravitational lensing, given by tiny distortions in the shapes of galaxies due to the deflection of light by intervening large-scale structure; and the abundance of clusters of galaxies.

The simplest and best-known model for dark energy is the cosmological constant. This model, represented by a single parameter given by the magnitude of the cosmological constant, is currently in good agreement with data. On the one hand, vacuum energy density is predicted to exist in quantum field theory due

to zero-point energy of quantum oscillators, and manifests itself as a cosmological constant: unchanging in time and spatially smooth. On the other hand, the theoretically expected vacuum energy density is tens of orders of magnitude larger than the observed value as has been known even prior to the discovery of the accelerating universe. Apart from the cosmological constant, there exists a rich set of other dark energy models including evolving scalar fields, modifications to general relativity, and other physically-motivated possibilities with many possible avenues to test them with data. Testing for such extensions of the simplest dark energy model on the present-day data has spawned an active research area in cosmology, and is the subject of this present section.

In 2017 the DES collaboration published the analyses of its first year of data (Y1). It presented results which put constraints on certain cosmological parameters derived from their late-universe imprints in galaxy surveys at the same level of precision as the constraints obtained on these same parameters from their early-universe signatures in the CMB data. These results, described in [2] (hereafter Y1KP) are based on the two-point statistics of galaxy clustering and weak gravitational lensing. The combined analysis of the three different two-point correlation functions (galaxy clustering, cosmic shear, and the galaxy-shear cross-correlation, typically referred to as galaxy-galaxy lensing) is the end product of a complex set of procedures which includes the analysis pipeline and methodology, its validation on realistic simulations, the creation of shape catalogs, the estimation and validation

of the redshift distribution for different galaxy samples, measurement and derivation of cosmological constraints from the cosmic shear signal, galaxy–galaxy lensing results and the galaxy clustering statistics. Both alone and in combination with external data.

In Y1KP we considered only the two simplest models for dark energy: the standard cosmological constant  $\Lambda$ CDM model and a  $w$ CDM model with an extra parameter (the dark energy equation-of-state  $w$ ) accounting for a constant relation between the pressure and the energy density of the dark energy fluid ( $p = w\rho$ ). In this paper we explore the impact of the DES Y1 data on the analysis of a few extensions of the standard flat  $\Lambda$ CDM and  $w$ CDM models considered in Y1KP, namely the possibilities of:

- Nonzero spatial curvature;
- New relativistic degrees of freedom;
- Time-variation of the dark energy equation-of-state;
- Modifications of the laws of gravity on cosmological scales.

We describe these extensions in more detail below. Our analysis applies the same validation tests with respect to assumptions about the systematic biases, analysis choices, and pipeline accuracy, as previously done in Y1KP. We also adopt the parameter-level blinding procedure used in that work, and we do not look at the final cosmological constraints until after unblinding, when the analysis procedure

and estimates of uncertainties on various measurement and astrophysical nuisance parameters were frozen. Validation and parameter blinding are also described in further detail below. Our study effectively complements and extends a number of studies of extensions to  $\Lambda/w$ CDM in the literature using state-of-the-art data, e.g. by Planck [75], the Baryon Oscillation Spectroscopic Survey (BOSS) [4], the Kilo Degree Survey (KiDS) [44,53] and more recently by using the Pantheon compilation of SNe Ia data [88]. These studies report no significant deviations from  $\Lambda$ CDM. We will comment on the comparison of our results to these existing constraints in the conclusion.

## 3.2 Extended Cosmologies

We assume the same set of  $\Lambda$ CDM cosmological parameters described in Y1KP, then supplement it with parameters alternately describing four extensions. We parametrize the matter energy density today relative to the critical density  $\Omega_m$ , as well as that of the baryons  $\Omega_b$  and of neutrinos  $\Omega_\nu h^2$ . Moreover, we adopt the amplitude  $A_s$  and the scalar index  $n_s$  of the primordial density perturbations power spectrum, as well as the optical depth to reionization  $\tau$ , and the value of the Hubble parameter today  $H_0$ . Except in the case of varying curvature, we assume that the universe is flat and, except in the case of varying dark energy, we assume that it is  $\Lambda$ -dominated with  $w = 1$ ; under those two assumptions,  $\Omega_\Lambda = 1 - \Omega_m$ . Note that the amplitude of mass fluctuations  $\sigma_8$  is a derived parameter, as is the parameter that

decorrelates  $\sigma_8$  and  $\Omega_m$ ,  $S_8 \equiv \sigma_8 \sqrt{\Omega_m/0.3}$ . The fiducial parameter set is therefore

$$\theta_{\text{base}} = \{\Omega_m, H_0, \Omega_b, A_s, n_s, (\tau)\} \quad (3.2.1)$$

where the parentheses around the optical depth parameter indicate that it is used only in the analysis combinations that use CMB data. In addition to this set of  $\Lambda$ CDM parameters, we use the following parametrization for each of the extension models:

- Spatial curvature:  $\Omega_k$ ;
- The effective number of neutrinos species  $N_{\text{eff}}$ ;
- Time-varying equation-of-state of dark energy:  $w_0$  &  $w_a$ ;
- Tests of gravity:  $\Sigma(a)$ ,  $\mu(a)$

The cosmological parameters describing these extensions, along with priors given to them in our analysis, are given in Figure 3.1.

### 3.2.1 Spatial Curvature

Standard slow-roll inflation predicts that spatial curvature is rapidly driven to zero. In this scenario, the amount of curvature expected today is  $\Omega_k \sim 10^{-4}$ , where the tiny deviation from zero is expected from horizon-scale perturbations but will be very challenging to measure even with future cosmological data. Departures from near-zero curvature are however expected in false-vacuum inflation. With

| $\Lambda$ CDM Extension     | Parameter        | Flat Prior      |
|-----------------------------|------------------|-----------------|
| Curvature                   | $\Omega_k$       | $[-0.25, 0.25]$ |
| Number relativistic species | $N_{\text{eff}}$ | $[3.0, 7.0]$    |
| Dynamical dark energy       | $w_0$            | $[-2.0, -0.33]$ |
|                             | $w_a$            | $[-3.0, 3.0]$   |
| Modified gravity            | $\Sigma_0$       | $[-3.0, 3.0]$   |
|                             | $\mu_0$          | $[-3.0, 3.0]$   |

Figure 3.1: The extended cosmological parameters introduced in our analysis, and their respective priors.

curvature, and ignoring the radiation density whose contribution is negligible in the late universe, the Hubble parameter initially shown in eq.(1.1.5) generalizes to

$$H(a) = H_0 \sqrt{\Omega_m a^{-3} + (1 - \Omega_\Lambda - \Omega_k) + \Omega_k a^{-2}} \quad (3.2.2)$$

so that  $\Omega_k < 0$  corresponds to spatially positive curvature, and the opposite sign to the spatially negative case. In this work, we compare constraints on  $\Omega_k$  using DES data alone, as well as with combinations of subsets of the external data described.

We do not modify the standard Halofit prescription for prediction of the nonlinear power spectrum for nonzero values of  $\Omega_k$ . Simulation measurements of the nonlinear spectrum for nonzero values of  $\Omega_k$  do not exist to sufficiently validate this regime. However, it is not an unreasonable a priori assumption that the nonlinear modification to the power spectrum is only weakly affected by curvature beyond the primary effect captured in the linear power spectrum being modified. We do

incorporate the impact of  $\Omega_k$  in the evolution of the expansion and growth, which is properly modeled as part of the linear matter power spectrum that is modified by Halofit. We verify that this approximation does not significantly impact our results by comparing to the case where we restrict our data to scales that are safely “linear” as described below.

### 3.2.2 Extra Relativistic Particle Species

Anisotropies in the CMB are sensitive to the number of relativistic particle species. The Standard Model of particle physics predicts that the three left-handed neutrinos were thermally produced in the early universe and their abundance can be determined from the measured abundance of photons in the cosmic microwave background. If the neutrinos decoupled completely from the electromagnetic plasma before electron-positron annihilation, then the abundance of the three neutrino species today would be

$$n = N_{\text{eff}} \times 113 \text{ cm}^{-3} \tag{3.2.3}$$

with  $N_{\text{eff}} = 3$ . In actuality, the neutrinos were slightly coupled during  $e^\pm$  annihilation, so  $N_{\text{eff}} = 3.046$  in the standard model. Values of  $N_{\text{eff}}$  larger than this would point to extra relativistic species. The DES observations are less sensitive to  $N_{\text{eff}}$  than the CMB, because the effect of this parameter in the DES mainly appears via the change in the epoch of matter-radiation equality. Nevertheless, DES might constrain some parameters that are degenerate with  $N_{\text{eff}}$  so, at least in principle,



adding DES observations to other data sets might provide tighter constraints.

In the fiducial model, we are allowing for a single free parameter  $\sum m_\nu$ , treating the 3 active neutrinos as degenerate (since they would be approximately degenerate if they had masses in the range we can probe,  $> 0.1$  eV). There is some freedom in how to parametrize the extension of a light sterile neutrino, however. If we attempt to model the addition of a single sterile neutrino, then in principle two new parameters must be added. For example, if the sterile neutrino has the same temperature as the active neutrinos, then the parameters can be chosen to be  $N_{\text{eff}}$ , allowed to vary between 3.046 and 4.046, and  $m_s$ , the mass of the sterile neutrino. Two light sterile neutrinos would require two more parameters, etc. However, we expect that the cosmological signal will be sensitive primarily to the total neutrino mass density and the number of effective massless species at the time of decoupling, as captured by  $N_{\text{eff}}$ , so we use only these two parameters,  $\sum m_n u$  and  $N_{\text{eff}}$ . Note that a value of  $N_{\text{eff}}$  appreciably different than 3 would point to a sterile neutrino or another light degree of freedom. We give  $N_{\text{eff}}$  a flat prior in the range [3.0, 9.0], where the lower hard bound encodes the guaranteed presence of at least three relativistic neutrino species.

### 3.2.3 Time-evolving Equation of State of Dark Energy

Given the lack of understanding of the physical mechanism behind the accelerating universe, it is important to investigate whether the data prefer models beyond the

simplest one, the cosmological constant. In Y1KP, we investigated the evidence for a constant equation-of-state parameter  $w = 1$ . We found no evidence for  $w \neq 1$ , with a very tight constraint from the combination of DES Y1, CMB, SNe Ia, and BAO of  $w = -1_{-0.04}^{+0.05}$ . We now investigate whether there is evidence for the time evolution of the equation-of-state  $w$ . We consider the phenomenological model that describes dynamical dark energy [63]

$$w(a) = w_0 + (1 - a)w_a \quad (3.2.4)$$

where  $w_0$  is the equation-of-state today, while  $w_a$  is its variation with scale factor  $a$ . The  $(w_0, w_a)$  parametrization fits many scalar fields and some modified gravity expansion histories up to a sufficiently high redshift, and has been used extensively in past constraints on dynamical dark energy. It is also useful to quote the value of the equation-of-state at the pivot  $w_p \equiv w(a_p)$ ; this is the scale factor at which the equation-of-state value and its variation with the scale factor are decorrelated, and where  $w(a)$  is best-determined. Rewriting eq. (3.2.4) as  $w(a) = w_p + (a_p - a)w_a$ , the pivot scale factor is

$$a_p = 1 + \frac{C_{w_0 w_a}}{C_{w_a w_a}} \quad (3.2.5)$$

where  $C$  is the parameter covariance matrix in the 2D  $(w_0, w_a)$  space, obtained by marginalizing the full  $28 \times 28$  covariance over the remaining 26 parameters. The corresponding pivot redshift is of course  $z_p = 1/a_p - 1$ .

The linear-theory observable quantities in this model are straightforwardly computed, as the new parameters affect the background evolution in a known way, given

that the Hubble parameter becomes

$$\frac{H(a)}{H_0} = [\Omega_m a^{-3} + (1 - \Omega_m) a^{-3(1+w_0+w_a)} e^{-3w_a(1-a)}]^{1/2}. \quad (3.2.6)$$

To obtain the nonlinear clustering in the  $(w_0, w_a)$  model, we assume the same linear-to-nonlinear mapping as in the  $\Lambda$ CDM model, except for the modified expansion rate  $H(z)$ . In particular, we implement the same Halofit nonlinear [99] prescription as we do in the fiducial  $\Lambda$ CDM case. We impose a hard prior  $w_0 + w_a \leq 0$ ; models lying in the forbidden region have a positive equation of state in the early universe, are typically ruled out by data, and would present additional challenges in numerical calculations. For the same reason we impose the prior  $w_0 < 0.33$ . Note also that in our analysis we do implicitly allow the “phantom” models where  $w(a) < -1$ ; while not a feature of the simplest physical models of dark energy (e.g. single-field quintessence), such a violation of the weak energy condition is in general allowed [19].

### 3.2.4 Modified Gravity

The possibility of deviations from general relativity on cosmological scales has been motivated by the prospect that an alternative theory of gravity could offer an explanation for the accelerated expansion of the Universe. In the past several years, numerous works constraining modifications to gravity using cosmological data have been published, including from the Planck team [22], the Kilo Degree Survey [53], and the Canada-France-Hawaii Lensing Survey [93]. Recently, stringent constraints

were made on certain alternative theories of gravity [64,81] via the simultaneous observation of gravitational and electromagnetic radiation from a binary neutron star merger with the Laser Interferometer Gravitational Wave Observatory (LIGO) [1]. In what follows, we refer to the scalar-perturbed Friedmann-Robertson-Walker line element in the conformal Newtonian gauge:

$$ds^2 = a^2(\tau) [(1 + 2\Psi)d\tau^2 - (1 - 2\Phi)\delta_{ij}dx^i dx^j] \quad (3.2.7)$$

In general relativity and without anisotropic stresses,  $\Psi = \Phi$ . The parametrization of deviations from general relativity studied in this work is motivated by theoretical descriptions which make use of the quasistatic approximation (see, e.g., [92]). It can be shown that in the regime where linear theory holds and where it is a good approximation to neglect time derivatives of novel degrees of freedom (e.g. extra scalar fields), the behavior of the majority of cosmologically-motivated theories of gravity can be summarized via a free function of time and scale multiplying the Poisson equation, and another which represents the ratio between the potentials  $\Phi$  and  $\Psi$ . Such a parametrization is an effective description of a more complicated set of field equations, but this approximation has been numerically verified on scales relevant to our present work.

There are a number of related pairs of functions of time and scale which can be used in a quasistatic parametrization of gravity; we choose the functions  $\mu$  and  $\Sigma$ ,

defined as

$$k^2\Psi = -4\pi G a^2 (1 + \mu(a)) \rho\delta \quad (3.2.8)$$

$$k^2(\Psi + \Phi) = -8\pi G a^2 (1 + \Sigma(a)) \rho\delta \quad (3.2.9)$$

where we are working in Fourier space where  $k$  is the wavenumber, and  $\delta$  is the comoving-gauge density perturbation. This version of the parametrization benefits from the fact that  $\Sigma$  parametrizes the change in the lensing response of massless particles to a given matter field, while  $\mu$  is linked to the change in the matter overdensity itself. Therefore, weak lensing measurements are primarily sensitive to  $\Sigma$  but also have some smaller degree of sensitivity to  $\mu$  via their tracing of the matter field, whereas galaxy clustering measurements depend only on  $\mu$  and are insensitive to  $\Sigma$ . We find the DES data alone are more sensitive to  $\Sigma$  than to  $\mu$ .

$$\mu(z) = \mu_0 \frac{\Omega_\Lambda(z)}{\Omega_\Lambda} \quad (3.2.10)$$

$$\Sigma(z) = \Sigma_0 \frac{\Omega_\Lambda(z)}{\Omega_\Lambda} \quad (3.2.11)$$

where  $\Omega_\Lambda(z)$  is the redshift-dependent dark energy density (in the  $\Lambda$ CDM model) relative to critical density, and  $\Omega_\Lambda$  is its value today. This time dependence has been introduced in [31], and is widely employed. It is motivated by the fact that in order for modifications to GR to offer an explanation for the accelerated expansion of the Universe, we would expect such modifications to become significant at the same timescale as the acceleration begins. We do not model any scale-dependence of  $\mu/\Sigma$  since it has been shown to be poorly constrained by current cosmological

data while not much improving the goodness-of-fit [75]. We therefore include only the parameters  $\mu_0/\Sigma_0$ . In GR,  $\mu_0 = \Sigma_0 = 0$ . Note that although our choice of parametrization is motivated by the quasistatic limit of particular theories of gravity, our analysis takes an approach which is completely divorced from any given theory. We endeavor instead to make empirical constraints on the parameters  $\mu_0/\Sigma_0$  as specified by the equations above.

### 3.3 Validation and Results

We subject our  $\Lambda$ CDM extensions analyses to the same battery of tests for the impact of systematics as in Y1KP. The principal goal is to ensure that all of our analyses are robust with respect to the effect of reasonable extensions to models of astrophysical systematics and approximations in our modeling. As part of the same battery of tests, we also test that the range of spatial scales that are used lead to unbiased cosmological results, and that motivated modifications to our modeling assumptions do not significantly change the inferred cosmology. In these tests and the results below, sampling of the posterior distribution of the parameter space is performed with Multinest [30] and emcee [33] wrappers within CosmoSIS10 [112] and CosmoLike [58]. While the convergence of Multinest is intrinsic to the sampler and achieved by verifying that the uncertainty in the Bayesian evidence is below than some desired tolerance, we explicitly check the convergence of emcee chains. In order to do so, we compute the autocorrelation length of each walk, then continue

the walks until a large number of such lengths is reached. The autocorrelation length estimates how long a chain needs to be in order for new “step” to be uncorrelated with previous ones. We then split chains into several uncorrelated segments and verify that marginalized parameter constraints do not change significantly when these segments are compared with each other. The typical number of samples of the posterior in these chains is between two and three million. We have also verified in select cases that this procedure leads to excellent agreement with the 1D marginalized parameter posteriors achieved by Multinest, so both samplers are used interchangeably in what follows.

In order to verify that our results are robust to modeling assumptions and approximations, we compare the inferred values of the extension parameters ( $\Omega_k$ ,  $N_{\text{eff}}$ , ...) obtained by a systematically shifted, noiseless synthetic data vector. The synthetic data vector is centered precisely on the standard  $\Lambda$ CDM cosmology, except it is shifted with the addition of a systematic effect that is not included in our analysis. The goal is to ensure that we do not claim evidence for an extension to  $\Lambda$ CDM when the real data contains astrophysical effects more complex than those in our model. For each systematic effect, we compare the inferred set of extension parameters to the fiducial, unmodified extension parameters used to create the synthetic data (which we refer to as the “baseline” constraint). For all of these tests, for DES we use the synthetic data vectors (for the baseline case and the systematic shifts described below), but for the external data sets — CMB, BAO, RSD, and SN Ia

— we use the actual, observed data vector. The changes to modeling assumptions that we consider are:

- Baryonic effects: we synthesize a noiseless data vector including a contribution to the nonlinear power spectrum caused by AGN feedback using the OWLS AGN hydrodynamical simulation [104] and following the methodology of [59].
- Intrinsic alignments, simple case: we synthesize a noiseless data vector with the IA amplitude  $A = 0.5$  and redshift scaling  $\eta = 0.5$  using the baseline nonlinear alignment model used in Y1KP. While we explicitly marginalize over these IA parameters in our analysis, this systematic check is still useful to monitor any potential biases due to degeneracy between the cosmological parameters and  $(A, \eta)$  and the presence of non-Gaussian posteriors
- Intrinsic alignments, complex case: we synthesize a noiseless data vector using a subset of the tidal alignment and tidal torquing model (hereafter TATT) from [15]. This introduces a tidal torquing term to the IA spectrum that is quadratic in the tidal field. The TATT amplitudes were set to  $A_1 = 0, A_2 = 2$  with no  $z$  dependence, as was done in [101] when validating the analysis of Y1KP.
- Nonlinear bias: we test our fiducial linear-bias assumption by synthesizing a noiseless data vector that models the density contrast of galaxies as

$$\delta_g = b_1 \delta + \frac{1}{2} b_2 [\delta^2 - \sigma^2] \quad (3.3.1)$$



where  $\delta$  and  $\delta_g$  are the overdensities in matter and galaxy counts respectively, and the density variance  $\sigma^2$  is subtracted to enforce that the mean of  $\delta$  is null. While this relationship is formally defined for smoothed density fields, the results do not depend on the choice of smoothing scale since, e.g., the variance explicitly cancels with contributions to the two-point correlation. We are considering scales that are sufficiently larger than the typical region of halo formation that we neglect higher-derivative bias terms.

- Magnification: we synthesize a noiseless data vector that includes the contribution from magnification to  $\gamma_t$  and  $w(\theta)$ . These are added in Fourier space using [7].
- Limber approximation and RSD: we synthesize a noiseless data vector that uses the exact (non-Limber)  $w(\theta)$  calculation and include the contribution from redshift space distortions.

The results of these tests are shown in Fig. 3.2. The columns show the parameters describing  $\Lambda$ CDM extensions, namely. The shaded vertical region shows the marginalized 68% posterior confidence limit (CL) in each parameter for the baseline case. The horizontal error bars show how this posterior, fully marginalized over all other parameters, including the other parameter in two-parameter extensions, changes with the systematic described in the given row for the case of DES-only (blue bars) and DES+external (red bars) data. We observe that, except in the

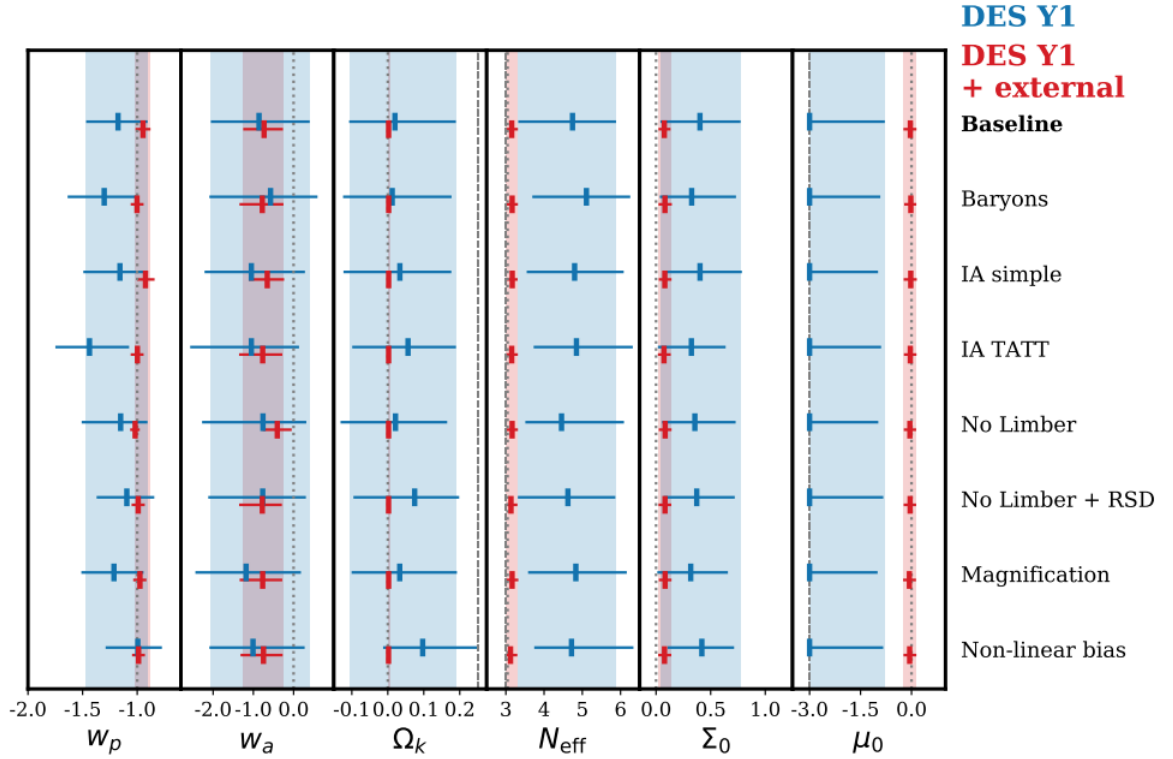


Figure 3.2: Impact of assumptions and approximations adopted in our analysis, demonstrated on synthetic data (that is, noiseless DES data centered on the theoretical expectation, along with actual external data). Each column shows one of the cosmological parameters describing  $\Lambda$ CDM extensions; the dotted vertical line is the true input value of that parameter in the DES data vector (which does not necessarily coincide with the parameter values preferred by the external data). The vertical shaded bands show the marginalized 68% CL constraints in the baseline model for the DES-only synthetic data (blue) and DES+external. The horizontal error bars show the inferred constraint for each individual addition to the synthetic data vector which are listed in rows; they match the shaded bands for the baseline case. Extracted from [3].

cases explained below, the marginalized posteriors are consistent with the baseline analysis in these tests.

Figure 3.2 shows shifts in some DES-only 68% C.L. constraints relative to the input value shown by the dotted vertical lines. The most pronounced effect is in the DES-only case for modified gravity parameter  $\mu_0$  (and, to a slightly smaller extent,  $\Sigma_0$  and  $N_{\text{eff}}$ ), which is more than  $1\sigma$  away from its true value of zero. Upon investigating this, we found that the bias away from the input value is caused by the interplay of two effects: 1) weak constraints, with a relatively flat likelihood profile in these parameters in certain directions, combined with 2) prior-volume effect, where the large full-parameter space volume allowed in the direction in which the parameter is a reasonably good fit ends up dominating the total integrated posterior, resulting in a 1D marginalized posterior that is skewed away from the maximum likelihood true value.

Since the baseline results agree with the contaminated cases, we proceed and show result from these parametrizations on real data. The constraints on curvature and the number of relativistic species are given in the two panels of Fig. 3.3.

Figure 3.3 indicates that DES alone constrains curvature weakly, showing mild ( $\sim 1\sigma$ ) preference for positive values of  $\Omega_k$ ; note also that this constraint is informed by the upper prior boundary. The DES-only constraint on  $N_{\text{eff}}$  is also relatively weak, and is fully consistent with the theoretically favored value  $N_{\text{eff}} = 3.046$ . Moreover, the DES Y1 data do not appreciably change the existing external-data

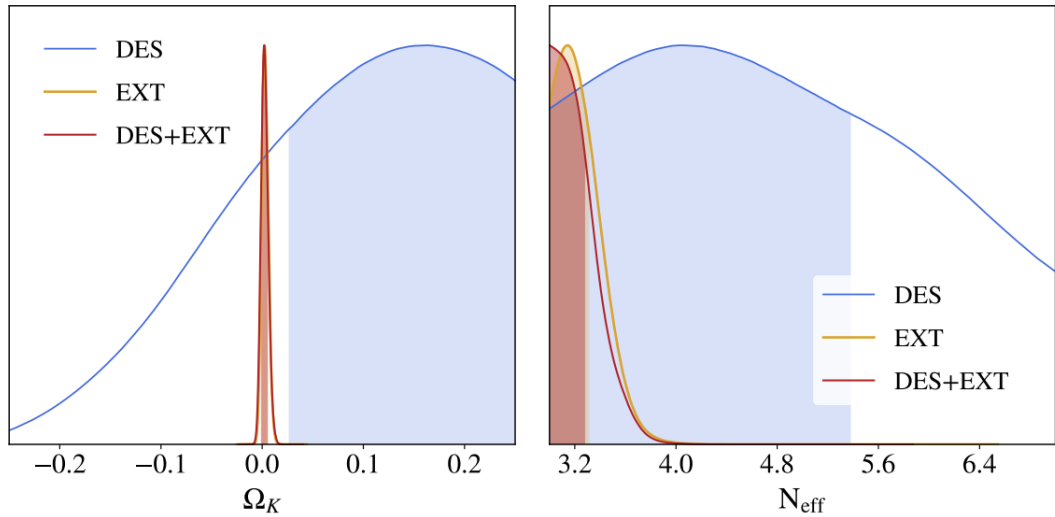


Figure 3.3: Posterior distributions on  $\Omega_k$  and  $N_{\text{eff}}$  from DES Y1. The constraining power of DES+external is mostly dominated by the tighter external posteriors.

constraints on these two parameters.

We now turn to dynamical dark energy and modified gravity constraints. The DES Y1 data alone are consistent with the cosmological-constant values of  $(w_0, w_a) = (-1, 0)$ ; they do not appreciably change the constraint from external data alone. The extended parameters on which the DES does add nontrivial information, however, are the modified gravity ones. Besides tightening constraints, DES also pushes  $\Sigma_0$  closer to its  $\Lambda$ CDM value of zero. An interesting manifestation of the multidimensionality of the parameter space is that the DES+external value is lower than either DES or external alone. This arises because DES favors a lower amplitude of mass fluctuations than that favored by the external data, due to the

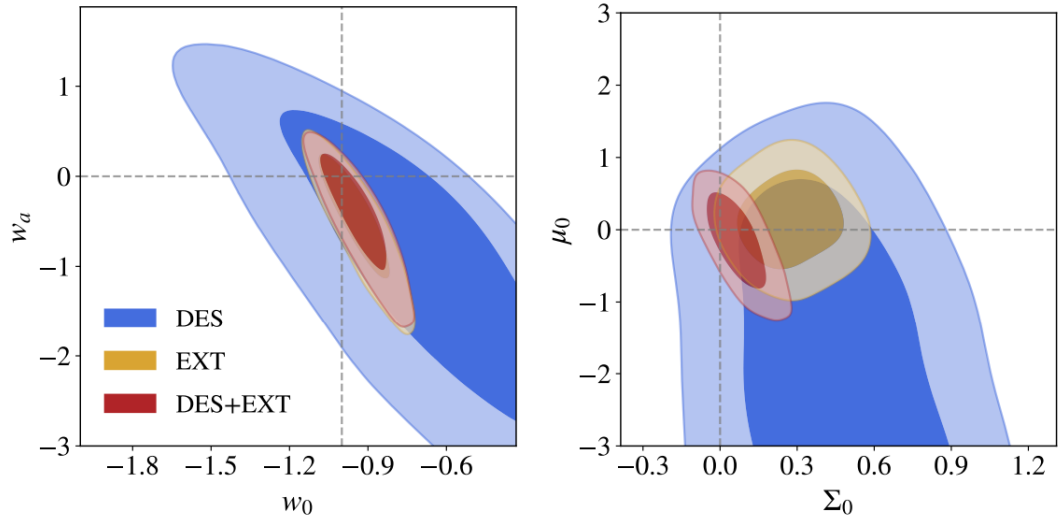


Figure 3.4: Constraints on dark energy parameters ( $w_0$ ,  $w_a$ ) (left panel) and the modified gravity parameters ( $\Sigma_0$ ,  $\mu_0$ ) (right panel). Blue contours show DES alone, yellow is external data alone, and red is the combination of the two. Dashed lines shows the parameter values in the  $\Lambda$ CDM model (left panel) and in GR (right).

lower amplitude of the lensing signal observed by the DES. Because the lensing amplitude is proportional to the product  $\Sigma_0 \times S_8$ , these two parameters are highly anticorrelated in DES, and the lensing amplitude suppression can be accommodated by decreasing either of them. Since external data constrain mostly  $S_8$  and constrain it to be high, the DES lensing amplitude is accommodated by shifting  $\Sigma_0$  down. These results are shown in Figure 3.4. We apply the Bayesian evidence ratio to all of the extended parameters above and find no preference for the addition of any of them to the standard  $\Lambda$ CDM model. The parameter constraints we find in DES-Y1 data are summarized in Figure 3.5.

Finally, in Figure 3.6, we show the constraints in the  $\Omega_m - S_8$  plane for the extended models (solid contours); for comparison, we also show the  $\Lambda$ CDM model constraints for DES data alone (dashed contours which are the same in all panels). The top right corner of each panel shows which extension the plot is referring to. For  $\Omega_k$ ,  $N_{\text{eff}}$  and  $w_0-w_a$  extensions, we see that the  $\Omega_m - S_8$  contour from DES alone is only modestly increased by marginalization over the additional nuisance parameter(s). The exception is the modified-gravity case, where the  $\Omega_m - S_8$  contour from DES alone is significantly larger and also pushed to smaller values of  $S_8$  because of the amplitude degeneracy between  $\Sigma_0$  and  $S_8$ .

| <b>Curvature</b>             | DES Y1                  | External                     | DES Y1 + External            | $[(\Delta\chi^2)_{\text{DES}}, (\Delta\chi^2)_{\text{Ext}}, (\Delta\chi^2)_{\text{DES+Ext}}]$ |
|------------------------------|-------------------------|------------------------------|------------------------------|---|
| $\Omega_k$                   | $0.16^{+0.09}_{-0.14}$  | $0.0023^{+0.0035}_{-0.0030}$ | $0.0020^{+0.0037}_{-0.0032}$ | $[-0.9, -0.2, -0.1]$  |
| <b>Number Rel. Species</b>   | DES Y1                  | External                     | DES Y1 + External            | $[(\Delta\chi^2)_{\text{DES}}, (\Delta\chi^2)_{\text{Ext}}, (\Delta\chi^2)_{\text{DES+Ext}}]$ |
| $N_{\text{eff}}$             | $< 5.38$                | $< 3.32$                     | $< 3.28$                     | $[0.2, 0.4, -0.7]$  |
| <b>Dynamical dark energy</b> | DES Y1                  | External                     | DES Y1 + External            | $[(\Delta\chi^2)_{\text{DES}}, (\Delta\chi^2)_{\text{Ext}}, (\Delta\chi^2)_{\text{DES+Ext}}]$ |
| $w_0$                        | $-0.69^{+0.30}_{-0.29}$ | $-0.96^{+0.10}_{-0.08}$      | $-0.95^{+0.09}_{-0.08}$      | $[-1.9, -0.0, -0.1]$  |
| $w_a$                        | $-0.57^{+0.93}_{-1.11}$ | $-0.31^{+0.38}_{-0.52}$      | $-0.28^{+0.37}_{-0.48}$      |   |
| $w_p$                        | $-0.91^{+0.19}_{-0.23}$ | $-1.02^{+0.04}_{-0.04}$      | $-1.01^{+0.04}_{-0.04}$      |   |
| <b>Modified Gravity</b>      | DES Y1                  | External                     | DES Y1 + External            | $[(\Delta\chi^2)_{\text{DES}}, (\Delta\chi^2)_{\text{Ext}}, (\Delta\chi^2)_{\text{DES+Ext}}]$ |
| $\Sigma_0$                   | $0.43^{+0.28}_{-0.29}$  | $0.26^{+0.14}_{-0.13}$       | $0.06^{+0.08}_{-0.07}$       | $[-0.2, -3.4, -0.4]$  |
| $\mu_0$                      | —                       | $0.16^{+0.43}_{-0.47}$       | $-0.11^{+0.42}_{-0.46}$      |   |

Figure 3.5: Constraints on the parameters describing the extensions of the  $\Lambda$ CDM model that we study in this paper. All errors are 68% confidence intervals, except for  $N_{\text{eff}}$  where we show the 68% upper bound. The last column shows the improvement in the goodness-of-fit,  $\Delta\chi^2$ , between the corresponding best-fit extension and the best-fit  $\Lambda$ CDM. Note that the sampling error in the  $\Delta\chi^2$  values is  $\sim 0.5$ ; hence, the two positive values in the last column (and many of the negative ones) should be treated as consistent with zero.

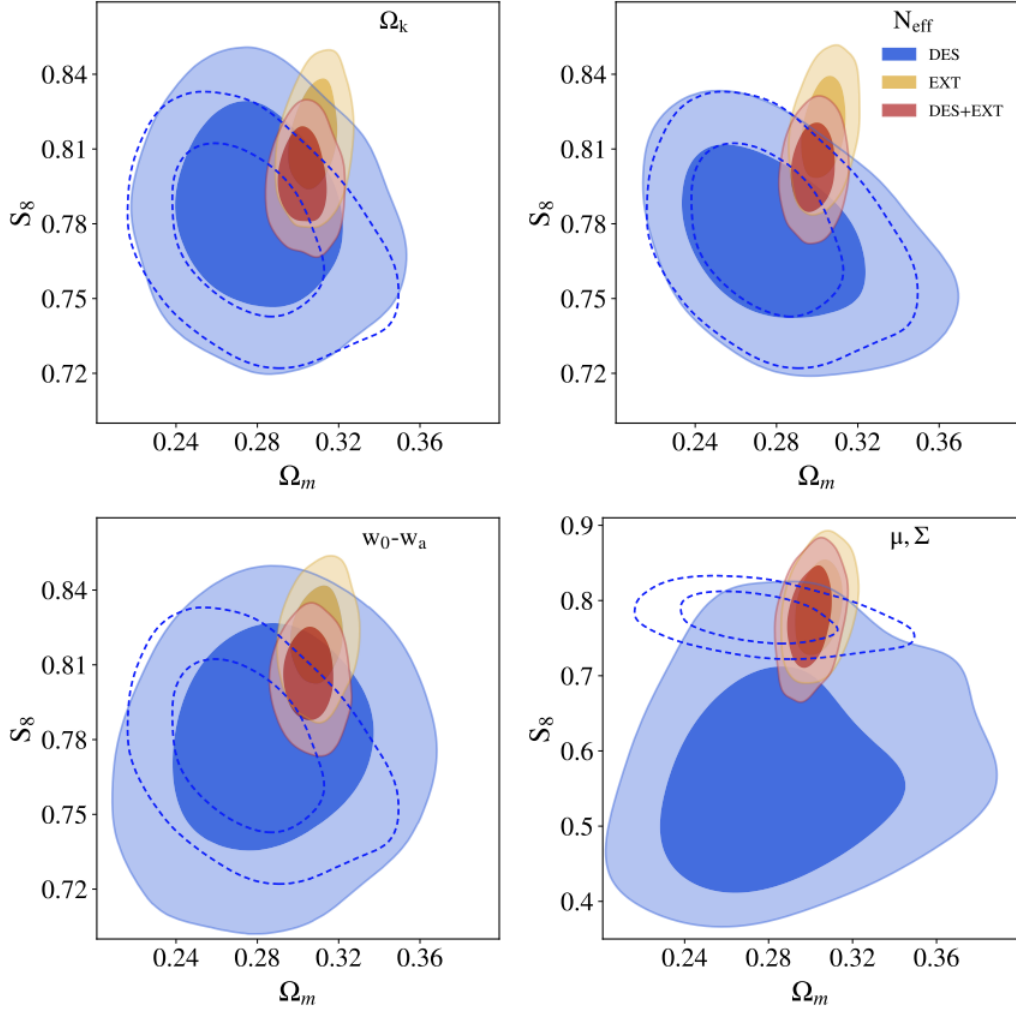


Figure 3.6: Comparison of constraints on the matter density  $\Omega_m$  and  $S_8$  to the  $\Lambda$ CDM case. The panels illustrate how the  $S_8 - \Omega_m$  constraints broaden and shift as we allow to vary: curvature (top left), number of relativistic species (top right), equation-of-state parameters  $w_0$  and  $w_a$  (bottom left), and modified gravity parameters  $\Sigma_0$  and  $\mu_0$  (bottom right). Shaded contours denote DES (blue), external (yellow), and DES+external (red) constraints. The DES-only  $\Lambda$ CDM case is shown in dashed contours, which are the same in each panel.



### 3.4 Conclusions

The results in this paper extend the work done in the Y1KP [2] by analyzing the models beyond flat  $\Lambda$ CDM and  $w$ CDM. In Y1KP, we found good agreement with the standard cosmological-constant dominated universe, and produced constraints on the matter density and amplitude of mass fluctuations comparable to those from the Planck satellite. We now extend that work into four new directions, allowing for: 1) nonzero curvature; 2) number of relativistic species different from the standard value of 3.046; 3) time-varying equation-of-state of dark energy described by the parameters; and 4) modified gravity parametrized by metric potentials. For the first three of these four extensions, we find that the DES Y1 data alone are consistent with values of zero curvature, three relativistic species, and dark energy parameters corresponding to the cosmological constant model. We also find that DES Y1 data do not significantly improve the existing constraints which combine the Planck 2015 temperature and polarization measurements, BAO measurements from SDSS and BOSS, RSD measurements from BOSS, and type Ia supernova measurements from the Pantheon compilation. When DES Y1 information is combined with that from the external data, the constraints on curvature are  $\Omega_k = 0.0020^{+0.0037}_{-0.0032}$ , while that on the dark-energy equation of state pivot value and its variation are  $w_p = -1.01^{+0.04}_{-0.04}$  and  $w_a = -0.28^{+0.37}_{-0.48}$ , respectively. The upper bound on the number of relativistic species is  $N_{\text{eff}} < 3.28$  (3.55) at the 68% (95%) confidence level from the combination of DES and external data.

DES Y1 alone provides a stronger constraint on the fourth extension of  $\Lambda$ CDM that we consider – modified gravity – giving  $\Sigma_0 = 0.43^{+0.28}_{-0.29}$ . The apparent DES-alone preference for positive  $\Sigma_0$  is consistent with parameter volume effects. When combining DES with external data, the  $\Sigma_0$  constraint is shifted downwards with respect to the external-only constraint, which can be explained by the fact that DES data prefer a lower lensing amplitude than that predicted by external data in  $\Lambda$ CDM. Combining DES Y1 with the external data gives  $\Sigma_0 = 0.06^{+0.08}_{-0.07}$  and  $\mu_0 = -0.11^{+0.42}_{-0.46}$  both of which are fully consistent with the  $\Lambda$ CDM values  $(\Sigma_0, \mu_0) = (0, 0)$ . The results in this work also serve to develop the tools necessary to take advantage of future constraints on these cosmological models by DES. In particular, the forthcoming analysis of the DES Y3 data, which will contain information from three times the area of Y1, should provide very interesting constraints on extensions of the minimal cosmological model including dark energy and modified gravity.

# Chapter 4

## Dark Matter in the Universe

We now turn our attention to the one of the main assumptions of the previous chapters: the hypothesis that Dark Matter (DM), apart from being cold, is deprived of any particle interactions. The presentation in the sections below was originally published in [89]<sup>1</sup>.

### 4.1 Introduction: Beyond the CDM Paradigm

The successful standard cosmological paradigm assumes that the dominant fraction of the matter contained in the universe is in the form of a nonluminous, nearly collisionless component called dark matter (DM). Furthermore, the clustering of matter in cosmological scales is often interpreted as evidence in favor of it being cold; i.e., it was nonrelativistic at the time of its decoupling from the thermal bath

---

<sup>1</sup>This article was led and written in its majority by LFS

of the primordial universe. However, the observed structure on small astrophysical scales has been claimed to be in tension with the CDM predictions derived from high-resolution simulations (e.g., [28, 71] for an incomplete list). There are several aspects to this possible tension. In particular, CDM-only simulations predict that (1) DM halo densities scale as  $\rho_{dm}(r) \propto r^{-1}$  in the inner  $\sim 1$  kpc of galaxies and (2) the number of satellite halos orbiting a Milky Way-sized halo is  $\mathcal{O}(100 - 1000)$ . The empirical facts that some halos seem to have flat cores ( $\rho_{dm} \propto r^0$ ) and that only  $\mathcal{O}(10)$  satellites have been found around our galaxy led these mismatches to be named the “core-cusp problem” and the “missing satellites problem,” respectively. Proper modeling and implementation of baryonic physics into simulations and the correction of observational biases have been claimed to alleviate such small-scale structure problems, though it is unclear whether they are fully resolved.

Spergel & Steinhardt (2000) [95] suggested that a nonzero cross section  $\tilde{\sigma}/m_{dm}$  for self-interacting dark matter (SIDM) could also help alleviate those problems. In the simplest model of SIDM,  $\tilde{\sigma}/m_{dm}$  is velocity-independent and large when compared to weak-force scales. Shortly after that initial work, stringent constraints were derived based on different observational predictions of SIDM, for instance, the sphericity (as opposed to triaxiality) of SIDM halos [68] and their evaporation rates [38]. With the growing sophistication of computational simulations, many of the previously obtained constraints have been significantly relaxed [23, 57, 74, 79]. In particular, simulations also showed that some level of velocity dependence of the

cross section is necessary to simultaneously explain the core sizes of dwarf galaxies and clusters.

Another potential observational consequence of DM self-interactions is an offset between light and mass centroids in cluster mergers. The dominant macroscopic effect of self-interactions in this case is expected to be analogous to that of a fluidlike drag force. The key idea is that, besides through gravitation, baryons are insensitive to SIDM, so stars act as a nearly collisionless component, while halos are decelerated by a drag force arising from the momentum transfer of DM interactions. The best-studied example of such a merger is the Bullet Cluster [21]). Constraints  $\tilde{\sigma}/m_{dm}$  have been derived on the basis that the separation between its matter centroid (as inferred from weak-lensing mass maps) and gas centroid (from X-ray emission) are of a few tens of kpc, consistent with zero within about the 68% confidence level. Based on the offsets within the Bullet Cluster, [65] found  $\tilde{\sigma}/m_{dm} < 5.0\text{cm}^2\text{g}^{-1}$ , while simulations by Randall et al. (2008) [76] found  $\tilde{\sigma}/m_{dm} < 1.25\text{cm}^2\text{g}^{-1}$ .

Under SIDM, halos are also subject to evaporation. The upper bounds derived from the survival of the cluster despite halo evaporation are slightly more stringent:  $\tilde{\sigma}/m_{dm} < 1.0\text{cm}^2\text{g}^{-1}$  from [65] and  $\tilde{\sigma}/m_{dm} < 0.7\text{cm}^2\text{g}^{-1}$  [76]. Roughly consistent constraints were obtained from studies of offsets within the Abell 3827 cluster [55] and from cluster collision images from HST and Chandra [40]. Interestingly, the offsets between member galaxies and DM measured in those cluster mergers seem to be consistent with standard CDM when systematic effects of projection and

mischaracterization of the centroids are significant. The differing constraints from evaporation and centroid offsets arise from the different assumptions on the microscopic behavior of DM interactions. It is commonly asserted that the desired range of cross sections necessary to explain the observed mass profiles of galaxies is around  $\tilde{\sigma}/m_{dm} \sim 0.5 - 5.0 \text{cm}^2 \text{g}^{-1}$  ([103] and references therein), with the upper bound being already severely constrained. It is thus notable that the simplest SIDM models have not been unambiguously ruled out to date.

In this context, galaxy clusters provide especially interesting environmental conditions for the study of DM interactions. If a flat core is present, the DM densities at the inner regions of  $\mathcal{O}(10^{14} - 10^{15})M_{\odot}$  cluster halos can reach around  $10^{-2}M_{\odot}\text{pc}^{-3}$ , or even as dense as  $10^0 M_{\odot}\text{pc}^{-3}$  in analytical cuspy profiles, while fairly concentrated galactic halos reach around  $10^{-1} M_{\odot}\text{pc}^{-3}$  in the inner 1 kpc.

These densities enhance the number of interactions between DM particles, leading to potentially observable effects resulting from any additional drag force acting on DM. In this work, we consider a disk galaxy in its galactic halo (hereafter subhalo) falling into a galaxy cluster (hereafter the main, host halo). While offsets between the luminous components of cluster mergers and their total matter centroids have been measured, the analogous measurement for a galactic halo would likely be highly dominated by noise, since the weak-lensing signal of a single such halo is not accurate enough to determine its centroid. However, we show that indirect effects on disk-galaxy morphologies resulting from relatively small baryon-DM

displacements could be potentially measurable.

In this work, we employ numerical simulations to characterize two types of distortions caused on stellar disks in SIDM subhalos when an effective drag is the dominating factor. The first distortion is the warping of the galaxy disk: a U-shaped bending along the direction of motion. A second, longer-lasting effect is the enhanced thickening of the disk once the warp mode decays. These U-shaped warps are not common in standard CDM; tidal interactions and kinematic processes usually lead to S-shaped distortions, and  $H_I$  disks are known to exhibit prominent S-shaped warps [9]. For example, in a study of 26 edge-on disk galaxies by [36], 21  $H_I$  warps were found, only two of which were U-shaped. However, these two were both highly disturbed and strongly interacting with visible nearby companions. In what follows, we show that DM self-interactions may lead to a U-shaped warp that is not necessarily caused by close encounters with neighboring galaxies.

## 4.2 Analytic and Numerical Models for Galaxy Warps

### 4.2.1 SIDM as a Drag Force

For colliding DM halos, the microscopic nature of the interactions between the DM particles determines the dominant macroscopic signatures that will be observable in such systems. The two main macroscopic effects that have been considered in

the literature are the evaporation rate of the smaller halo and an effective drag that each halo experiences as it moves through the environment of the other halo. For short-range interactions with isotropic cross sections, immediate halo evaporation is the most dominant effect [54, 65]. As a large fraction of collisions have a high momentum transfer, particles may be expelled from their host’s potential, leading to subhalo evaporation. The observation of surviving low-mass subhalos therefore puts a stringent upper bound on the cross section of isotropic scattering, as well as the fraction of collisions that result directly in the expulsion of DM particles from the subhalo. On the other hand, if we consider interactions where the cross section is velocity-independent and anisotropic - that is, there are many more small-angle scatterings than there are large-angle scatterings - frequent interactions are possible without completely disrupting the subhalo. In this scenario, individual interactions are usually unable to expel particles from the subhalo. However, there is a nonzero cumulative evaporation rate resulting from multiple interactions. As shown in [54], frequent and anisotropic self interactions also lead to an effective “drag” force, and the rate of deceleration due to the drag force is comparable to the rate of cumulative evaporation. For these interactions, therefore, the macroscopic effects of the drag force can be comparable to the effects coming from evaporation [61].

To understand the origin of the drag, we consider a two-particle interaction in the center of mass (COM) frame. If the scattering angle in this frame is  $\theta$ , then in the direction parallel to the relative velocity of the two particles, the change in the



velocity of one particle is given by

$$\delta v_{\parallel} = -v(1 - \cos \theta), \quad (4.2.1)$$

where  $v$  is the initial velocity of the particle in the COM frame. For isotropic interactions,  $\cos \theta$  is drawn from a uniform distribution between  $-1$  and  $1$ . For anisotropic interactions of the form that we are interested in,  $\cos \theta$  is drawn from a distribution that is peaked near  $1$  and  $-1$ , and has very low probability for collisions where  $\cos \theta \sim 0$ . In particular, we use the same form of the differential cross section for the anisotropic interactions as was used in [54]:

$$\frac{d\sigma}{d\Omega} \propto \frac{1 + \cos^2 \theta}{1 - \cos^2 \theta}. \quad (4.2.2)$$

If collisions are frequent, and if individual interactions only change the initial velocity by a small amount, we can integrate over all possible interaction angles to obtain the average change in the velocity in the parallel direction of a particle passing through a sea of other particles. In a time interval  $dt$ , the number of interactions is given by

$$dN = \frac{\rho}{m_{\text{dm}}} (v dt) \frac{d\sigma}{d\Omega} d\Omega, \quad (4.2.3)$$

where  $d\sigma/d\Omega$  is the differential cross section,  $\rho$  is the ambient density, and  $m_{\text{dm}}$  is the mass of the dark matter particle. Using this, we can write the total change in the parallel velocity as

$$dv_{\parallel} = -\frac{\rho v^2 dt}{m_{\text{dm}}} \int \frac{d\sigma}{d\Omega} (1 - \cos \theta) d\Omega. \quad (4.2.4)$$

Since we assume that the dark matter particles are indistinguishable, we follow [54], and define the momentum transfer cross section  $\sigma_T$  as

$$\sigma_T = 4\pi \int_0^1 \frac{d\sigma}{d\Omega} (1 - \cos\theta) d(\cos\theta). \quad (4.2.5)$$

Once again, this expression makes sense only when the overall direction and velocity change per particle in the time interval  $dt$  is small compared to the incoming velocity. For our choice of the differential cross section, this is a safe approximation to make for sufficiently small time steps. The integral runs over the scattering angle  $0 \leq \theta \leq \pi/2$  since, for indistinguishable particles, a scattering angle above  $\pi/2$  is the same as an equivalent scattering angle below  $\pi/2$  but with a relabeling of the two outgoing particles. Using the expression for  $\sigma_T$ , equation (4.2.4) reduces to

$$dv_{\parallel} = -\frac{\rho v^2 dt}{2m_{\text{dm}}} \sigma_T \quad (4.2.6)$$

Therefore, this change in the parallel velocity can be written as an effective drag deceleration due to the anisotropic self-interactions as a particle moves through a sea of other dark matter particles, with

$$\frac{F_{\text{drag}}}{m_{\text{dm}}} = -\frac{1}{2} \left( \frac{\sigma_T}{m_{\text{dm}}} \right) \rho v^2. \quad (4.2.7)$$

We note that for isotropic cross sections where  $d\sigma/d\Omega$  is a constant, the momentum transfer cross section  $\sigma_T$  and the total cross section  $\tilde{\sigma}$  is given by  $\tilde{\sigma} = 2\sigma_T$ . Therefore, we can re-cast equation (4.2.7) in terms of  $\tilde{\sigma}$  so that our results can be compared directly to results for isotropic self-interactions. This yields

$$\frac{F_{\text{drag}}}{m_{\text{dm}}} = -\frac{1}{4} \left( \frac{\tilde{\sigma}}{m_{\text{dm}}} \right) \rho v^2. \quad (4.2.8)$$

We note that we assumed that the relative velocity between the two colliding halos, or the velocity of a subhalo falling into the host halo, is much larger than the velocity dispersion of the subhalo, and therefore the self-interactions between the subhalo and the particles of the host halo dominate over self-interactions between particles of the subhalo itself.

### 4.2.2 The Cluster and Subhalo System

We now describe the astrophysical system which is the focus of this study. Consider a spherically symmetric galactic subhalo which contains a disk galaxy seen edge-on by the observer. The centers of mass of both the subhalo and the disk initially coincide. The whole system moves along a trajectory  $r_{\text{sh}}$  with velocity  $v_{\text{sh}}$  through a host dark matter halo of density  $\rho_{\text{h}}$  (a galaxy cluster), assumed to be at rest. For typical orbital velocities and halo densities, equation (4.2.8) leads to a non-negligible contribution of SIDM to the motion of the subhalo, decreasing its infall acceleration and consequently distorting the galaxy disk. We present a schematic description of the system in Figure 4.1.

To simplify our treatment of this problem, we make several approximations

1. The galaxy disk is made of stars only, and they are perfectly collisionless. We assume that the gravitational effect of the gaseous component of the disk is irrelevant to the dynamics.
2. The galaxy disk experiences the gravitational attraction towards the dark

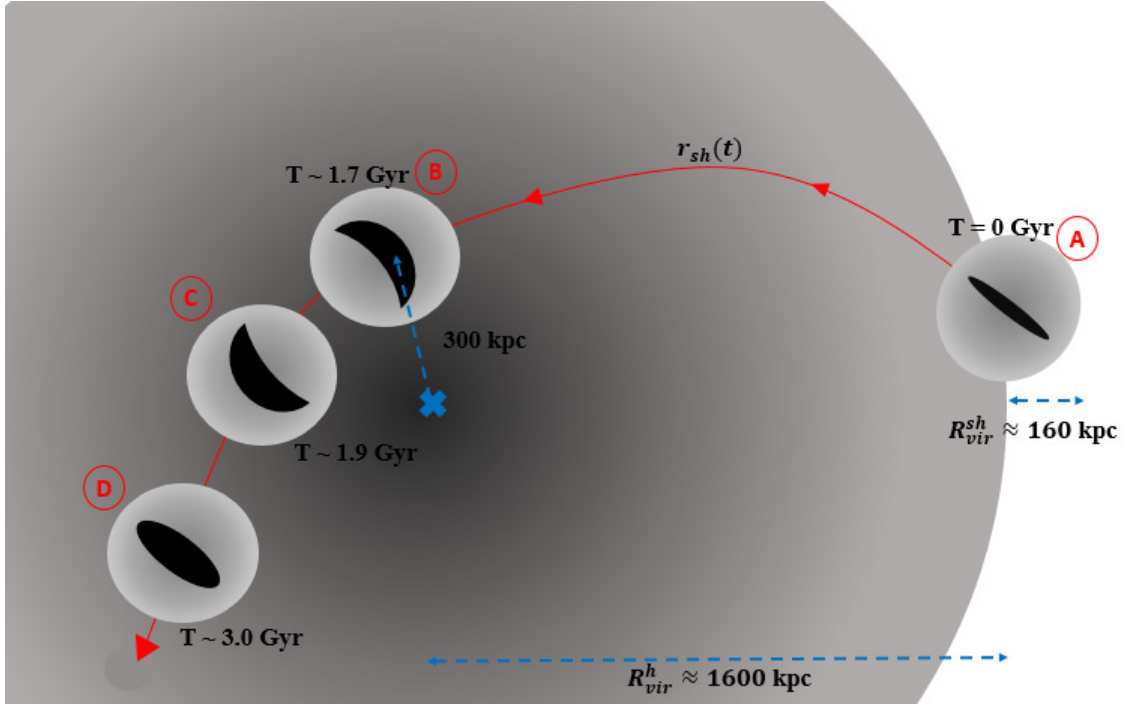


Figure 4.1: A schematic view of the simulated system (not to scale). With the fiducial choices detailed in Section 4.2.2, the virial radius of the host is around  $R_{\text{vir}}^h = 1600$  kpc and that of the subhalo is around  $R_{\text{vir}}^{\text{sh}} = 160$  kpc. The curved red line corresponds to the trajectory of the subhalo through the host,  $r_{\text{sh}}(t)$ . At (A), the thin galaxy disk is at the center of the subhalo at time  $T = 0$  Gy. At (B), at around  $T = 1.7$  Gy (exact time values are slightly dependent on the chosen pericenter) the system is at closest approach from the host center and, shortly after that, the galaxy is maximally warped. At (C), typically 200My after the initial forward warp, the distortion oscillates backwards. At much later times, (D), around  $T = 3$  Gy, the subhalo is close to its second turnaround or “splashback radius”, and the disk is thicker than it was at the start.

matter subhalo in which it is contained, but the subhalo does not experience any attraction towards the stars. While this approximation is used for most of the simulations in this work, we do test its validity in Section 4.3.4.

3. The dark matter subhalo is spherical and is not distorted while crossing the host. It is characterized by a static radial density profile, so we treat its trajectory semi-analytically. The same applies to the host halo. This approximation implies that any possible disruption of either halos during the merger or evaporation of the subhalo has a small effect on the stellar disk; the effective drag force is dominant.

With these approximations, plus equation (4.2.8), the acceleration of the subhalo center of mass and of a given star can be written as:

$$\ddot{\mathbf{r}}_{\text{sh}} = -G \frac{M_{\text{h}}(< |\mathbf{r}_{\text{sh}}|)}{|\mathbf{r}_{\text{sh}}|^3} \mathbf{r}_{\text{sh}} + \frac{1}{4} \left( \frac{\tilde{\sigma}}{m_{\text{dm}}} \right) \rho_{\text{h}} \dot{\mathbf{r}}_{\text{sh}}^2 \quad (4.2.9)$$

$$\begin{aligned} \ddot{\mathbf{r}}_{\star}^i &= -G \frac{M_{\text{h}}(< |\mathbf{r}_{\star}^i|)}{|\mathbf{r}_{\star}^i|^3} \mathbf{r}_{\star}^i - G m_{\star} \sum_{i \neq j} \frac{(\mathbf{r}_{\star}^i - \mathbf{r}_{\star}^j)}{|\mathbf{r}_{\star}^i - \mathbf{r}_{\star}^j|^3} \\ &\quad - G \frac{M_{\text{sh}}(< |\mathbf{r}_{\star}^i - \mathbf{r}_{\text{sh}}|)}{|\mathbf{r}_{\star}^i - \mathbf{r}_{\text{sh}}|^3} (\mathbf{r}_{\star}^i - \mathbf{r}_{\text{sh}}), \end{aligned} \quad (4.2.10)$$

where  $\mathbf{r}_{\star}^i$  is the 3D position of  $i$ -th star relative to the center of the host,  $M_{\text{h}(\text{sh})}$  is the mass of the host (subhalo) enclosed in a given radius and  $m_{\star}$  is the mass of a single star.

This system of equations is similar to that employed by [55], to which we add the mutual gravitational attraction between stars by introducing the summation

Figure 4.2: Radial density profiles of the subhalo (black) and the host halo (red). The host has a Hernquist profile defined by equation (4.2.11), with virial mass  $M_h = 10^{15} M_\odot$  and concentration  $c = 5$ . The subhalo is also a Hernquist profile with virial mass  $M_{sh} = 10^{12} M_\odot$  and concentration  $c = 8$ .

term of equation (4.2.10). In particular, disregarding that self-gravity term, direct numerical integration of equations (4.2.9) and (4.2.10) has been used by those authors for an approximate description of the offset created between a collisionless component and its subhalo's center.

Our choices for the halo profiles are shown in Figure 4.2. For both the subhalo and host, we use a Hernquist profile [41] given by

$$\rho(r) = \frac{M_{\text{dm}}}{2\pi} \frac{a}{r(r+a)^3} \quad (4.2.11)$$

where  $a$  is the scale factor and  $M_{\text{dm}}$  is the total mass of the halo. Following [97], we determine  $a$  for each halo by matching their inner densities to an NFW profile [70] with concentration  $c$  and virial radius  $r_{200}$  using

$$a = \frac{r_{200}}{c} \sqrt{2 [\ln(1+c) - c/(1+c)]}. \quad (4.2.12)$$

In our fiducial analysis, the host has halo mass of  $10^{15} M_\odot$  and concentration  $c = 5$ , while the subhalo has mass  $10^{12} M_\odot$  and  $c = 8$ .

The disk galaxy contained in the subhalo has an exponentially decaying radial

profile and a squared hyperbolic secant vertical profile:

$$\rho_{\text{disk}}(R, z) = \frac{M_{\text{disk}}}{4\pi z_0 h_0^2} \exp\left(-\frac{R}{h_0}\right) \text{sech}^2\left(\frac{z}{z_0}\right) \quad (4.2.13)$$

where  $h_0$  is the scale length of the disk,  $z_0$  its scale height and  $M_{\text{disk}}$  its stellar mass. We choose  $M_{\text{disk}} = 3 \times 10^{10} M_{\odot}$ ,  $h_0 \approx 3.5$  kpc and a ratio of scale height to scale length of  $z_0/h_0 = 0.1$  for the fiducial simulated galaxy disk. We also relate the velocity dispersions of the galaxy in the radial and vertical directions such that  $\sigma_z = 0.5\sigma_R$ , and set  $\sigma_{\phi} = \sigma_R$  for the azimuthal direction  $\hat{\phi}$ . With these choices, the resulting disk is roughly compatible with a Milky-Way type galaxy [11]. The resulting galaxy is stable and its Toomre Q parameter is greater than 1 at all relevant radii [100].

### 4.2.3 Numerical Simulation

To set up initial conditions for the phase space distribution of a galaxy disk, we use the publicly available code GalIC<sup>2</sup> [111]. GalIC iteratively minimizes a set of merit functions which measure the discrepancy between the target and realized spatial density field and velocity dispersions. It achieves this by using a Monte Carlo style algorithm that forces the velocity distributions to have the correct second order moments. We use  $N = 10^5$  particles to populate the stellar disk, and set the remaining parameters of GalIC to reproduce our fiducial scenario. The generated fiducial disk is close enough to an equilibrium state that it maintains its profile for

---

<sup>2</sup><https://www.h-its.org/tap-software-en/galic-code/>

a sufficiently long time.

To evolve the motion of the subhalo-disk system in time, we need to efficiently solve equations (4.2.9) and (4.2.10). We use the publicly available code GIZMO<sup>3</sup> [47] in order to do so. GIZMO inherits some of its N-body algorithms from GADGET-2<sup>4</sup> [96] and GADGET-3, and solves gravity with an efficient tree method. It also allows for the use of external analytic gravitational potentials and forces, and we use that feature to reproduce the motion of the subhalo through the host. Both halos are introduced as analytic potentials and are not populated with particles, and the subhalo moves according to a prescribed trajectory while the host is fixed. We first integrate equation (4.2.9) with the relevant set of initial conditions and a choice of  $\tilde{\sigma}/m_{\text{dm}}$  ( $0.5 \text{ cm}^2\text{g}^{-1}$ ,  $1.0 \text{ cm}^2\text{g}^{-1}$  or CDM), then feed to GIZMO a look-up table with this subhalo trajectory  $r_{\text{sh}}(t)$ .

As depicted in Figure 4.1, the subhalo-plus-disk system starts its infall at the virial radius of the host, roughly 1600 kpc away from its center. To simulate realistic cases, we use subhalo orbits with several choices of pericenters, defined as the closest approach distances from the center of the host. We set the pericenter by initially giving the subhalo-disk system a tangential velocity whose magnitude is a fraction of the circular velocity about the host. While we experimented with different values, we focus on pericenter distances of 200 and 300 kpc for our analysis, since these show appreciable SIDM effects and are not dominated by tidal distortions due to

---

<sup>3</sup><http://www.tapir.caltech.edu/~phopkins/Site/GIZMO.html>

<sup>4</sup><http://wwwmpa.mpa-garching.mpg.de/gadget/>



the host which could break our initial assumptions. The ratio of mean pericenter to cluster virial radius (apocenter) is about 1:6 as shown in simulations by [37]. We note that a more recent study by [105] has found a mean pericenter that is larger by a factor of around two with respect to [37]. Our choices thus reflect a sizable fraction of orbits of subhalos inside clusters.

We also expect the orientation of the galaxy disk at its closest passage to the host to change the observable morphological distortions. This orientation is defined as the angle between the center of mass velocity of the galaxy disk and the normal to its plane. We study 4 different scenarios: orientation angles of 0, 22.5, 45 and 67.5 degrees (0 degrees is a face-on passing through the host and 90 degrees would be a passing along the diameter of the disk, which is not interesting for our analysis). Note that in all of these cases, the galaxy is still edge-on for the observer. In our simulations, each disk is evolved separately, so no simultaneous interaction with other galaxies is present.

#### 4.2.4 An Analytical Prediction of the Results

Consider a single star of mass  $m_*$  in a nearly circular orbit around the disk center. To determine the disk warping, we are interested in the star's motion in the direction perpendicular to the galaxy plane,  $z(t)$ . Under the approximation that the drag force is constant across the entire subhalo, and considering that the warp is small enough such that the disk potential is not severely disturbed, we can describe the

motion of a star *in the reference frame of the subhalo* as

$$\ddot{z} = \left( \frac{F_{\text{drag}}}{m_{\text{dm}}} \right) - \frac{F_{\text{sh}} \sin \theta}{m_{\star}} - \frac{\partial \Phi_{\text{eff}}(R, z)}{\partial z} \quad (4.2.14)$$

where the first term is given by equation (4.2.8) and comes from the change in reference frames, and the effective potential of the axisymmetric stellar disk is  $\Phi_{\text{eff}}(R, z) = \Phi(R, z) + L_z^2/2R^2$ , where  $R$  is the radial distance from the star to the center of the disk along its plane, and  $L_z$  its conserved angular momentum. The term  $F_{\text{sh}} \sin \theta$  is the projection of the subhalo gravity onto the direction perpendicular to the plane of the galaxy, with  $\theta$  being the angle between the galaxy plane and the vector that goes from the galaxy center to the displaced star. One could also add to equation (4.2.14) a term that corresponds to the tidal force caused by the host, but that component is at least an order of magnitude weaker than the gravity of the subhalo at the scale radius of the disk.

Recalling the approximation that a star does not wander too far from the plane of the disk, we have  $\sin \theta \approx z/R$ . Using the spherical symmetry of the subhalo and the epicycle approximation [12] to Taylor expand the potential up to second order in  $z$ -derivatives, we can write

$$\ddot{z} = \frac{1}{4} \left( \frac{\tilde{\sigma}}{m_{\text{dm}}} \right) \rho_{\text{h}} v_{\text{sh}}^2 - \frac{GM_{\text{sh}}(R)}{R^2} \left( \frac{z}{R} \right) - \frac{\partial^2 \Phi}{\partial z^2} z, \quad (4.2.15)$$

where the second derivative of the potential is evaluated at the equilibrium position  $z = 0$ , on the plane of the galaxy. Describing the subhalo by a Hernquist profile,

the cumulative mass within the radius  $R$  is given by [41]

$$M_{\text{sh}}(R) = M_{\text{dm}} \frac{R^2}{(R+a)^2}, \quad (4.2.16)$$

where  $a$  is the scale radius of the halo, equivalent to that of equation (4.2.11). To treat the potential, we use a fully analytic expression that approximates the 3D potential of an axisymmetric disk with characteristic radius  $h_0$  and characteristic height  $z_0$ , given by [69]:

$$\Phi(R, z) = - \frac{GM_{\text{disk}}}{\left[ R^2 + \left( h_0 + \sqrt{z^2 + z_0^2} \right)^2 \right]^{1/2}}. \quad (4.2.17)$$

A final approximation is that most of the warp occurs in a relatively short time span, becoming maximal near the pericenter of the subhalo trajectory by the host. We verify with the simulations that this is especially true for the mild warps with which we are concerned in this derivation. With that in mind, the drag force acts as a “kick” on the star under consideration. Using equations (4.2.16) and (4.2.17) on equation (4.2.15) and keeping the dominant orders in  $R$ , the motion of a point on the disk is described by

$$\ddot{z}(t = t_{\text{imp}}) = \left[ \frac{1}{4} \left( \frac{\tilde{\sigma}}{m_{\text{dm}}} \right) \rho_{\text{h}} v_{\text{sh}}^2 \right]_{t=t_{\text{imp}}} - \omega^2 z \quad (4.2.18)$$

where  $t_{\text{imp}}$  is the time at which the subhalo is at pericenter, and where

$$\omega^2 = \frac{GM_{\text{dm}}}{R(R+a)^2} + \frac{\left( 1 + \frac{h_0}{z_0} \right) R^2}{[(h_0 + z_0)^2 + R^2]^{5/2}} GM_{\text{disk}}. \quad (4.2.19)$$

such that the system resembles a driven harmonic oscillator with characteristic frequency  $\omega$ .

Equation (4.2.18) suggests two things: that the gravitational pull of the subhalo and disk act together as a restoring force, opposing the warp, and that this distortion is oscillatory. Especially at larger  $R$ , the squared frequency given by equation (4.2.19) goes as  $R^{-3}$ , so the restoring force is smaller at large radii and particles closer to the disk edge are less tightly bound gravitationally. The galaxy disk thus gets warped due to *differential offsets* along the disk, its longitudinal section becoming “U-shaped”, and the warp shape may oscillate around the initially thin configuration. Note that the edge-on disk initially bends *forward* towards the direction of motion of the galaxy, as depicted on Figure 4.1. We indeed find the warping effect in the simulations described in the following sections, not only for the mildly warped disks but also for the intense warps which perturb the galaxy potential beyond our analytic approximations.

We can use equation (4.2.18) to obtain a theoretical estimate of the maximum amplitude of the warp. Consider the fact that very shortly after the drag-induced “kick”, the galaxy reaches its new, distorted equilibrium position, and that the kick takes a finite, but small, amount of time. In that case, we can find the equilibrium displacement  $z$  by setting  $\ddot{z} = 0$  on equation (4.2.18). The maximal displacement obtained this way is:

$$z_{\max}(R) = \frac{\rho_{\text{h}} v_{\text{sh}}^2}{4\omega^2} \left( \frac{\tilde{\sigma}}{m_{\text{dm}}} \right), \quad (4.2.20)$$

with  $\omega^2$  given by equation (4.2.19). Using physical parameters similar to our fiducial system on equation (4.2.20) for the disk and subhalo dimensions and mass, we

|         | $R = h_0$ | $R = 2h_0$ | $R = 3h_0$ |
|---------|-----------|------------|------------|
| 200 kpc | 0.48      | 1.05       | 2.39       |
| 300 kpc | 0.19      | 0.42       | 0.95       |

Table 4.1: Analytic prediction of the magnitude of the displacement  $z_{\max}$  as a function of disk radius, in units of kpc, for the fiducial galaxy scenario when  $\tilde{\sigma}/m_{\text{dm}} = 1.0 \text{ cm}^2\text{g}^{-1}$ . These results match the simulations with reasonable accuracy.

estimate the magnitude of the distortions in units of kpc on Table 1 for the pericenters of interest. More explicitly, we use  $h_0 = 3.5 \text{ kpc}$ ,  $z_0 = 0.1 h_0$ ,  $M_{\text{dm}} = 10^{12} M_{\odot}$ ,  $M_{\text{disk}} = 3 \times 10^{10} M_{\odot}$  and  $a = 30 \text{ kpc}$ . We use the local dark matter density of the host at pericenter, and the subhalo velocity is around  $3200 \text{ km/s}$ .

While equation (4.2.20) itself suggests a way of fitting the shape of the distortion, we choose a slightly different method in Section 4.3.1, which accounts also for asymmetric warps. An added effect, not accounted for in the previous derivation, is an ‘‘S-shaped’’ warp resembling an integral sign. The presence of an S-shaped warp is a standard dynamical feature that arises quite generally from tidal interactions with close neighbors [10, 77, 90].

Previous works have focused on the overall, center-of-mass offset between the dark matter halos and their luminous components, but overlooked the differential offset from an extended body such as a disk galaxy. In particular, while an offset

between the centroids of light and total matter in cluster mergers must reach tens of kiloparsecs to be measurable, we find that displacements smaller than 1 kpc between the subhalo and the stellar disk can lead to clear morphological distortions.

However, perturbations that bend galaxy disks tend to damp out quickly, in a few rotation times [12], so the warps are not expected to be permanent features. Our simulations show that, after the warping phase, the stellar disk also does not revert back to a thin plane. Rather, in its final and relaxed state, sufficiently far from the densest parts of the host such that the drag force is again negligible, the stellar orbits spend significant time away from the galactic plane. We interpret this final state as an enhancement of the thickness of the initially thin disk.

## 4.3 Results

### 4.3.1 Measuring the Warping of Disks

As expected from our analytical arguments, we indeed find that galaxy disks in our simulations warp forwards, then oscillate and warp backwards, and then finally relax in a puffier state than at the beginning. To quantify the intensity of the warps, we fit a 3rd order polynomial to the 2D projection of the edge-on stellar disk:  $z(R) = aR^3 + bR^2 + cR + d$ , where  $z$  is the coordinate perpendicular to the plane of the disk and  $R$  is the radial distance along the disk's plane, from its center. Such a polynomial is able to capture the initial and final state of the disks, when

it should be well fit by a straight line, as well as the U and S warps, which will force a fit to large  $b$  and  $a$  coefficients, respectively. This choice of metric is simple and convenient for our present purposes, but we note that others are available and have been used in the literature (e.g. [106]). To fit the polynomial when there is some orientation angle, we first rotate the galaxy so that it aligns with the vertical axis. Since the warps oscillate and then vanish, the fitting coefficients reproduce this behavior by getting increased in magnitude and then eventually decreased back to nullity. While the prediction from equation (4.2.20) assumed a symmetric warp and employed the approximation of a constant disk potential, which breaks down for strong warps, we do check that the predicted values in Table 1 are compatible with the simulations.

We take the magnitude of coefficient  $b$  as a simple proxy of the U-warp intensity. To quantify some degree of theoretical uncertainty, we also obtain the error bars for  $b$  from the covariance matrix of the polynomial fitting. For a distant galaxy, one would hardly observe stars significantly further than a few scale radii from the disk center, due to the rapidly decaying flux caused by the lower stellar density. To avoid overestimating the observable warp intensity, we restrict the polynomial fit only to particles that lie within a sphere of radius equal to  $3h_0$  from the center of the subhalo, where  $h_0$  is the scale radius of the galaxy disk.

For a better understanding of the distortions, Figures 4.3 and 4.4 show simulation snapshots of the evolution of the warps with time. With all stellar disks

starting from the same initial conditions, we show in Figure 4.3 a snapshot of the  $\tilde{\sigma}/m_{\text{dm}} = 0.5 \text{ cm}^2\text{g}^{-1}$  and  $\tilde{\sigma}/m_{\text{dm}} = 1.0 \text{ cm}^2\text{g}^{-1}$ , 300 kpc–0 deg simulation, as well as the CDM case. The galaxies in the SIDM halos exhibit prominent U-warps. Notably, the stellar disk that inhabits the CDM subhalo displays a modest S-warp at the same time frame. It is clear from the figure that the galaxy in the standard CDM subhalo should not display a significant  $b$  coefficient as given by the polynomial fit. Notice that the  $\tilde{\sigma}/m_{\text{dm}} = 1.0 \text{ cm}^2\text{g}^{-1}$  panel on Figure 4.3 provides a check for the analytical prediction of Table 1. There is overall good agreement between the values in the 300 kpc row of that table and what is presented on Figure 4.3. For  $R = 3h_0 \gtrsim 10 \text{ kpc}$ , the predicted displacement of 0.95 kpc is in concordance with the visual displacement of around 1 kpc in that Figure.

Once the subhalo’s gravity dominates over the drag again, the warp oscillates backwards, as represented by Figure 4.4 by the snapshots at a time step around 200 My after those of Figure 4.3. Similarly, the S-shaped warp on the galaxy belonging to the CDM subhalo changes orientation.

Finally, at a later stage, around 1 Gy after the first warp and pericenter passage, the bending modes have decayed, and the remaining effect is an enhancement of the thickness of the stellar disk. Such disk heating is also a feature of gravitational interactions in a standard CDM scenario. Our simulations suggest, however, that a population of disks under SIDM should be thicker than their CDM counterparts due to the extra heating caused by the initial warping. For a quantitative analysis,



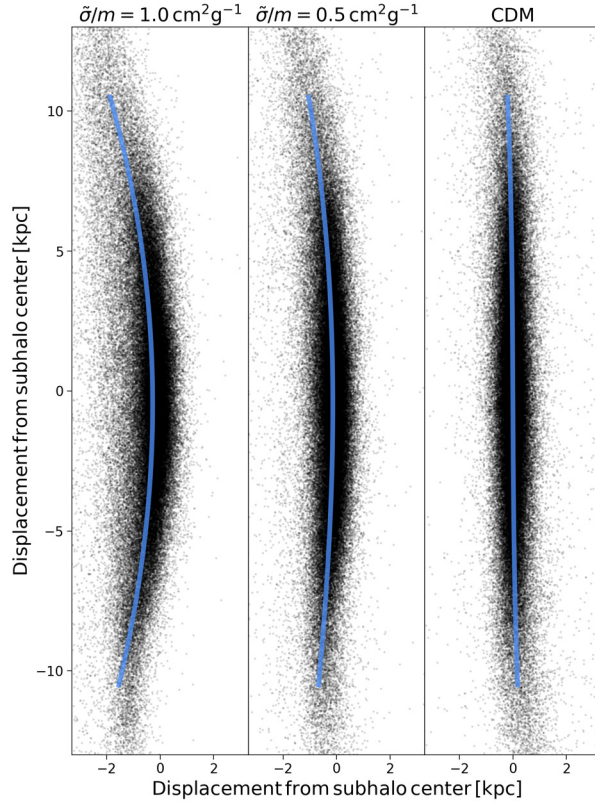


Figure 4.3: Snapshots from the simulations with 300 kpc pericenter and orientation angle  $0^\circ$ . Blue lines correspond to best-fit polynomials to the warp shape. From left to right, we display the two SIDM cross-sections analyzed and the standard CDM case. In all panels, the disk moves towards the left of the page, and the host’s center is located towards the bottom of the page, as suggested by Figure 4.1. The U-shaped warp is more severe on the case  $\tilde{\sigma}/m_{\text{dm}} = 1.0 \text{ cm}^2\text{g}^{-1}$ , and still very pronounced when  $\tilde{\sigma}/m_{\text{dm}} = 0.5 \text{ cm}^2\text{g}^{-1}$ , while the standard CDM case displays an S-shaped warp. The SIDM scenario is qualitatively very different than CDM.

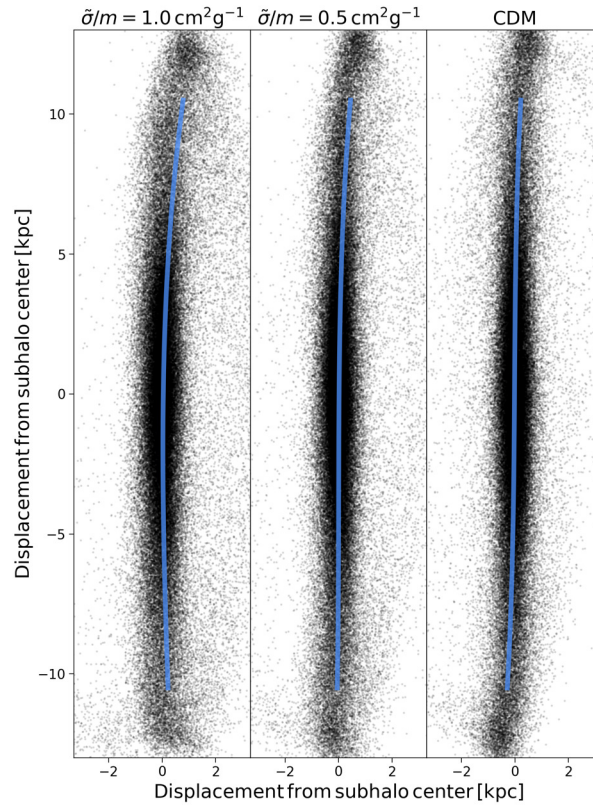


Figure 4.4: Same as Figure 4.3, around 200 My later. Both warps change orientation and the polynomial fit captures that change. As suggested again by Figure 4.1, the host’s center is located towards the right of the page.

we determine a metric for the disk thickness and apply it to simulation snapshots on the following Section.

In Figure 4.5 we show snapshots of the simulations for both choices of pericenter and all orientation angles at the maximal warping instant according to the polynomial fit, for the case  $\tilde{\sigma}/m_{\text{dm}} = 1.0 \text{ cm}^2\text{g}^{-1}$ . All panels show galaxies that inhabit SIDM subhalos, and the disk initial conditions are the same. The units on each axis correspond to the separation of the edge-on disks to the center of their respective subhalos. The general trend is that the 0 degree orientation angle (face-on onto the host) leads to more prominent, symmetric warps, while other inclination angles are somewhat asymmetric around the center of the subhalo. Also, a shorter pericenter leads to stronger distortions as it probes denser parts of the host halo.

Figure 4.5 also shows that, for inclinations that are not exactly face-on (orientation angle differing from zero), the stellar distribution can become significantly skewed within the disk plane. This skewness is another potential signature of DM self-interactions, in addition to the U-shaped warps and enhanced disk thickness. Our simulations suggest that SIDM-induced skewness can persist within satellite disks for times similar to the durations of the U-shaped warps. We defer a detailed study of SIDM-induced skewness to future work, and instead will focus on quantifying warp signatures and disk thickness.

In Figure 4.6 we show the evolution of the quadratic coefficient of the polynomial fit as a function of time for the 0° orientation angle in our 2 pericenters of interest.

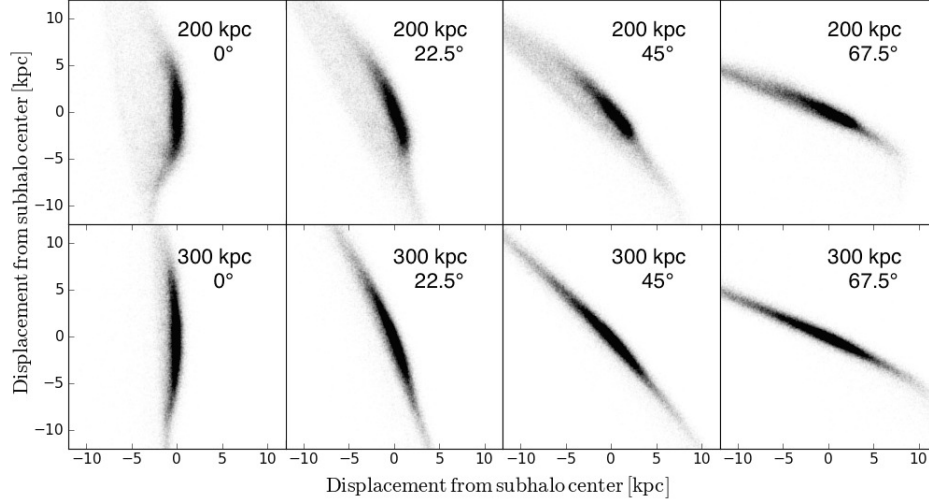


Figure 4.5: Snapshots of the maximum forward warp in 8 simulations with different pericenters and orientation angles, for  $\tilde{\sigma}/m_{\text{dm}} = 1.0 \text{ cm}^2\text{g}^{-1}$ . Black dots correspond to individual stars on the disk that inhabits an SIDM subhalo. The same initial conditions were used for the galaxies on each panel. The U-shaped warp is more prominent for smaller pericenters (when the subhalo probes a higher ambient density  $\rho_h$ ) and lower orientation angles (when the collision is closer to face-on as seen by the host halo). We also note, but leave for a future study, the fact that there is a skewness in the light distribution of disk galaxies at orientation angles larger than 0 degrees.

Negative values of  $b$  correspond to a parabolic U-shape in the forward direction of motion, while positive  $b$  values bend the disk backwards. In both panels, we see oscillations of the coefficient which eventually vanish as the disk aligns again with the subhalo center. The error bands are multiplied by a factor of 10 on those plots for better visualization.

We define the threshold for the detection of the warps to be  $|b| > 0.003$ , which is roughly an order of magnitude larger than the values this same coefficient reaches in the baseline CDM case due to fluctuations. For a very symmetric warp with  $z(R) \approx bR^2$ , this threshold value of  $b$  corresponds to a perpendicular displacement of approximately 0.03 kpc and 0.3 kpc as measured around the disk’s scale radius and three times the scale radius, respectively. After the first backwards warp (the first positive bump of the quadratic coefficient  $b$  on Figure 4.6), the galaxy disk is significantly thicker than how it was initialized, looking “puffy” rather than warped. Conservatively restricting ourselves to only one forwards plus one backwards warp, we find from the curves on Figure 4.6 that the period during which the warp could be detected on the least affected 0-degrees orientation case ( $\tilde{\sigma}/m_{\text{dm}} = 0.5 \text{ cm}^2\text{g}^{-1}$ , 300 kpc) is of around 0.1 Gy, while the most affected disk ( $\tilde{\sigma}/m_{\text{dm}} = 1.0 \text{ cm}^2\text{g}^{-1}$ , 200 kpc) is detectably warped for at least 0.4 Gy. The survival time of the U-shaped warp ultimately translates into a potentially observable sample size, which we further discuss in Section 4.4.

An important difference then becomes clear: for SIDM cross-sections within the

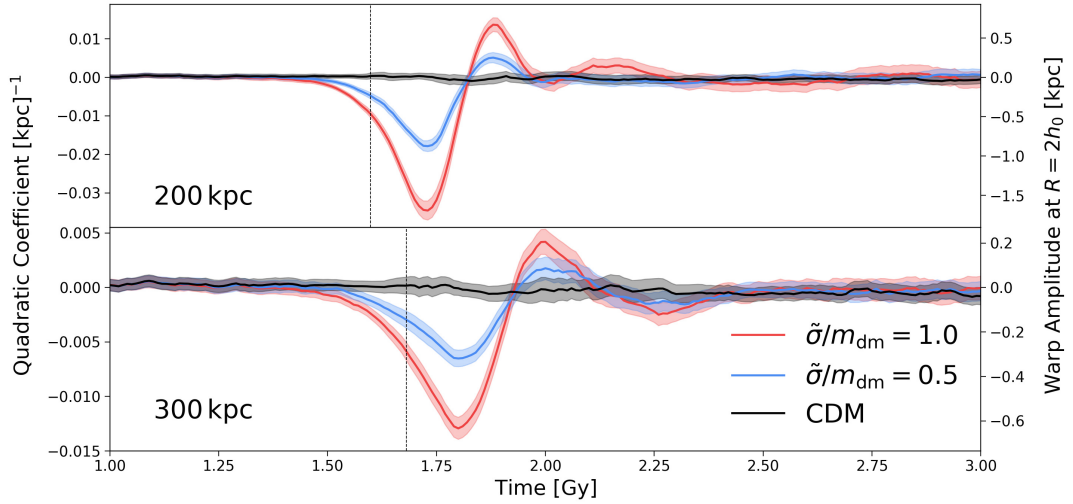


Figure 4.6: Quadratic coefficient  $b$  of the polynomial fit  $z(R) = aR^3 + bR^2 + cR + d$  as a function of time for two pericenters. This is a simple metric chosen among different possibilities (see text). On the right-hand axis, we show values for  $z(R) = bR^2$  at  $R = 2h_0$  (the displacement of the stellar disk at 2 scale radii). Note that the quadratic coefficient alone may not reproduce the exact warps apparent on Figures 4.3 and 4.4, where we fit the full polynomial. However, it captures the largest part of the observable warp effect. An estimate of the survival time of the warps is obtained from these curves (see text). Colored bands are estimates of the measurement error, obtained from the covariance of the fitted coefficient  $b$ , and are multiplied by a factor of 10 in the plot above for visualization. Vertical dashed lines mark the time at which galaxies reach the pericenter. Upper panel: 200 kpc pericenter,  $0^\circ$  orientation angle. Lower panel: 300 kpc pericenter,  $0^\circ$  orientation angle. In both cases, the CDM curve does not exhibit any appreciable U-shaped warp as given by this metric.

range that we have explored ( $0.5 < \tilde{\sigma}/m_{\text{dm}} < 1.0 \text{ cm}^2\text{g}^{-1}$ ), U-shaped stellar disks are expected to be quite general on galaxies that make a fast passing through a dense dark matter environment, such as a galaxy cluster. In standard CDM, such stellar disk warps should be rare when compared to their S-shaped counterparts. We expect that further work to measure the intensity of warps and how frequently they are found in observations can place tight constraints on  $\tilde{\sigma}/m_{\text{dm}}$ .

To complement Figures 4.5 and 4.6, we present Figure 4.7 comparing different orientation angles for the case  $\tilde{\sigma}/m_{\text{dm}} = 0.5 \text{ cm}^2\text{g}^{-1}$  with 300 kpc pericenter. We again show error bands which are multiplied by a factor of 10 for visualization. The trend is similar to that shown on Figure 4.5, with steeper angles displaying a less intense – but still detectable – warp signal when compared to the symmetric 0 deg case.

### 4.3.2 Measuring the Enhanced Disk Thickness

Once the transient warps decay and the galaxy reaches a new equilibrium configuration, we find that the resulting stellar disks are thicker in the SIDM subhalos when compared to their standard CDM counterparts. This happens because stars in SIDM galaxies get scattered to outer orbits following the warped phase. To quantify the thickness enhancement, we use simulation snapshots at around 3 Gy, when the disk is around its furthest distance from the host. We verify that the thickness is fairly constant around that time frame. On the 2D projection of the

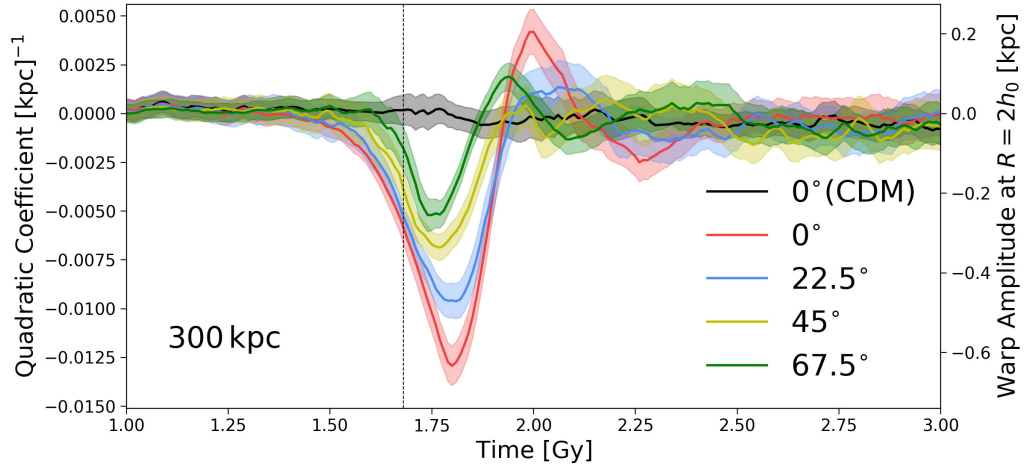


Figure 4.7: Same as Figure 4.6, but for multiple orientation angles in the 300 kpc pericenter case and cross-section  $\tilde{\sigma}/m_{\text{dm}} = 1.0 \text{ cm}^2 \text{ g}^{-1}$ . Steeper angles are not only more asymmetric (as seen from Figure 4.5), but also display a less intense warp. Similarly to the 0 deg case plotted above, other orientation angles for CDM are also null, as expected.



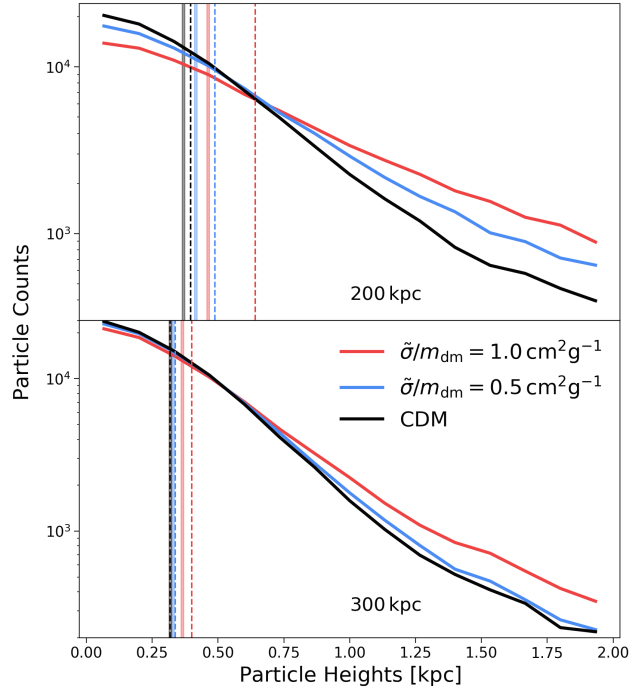


Figure 4.8: Histograms of disk particles selected to lie within a box of 3 scale radii and 5 scale heights from the galaxy center. Vertical bands correspond to the measurement of disk thickness as given by the standard deviation of the histograms, while dashed lines are scale height estimates from an exponential profile fit (see text). The uncertainty in the standard deviation metric is given by the band width and calculated from the mean  $\Delta_{\text{disk}}$  over 1 Gy. Upper panel: 200 kpc pericenter, 0 degree inclination angle. The measured thickness is  $\Delta_{\text{disk}}(\text{CDM}) = 0.32 \pm 0.006$  kpc,  $\Delta_{\text{disk}}(0.5 \text{ cm}^2 \text{g}^{-1}) = 0.39 \pm 0.008$  kpc and  $\Delta_{\text{disk}}(1.0 \text{ cm}^2 \text{g}^{-1}) = 0.46 \pm 0.010$  kpc. The exponential fit yields scale heights  $\tau(\text{CDM}) = 0.34$  kpc,  $\tau(0.5 \text{ cm}^2 \text{g}^{-1}) = 0.49$  kpc and  $\tau(1.0 \text{ cm}^2 \text{g}^{-1}) = 0.64$  kpc. Lower panel: 300 kpc pericenter, also with 0 degree inclination angle. The enhancement with respect to CDM is only significant for the cross-section of  $1.0 \text{ cm}^2 \text{g}^{-1}$ .

disk as seen by the observer, we first select only the particles that lie inside a box of radial range  $R = [-3h_0, 3h_0]$  and height range  $z = [-5z_0, 5z_0]$ , where  $h_0 \approx 3.5$  kpc is the initial scale length of the galaxy disk and  $z_0 = 0.1h_0$  is the initial scale height. In the cases with some nonzero orientation angle, we first rotate the galaxies by the known angle to align them with the vertical axis, and then select particles. This cut is supposed to represent only particles that could be detected as part of the stellar disk in actual observations in the same way we select particles before fitting the 3rd order polynomial.

We then make histograms of the height of these selected particles with respect to the disk plane, which in the edge-on view of the observer is simply given by the horizontal coordinate  $z$ . As a primary metric for the disk thickness, we use the standard deviation of the resulting distribution of particles  $\Delta_{\text{disk}} \equiv \sqrt{\langle z^2 \rangle - \langle z \rangle^2}$ . While the initial disk's transverse profile is, by construction, very well fit by a  $\text{sech}^2$  function according to equation (4.2.13) from which a scale height can be obtained, we make this choice because the final, thicker disks are not well fit by that expression. As the thickness differences between CDM and SIDM play a more significant role at around  $z \gtrsim 3z_0$ , we also fit an exponential profile proportional to  $e^{-z/\tau}$  as a secondary metric, where  $\tau$  is analogous to a new disk scale height. This fit is restricted within the range  $[2z_0, 4z_0]$ , where the profiles are well described by a single exponential length scale  $\tau$ . For a comparison with a control disk, we also measure both thickness metrics in a simulated system that does not go through

the host halo, but rather evolves in isolation in a CDM subhalo. After 3 Gy, the vertical profile of this isolated disk remains consistent with the initial conditions due to GalIC's success in finding a quasi-equilibrium configuration. We find  $\Delta_{\text{disk}}^{\text{isol.}} = 0.24 \text{ kpc}$  and  $\tau^{\text{isol.}} = 0.20 \text{ kpc}$  in this control system.

Figure 4.8 represents the obtained histograms at time 3 Gy for different cross-sections in the 200 kpc and 300 kpc pericenter cases, with orientation angle  $0^\circ$ . The vertical bands on both panels show the values of the thickness metric, and the uncertainty represented by their width corresponds to an averaging over  $\sim 1 \text{ Gy}$  around the turnaround time. For the 200 kpc case we obtain  $\Delta_{\text{disk}}(\text{CDM}) = 0.32 \pm 0.006 \text{ kpc}$ ,  $\Delta_{\text{disk}}(\tilde{\sigma}/m_{\text{dm}} = 0.5 \text{ cm}^2\text{g}^{-1}) = 0.39 \pm 0.008 \text{ kpc}$  and  $\Delta_{\text{disk}}(\tilde{\sigma}/m_{\text{dm}} = 1.0 \text{ cm}^2\text{g}^{-1}) = 0.46 \pm 0.010 \text{ kpc}$ . Notice that the CDM disk also gets thicker due to tidal interactions alone, which is a potential systematic uncertainty. On both panels, a larger cross-section leads to a thicker disk, but the discrepancy is more prominent for smaller pericenters, which probe a higher number of SIDM interactions, a trend similar to that of the U-shaped warps. Dashed lines correspond to the secondary metric, the exponential fit, which capture mostly the difference in the histogram tails. For the 200 kpc case we obtain  $\tau(\text{CDM}) = 0.34 \text{ kpc}$ ,  $\tau(\tilde{\sigma}/m_{\text{dm}} = 0.5 \text{ cm}^2\text{g}^{-1}) = 0.49 \text{ kpc}$  and  $\tau(\tilde{\sigma}/m_{\text{dm}} = 1.0 \text{ cm}^2\text{g}^{-1}) = 0.64 \text{ kpc}$ . Both pericenters show a slightly stronger SIDM signal in the  $\tau$  metric than in  $\Delta_{\text{disk}}$ .

We note that including particles away from the limits  $|z| < 5z_0$  in the calculation of  $\Delta_{\text{disk}}$  increases the enhancement effect. That is mostly due to the fact that the

disks in SIDM halos actually have a considerable number of particles spread out to much further heights, while the CDM histogram decays very quickly and has little contribution at  $z > 5z_0$ , as can be seen from Figure 4.8. This implies that our selection of particles is conservative for observational purposes.

The survival time for the enhanced thickness is considerably longer than that of the U-warps. We find that during at least 1 Gy the histograms presented in Figure 4.8 remain very stable despite the orbital motion of particles. In fact, due to the collisionless nature of stars, it is not expected that the stellar disk will completely revert back to a thin plane, since that would require some energy to be radiated away.

We thus conclude that this is another interesting difference between morphologies in SIDM and CDM in cluster environments. While, in both scenarios, a disk that has made a fast passage through a dense dark matter environment should become thicker, the currently allowed SIDM cross-sections can lead to an enhancement of that effect. A consequence of this conclusion is that field galaxies which have never been inside cluster environments should be relatively thinner, both in CDM and SIDM, than those inside clusters.

A caveat is worth noting: one should expect the cluster environment to be more disturbing to disks than our single-galaxy simulations can capture. This could lead to a statistically increased thickness of edge-on disks even in the absence of SIDM, for instance due to tidal interactions with many potential close neighbors other than

the host itself.

### 4.3.3 Variations of the Cluster and Galaxy Properties

As expected from our theoretical estimates in Section 4.2.4, our results on the previous sections are somewhat sensitive to the initial choice of the fiducial system – the host and subhalo masses and their concentration, the initial galaxy thickness, etc. We consider here variations of these physical parameters. In the next Section, we also vary the “unphysical” parameters of the simulation, for instance the number of particles and the gravitational softening scale. We also test, to some extent, the initial simplifying approximations made explicit in Section 4.2.2. To accomplish these tests, we simply run a new suite of simulations changing, whenever possible, only one relevant parameter at a time.

The physical characteristics of the system, like halo profiles and galaxy length scales, are ultimately a set of nuisance parameters that one would marginalize over, in some sense, when trying to infer the SIDM cross-section  $\tilde{\sigma}/m_{\text{dm}}$  from actual observations. That is due to the fact that the results shown in Sections 4.3.1 and 4.3.2 are expected to have a dependence on these parameters.

When we vary the host and subhalo profiles, the resulting warp strength follows the trend expected from the analytical derivation in Section 4.2.4. Increasing the concentration of the subhalo, at fixed mass, from the fiducial choice  $c = 8$  to  $c = 12$  yields a more cuspy halo which consequently produces a stronger restoring force on

the distorted galaxy disk. The disk warp is expected to be less intense. Indeed, the resulting warp curve for the 200 kpc,  $\tilde{\sigma}/m_{\text{dm}} = 1.0 \text{ cm}^2\text{g}^{-1}$  case then reaches a minimum coefficient  $b = -0.024 \text{ kpc}^{-1}$ , approximately 30% less intense than the fiducial case (see Figure 4.6). The same trend is expected when the subhalo mass is increased from the fiducial  $M_{\text{sh}} = 10^{12} M_{\odot}$  to  $5 \times 10^{12} M_{\odot}$ , and we confirm that the most intense warp coefficient is 50% smaller than the fiducial scenario. Conversely, for a less massive subhalo with  $M_{\text{sh}} = 5 \times 10^{11} M_{\odot}$ , the maximum warp is 50% larger than the fiducial case on Figure 4.6. In these tests, the galaxy and host halo properties were kept the same as the fiducial choice.

We run another set of tests modifying the host profile parameters. We simultaneously change the initial infall distance of the disk galaxy to match the virial radius of the new host. The other galaxy parameters remain fixed at their fiducial values and again we look at the case 200 kpc,  $\tilde{\sigma}/m_{\text{dm}} = 1.0 \text{ cm}^2\text{g}^{-1}$  with 0 deg orientation angle. Decreasing the host mass from  $10^{15} M_{\odot}$  to  $5 \times 10^{14} M_{\odot}$ , at fixed concentration, reduces the maximum warp by around 60%, resulting in  $b = -0.014 \text{ kpc}^{-1}$  at maximal warping. Also, further reducing it to  $10^{14} M_{\odot}$  significantly reduces the maximum warp intensity to  $b = -0.001 \text{ (kpc)}^{-1}$ , below our defined detection limit of  $|b| > 0.003 \text{ (kpc)}^{-1}$ . This again follows the trend described in Section 4.2.4: reducing the mass at fixed concentration makes the host less dense at its center, leading to a weaker SIDM drag force from equation (4.2.8), and consequently subtler distortions.

We also modify the disk’s structural parameters. Reducing the stellar mass from  $3 \times 10^{10} M_{\odot}$  to  $10^{10} M_{\odot}$  and changing the initial scale height from  $z_0 = 0.1h_0$  to  $z_0 = 0.05h_0$  and  $z_0 = 0.2h_0$  did not produce changes larger than 10% on the warp intensity.

In all of the tests above regarding the physical parameters of the system, we also look at the effect on the disk thickening. With respect to our fiducial case, all variations caused only marginal changes on  $\Delta_{\text{disk}}$  below  $\pm 10\%$ , to the final thickness of the stellar disk in the  $\tilde{\sigma}/m_{\text{dm}} = 1.0 \text{ cm}^2 \text{ g}^{-1}$  SIDM subhalo (see Figure 4.8).

#### 4.3.4 Tests of Numerical Approximations

We proceed to test the numerical, “unphysical” simulation parameters and our initial approximations. The (constant) softening length used in our simulation runs was of 50 pc, considerably shorter than the length scales of the effects we have studied. We performed several runs with softening as small as 25 pc and as large as 200 pc and found no significant difference in the obtained results. We were focusing specially on the evolution of the disk thickness when this parameter changed, since spurious 2-body scatterings can lead to heating of the galaxy disk followed by an increase in its thickness.

To make sure our results are not an artifact of integration accuracy, we also experiment with GIZMO’s tree construction frequency and the maximum allowed size of the time steps. We find no significant difference in our measurements when

the tree updating is made faster by an order of magnitude, and the same for when the maximum time step allowed is made lower by one and two orders of magnitude. We also increase and decrease the number of disk particles by a factor of 2 and find subpercent differences in the warp intensity of thickness measurements. We thus conclude that our results are fully converged.

Finally, we test approximations (ii) and (iii) in Section 4.2.2 by implementing simulations with both the subhalo and host described by dynamic, gravitating N-body particles. We run these N-body simulations by modifying GADGET-2 [96] to include self interacting dark matter with anisotropic scattering cross-section [5]. The disk was again generated using GalIC. The simulations used  $2 \times 10^7$  particles for the host halo of mass  $10^{15} M_{\odot}$ ,  $2 \times 10^4$  for the subhalo with mass  $10^{12} M_{\odot}$  and  $10^4$  particles in the  $3 \times 10^{10} M_{\odot}$  disk. In general, anisotropic self-interactions will give rise to both evaporation of the subhalo as well as a drag. To isolate the effect of drag on the galaxy disk system we run a drag-only implementation where each simulation particle is considered to be representative of an ensemble of microscopic particles and the net drag force can be evaluated using equation (4.2.7). In this case we find that strong warps are produced in the galaxy disk even when the outer regions of the subhalo are largely distorted by tidal interactions. This is consistent with our assumption that the warp is sensitive to the subhalo profile within the scales of the disk radius, which does not change significantly due to tidal interactions. The drag-only case by itself is not energy conserving. We run another set of simulations



where we implement the full physical picture with drag and evaporation. We treat interactions between simulation particles as if they represent actual microscopic particles - i.e. we use the total cross section  $\sigma$  to decide if two neighboring particles interact or not, and then by choosing the scattering angle  $\theta$  using the probability distribution for  $\theta$  from the form of  $d\sigma/d\Omega$  [5]. Since these interactions change the velocities of the interacting particles in both the direction parallel to the relative velocity of the particles, as well as in the direction perpendicular to it, this method naturally incorporates the effects of both drag as well as subhalo evaporation arising from self-interactions.

Since evaporation affects the entire subhalo profile, we find that for the cross-section used in this work (equation 4.2.2) the warping can be suppressed in our fiducial 300 kpc pericenter case. Conversely, the disk thickening is enhanced due to mass loss from the subhalo. However, when performing a full simulation for the idealized scenario of a completely radial trajectory for the subhalo, we find measurable disk warps, even though their magnitude is smaller than the drag-only case. It must be noted that the amount of evaporation and drag can be affected differently as both depend on the nature of  $d\sigma/d\Omega$  [60]. These simulations are currently in the process of development and it will be of interest to do a detailed analysis on how different cross-sections affect the warping of galaxy disks.

## 4.4 Discussion

We have studied the impact of dark matter self-interactions on the morphology of disk galaxies in galaxy cluster environments. The effective drag force of SIDM causes an offset between the dark matter subhalo and stars of the disk galaxy. The restoring force from the dark matter then causes the stellar disk to be distorted. We use modified N-body simulations to model anisotropic, velocity-independent SIDM and focus on the morphology of disk galaxies as they pass through a large galaxy cluster. In Figures 4.3-4.5 we show the distortions of an edge-on disk. Our quantitative results focus on the symmetric, U-shaped warp and thickening of the disk. For SIDM cross-sections of 0.5 to  $1 \text{ cm}^2\text{g}^{-1}$ , we find that a disk galaxy with pericenter  $\lesssim 300 \text{ kpc}$  gets significantly warped, and the warp oscillates on a timescale of a few hundred million years (Figures 4.6 and 4.7) before decaying and leaving a thickened disk (Figure 4.8). Thus we have identified the warping and thickening as distinct signatures of SIDM; more generally asymmetries in the light distribution arise once the disk is offset from the dark matter.

Several caveats apply to our simulation findings and to a detailed connection to observations. We show tests with full simulations in which the dark matter halos are populated with particles, and are therefore susceptible to evaporation, rather than having their motion approximated by the drag force. Detailed studies with such simulations are needed to obtain the full range of SIDM effects and make accurate observational predictions. In addition, our predictions are expected to

apply robustly only to galaxies for which the dark matter dominates the gravity at least towards the outer parts of the disk.

The prospects for observational detection of these SIDM signatures also hinge on a robust understanding of disk galaxies in standard CDM, so that comparative statements can be made. This generally requires inclusion of gas physics. Disk galaxies are expected to be quenched, and therefore redder in color, and tidally distorted near the cluster center – detailed predictions are challenging to obtain as feedback processes and other gas physics remains uncertain. There are several observational challenges as well. Perhaps the biggest observational uncertainty is in the true 3-D distance of observed disk galaxies from the cluster center. Other possible sources of uncertainty are the inclination angle with respect to the observer (when the disk is not exactly edge-on), the location of the cluster center and the dark matter density near it, and the gravitational influence of the galactic subhalo’s dark matter over the stellar disk. The amount of time the disk galaxy has spent inside the cluster is an additional factor, as it may not be on its first passage.

Given these caveats, one can take two approaches to connect robust SIDM predictions to observations. The first is to identify warped or otherwise distorted galaxies and compare their properties to CDM and SIDM predictions. The fraction of warped galaxies, the qualitative signature of the warp (S-shaped vs. U-shaped), and other features differ in the two models. Even a small sample of warped disk galaxies near cluster centers would be useful: the presence of U-shaped warps in

such galaxies could support an SIDM explanation. This approach can already be implemented with more detailed predictions, as imaging of nearby disk galaxies with measured morphological properties has been obtained by the Sloan Digital Sky Survey (SDSS)<sup>5</sup> and other surveys. However, the lack of such warped disks would be harder to interpret: if we only have projected positions, one must take into account the fact that, even in standard CDM, disk galaxies may simply not survive very close to the center, so disk galaxies observed near the cluster center may have a large 3-D distance. The second approach is more statistical: analyze all disk galaxies as a function of projected distance from the cluster and compare to an ensemble of such galaxies in simulations. The presence of warps that last a few hundred million years suggest that a non-negligible fraction of disks at small radii would be observed to have U-warps in SIDM.

High resolution, multi-color images of galaxies in galaxy clusters would be the appropriate sample for such tests. With ongoing and planned imaging surveys such as the Dark Energy Survey (DES)<sup>6</sup>, Subaru-HSC<sup>7</sup>, the Kilo Degree Survey (KiDS)<sup>8</sup>, the Wide Field InfraRed Survey Telescope (WFIRST)<sup>9</sup> and Euclid<sup>10</sup>, large samples of low-redshift clusters with well resolved galaxies will be available. In addition to the warping, thickening and other observed effects in simulations, one could also

---

<sup>5</sup><http://www.sdss.org/>

<sup>6</sup><https://www.darkenergysurvey.org/>

<sup>7</sup><http://hsc.mtk.nao.ac.jp/ssp/survey/>

<sup>8</sup><http://kids.strw.leidenuniv.nl/>

<sup>9</sup><https://wfirst.gsfc.nasa.gov/>

<sup>10</sup><http://sci.esa.int/euclid/>

use velocity signatures from spatially resolved spectroscopy of face-on disks. We find that in the oscillation phase, beyond the scale radius the disk moves with an azimuthally symmetric velocity of 10's of km/s. This could lead to Doppler shifts between the edges and the center of the face-on disk. Yet another potentially interesting effect that we defer to future work is a skewness in the light profile of galaxies, as suggested by Figure 4.5. In such a scenario, nearby elliptical galaxies would also be interesting candidates to probe SIDM cross-sections.

A more detailed discussion of observational strategy is beyond the scope of this work since we have only simulated a few simple cases of disk galaxy infall. We leave for future work with detailed simulations the full prediction of galaxy morphologies in SIDM, and a more comprehensive connection to observational prospects.

# Bibliography

- [1] B. Abbott, R. Abbott, T. Abbott, F. Acernese, K. Ackley, C. Adams, T. Adams, P. Addesso, R. Adhikari, V. Adya, and et al. Gw170817: Observation of gravitational waves from a binary neutron star inspiral. *Physical Review Letters*, 119(16), Oct 2017.
- [2] T. M. C. Abbott, F. B. Abdalla, A. Alarcon, J. Aleksić, S. Allam, S. Allen, A. Amara, J. Annis, J. Asorey, S. Avila, D. Bacon, E. Balbinot, M. Banerji, N. Banik, W. Barkhouse, M. Baumer, E. Baxter, K. Bechtol, M. R. Becker, A. Benoit-Lévy, B. A. Benson, G. M. Bernstein, E. Bertin, J. Blazek, S. L. Bridle, D. Brooks, D. Brout, E. Buckley-Geer, D. L. Burke, M. T. Busha, A. Campos, D. Capozzi, A. Carnero Rosell, M. Carrasco Kind, J. Carretero, F. J. Castander, R. Cawthon, C. Chang, N. Chen, M. Childress, A. Choi, C. Conselice, R. Crittenden, M. Crocce, C. E. Cunha, C. B. D'Andrea, L. N. da Costa, R. Das, T. M. Davis, C. Davis, J. De Vicente, D. L. DePoy, J. DeRose, S. Desai, H. T. Diehl, J. P. Dietrich, S. Dodelson, P. Doel, A. Drlica-Wagner, T. F. Eifler, A. E. Elliott, F. Elsner, J. Elvin-Poole,

J. Estrada, A. E. Evrard, Y. Fang, E. Fernandez, A. Ferté, D. A. Finley, B. Flaugher, P. Fosalba, O. Friedrich, J. Frieman, J. García-Bellido, M. Garcia-Fernandez, M. Gatti, E. Gaztanaga, D. W. Gerdes, T. Giannantonio, M. S. S. Gill, K. Glazebrook, D. A. Goldstein, D. Gruen, R. A. Gruendl, J. Gschwend, G. Gutierrez, S. Hamilton, W. G. Hartley, S. R. Hinton, K. Honscheid, B. Hoyle, D. Huterer, B. Jain, D. J. James, M. Jarvis, T. Jeltema, M. D. Johnson, M. W. G. Johnson, T. Kacprzak, S. Kent, A. G. Kim, A. King, D. Kirk, N. Kokron, A. Kovacs, E. Krause, C. Krawiec, A. Kremin, K. Kuehn, S. Kuhlmann, N. Kuropatkin, F. Lacasa, O. Lahav, T. S. Li, A. R. Liddle, C. Lidman, M. Lima, H. Lin, N. MacCrann, M. A. G. Maia, M. Makler, M. Manera, M. March, J. L. Marshall, P. Martini, R. G. McMahon, P. Melchior, F. Menanteau, R. Miquel, V. Miranda, D. Mudd, J. Muir, A. Möller, E. Neilsen, R. C. Nichol, B. Nord, P. Nugent, R. L. C. Ogando, A. Palmese, J. Peacock, H. V. Peiris, J. Peoples, W. J. Percival, D. Petravick, A. A. Plazas, A. Porredon, J. Prat, A. Pujol, M. M. Rau, A. Refregier, P. M. Ricker, N. Roe, R. P. Rollins, A. K. Romer, A. Roodman, R. Rosenfeld, A. J. Ross, E. Rozo, E. S. Rykoff, M. Sako, A. I. Salvador, S. Samuroff, C. Sánchez, E. Sanchez, B. Santiago, V. Scarpine, R. Schindler, D. Scolnic, L. F. Secco, S. Serrano, I. Sevilla-Noarbe, E. Sheldon, R. C. Smith, M. Smith, J. Smith, M. Soares-Santos, F. Sobreira, E. Suchyta, G. Tarle, D. Thomas, M. A. Troxel, D. L. Tucker, B. E. Tucker, S. A. Uddin, T. N. Varga, P. Vielzeuf, V. Vikram,

A. K. Vivas, A. R. Walker, M. Wang, R. H. Wechsler, J. Weller, W. Wester, R. C. Wolf, B. Yanny, F. Yuan, A. Zenteno, B. Zhang, Y. Zhang, J. Zuntz, and Dark Energy Survey Collaboration. Dark Energy Survey year 1 results: Cosmological constraints from galaxy clustering and weak lensing. , 98(4):043526, Aug. 2018.

- [3] T. M. C. Abbott, F. B. Abdalla, S. Avila, M. Banerji, E. Baxter, K. Bechtol, M. R. Becker, E. Bertin, J. Blazek, S. L. Bridle, D. Brooks, D. Brout, D. L. Burke, A. Campos, A. Carnero Rosell, M. Carrasco Kind, J. Carretero, F. J. Castander, R. Cawthon, C. Chang, A. Chen, M. Crocce, C. E. Cunha, L. N. da Costa, C. Davis, J. De Vicente, J. DeRose, S. Desai, E. Di Valentino, H. T. Diehl, J. P. Dietrich, S. Dodelson, P. Doel, A. Drlica-Wagner, T. F. Eifler, J. Elvin-Poole, A. E. Evrard, E. Fernandez, A. Ferté, B. Flaugher, P. Fosalba, J. Frieman, J. García-Bellido, E. Gaztanaga, D. W. Gerdes, T. Giannantonio, D. Gruen, R. A. Gruendl, J. Gschwend, G. Gutierrez, W. G. Hartley, D. L. Hollowood, K. Honscheid, B. Hoyle, D. Huterer, B. Jain, T. Jeltema, M. W. G. Johnson, M. D. Johnson, A. G. Kim, E. Krause, K. Kuehn, N. Kuropatkin, O. Lahav, S. Lee, P. Lemos, C. D. Leonard, T. S. Li, A. R. Liddle, M. Lima, H. Lin, M. A. G. Maia, J. L. Marshall, P. Martini, F. Menanteau, C. J. Miller, R. Miquel, V. Miranda, J. J. Mohr, J. Muir, R. C. Nichol, B. Nord, R. L. C. Ogando, A. A. Plazas, M. Raveri, R. P. Rollins, A. K. Romer, A. Roodman, R. Rosenfeld, S. Samuroff, E. Sanchez, V. Scarpine,



R. Schindler, M. Schubnell, D. Scolnic, L. F. Secco, S. Serrano, I. Sevilla-Noarbe, M. Smith, M. Soares-Santos, F. Sobreira, E. Suchyta, M. E. C. Swanson, G. Tarle, D. Thomas, M. A. Troxel, V. Vikram, A. R. Walker, N. Weaverdyck, R. H. Wechsler, J. Weller, B. Yanny, Y. Zhang, J. Zuntz, and DES Collaboration. Dark Energy Survey year 1 results: Constraints on extended cosmological models from galaxy clustering and weak lensing. , 99(12):123505, June 2019.

[4] S. Alam, M. Ata, S. Bailey, F. Beutler, D. Bizyaev, J. A. Blazek, A. S. Bolton, J. R. Brownstein, A. Burden, C.-H. Chuang, and et al. The clustering of galaxies in the completed sdss-iii baryon oscillation spectroscopic survey: cosmological analysis of the dr12 galaxy sample. *Monthly Notices of the Royal Astronomical Society*, 470(3):2617–2652, Mar 2017.

[5] A. Banerjee et al. In Prep.

[6] N. Benitez. Bayesian photometric redshift estimation. *The Astrophysical Journal*, 536(2):571–583, jun 2000.

[7] G. M. Bernstein, R. Armstrong, C. Krawiec, and M. C. March. An accurate and practical method for inference of weak gravitational lensing from galaxy images. , 459(4):4467–4484, July 2016.

[8] G. M. Bernstein and M. Jarvis. Shapes and Shears, Stars and Smears: Optimal Measurements for Weak Lensing. , 123(2):583–618, Feb. 2002.

- [9] J. Binney. Warps. *Annual Review of Astronomy and Astrophysics*, 30(1):51–74, 1992.
- [10] J. Binney. WARPS. , 30:51–74, 1992.
- [11] J. Binney and M. Merrifield. *Galactic Astronomy*. 1998.
- [12] J. Binney and S. Tremaine. *Galactic Dynamics: Second Edition*. Princeton University Press, 2008.
- [13] S. Bird, M. Viel, and M. G. Haehnelt. Massive neutrinos and the non-linear matter power spectrum. *Monthly Notices of the Royal Astronomical Society*, 420(3):2551–2561, 02 2012.
- [14] J. Blazek, Z. Vlah, and U. Seljak. Tidal alignment of galaxies. , 2015(8):015, Aug. 2015.
- [15] J. A. Blazek, N. MacCrann, M. A. Troxel, and X. Fang. Beyond linear galaxy alignments. , 100(10):103506, Nov. 2019.
- [16] S. Bridle and L. King. Dark energy constraints from cosmic shear power spectra: impact of intrinsic alignments on photometric redshift requirements. *New Journal of Physics*, 9(12):444, Dec. 2007.
- [17] M. L. Brown, A. N. Taylor, N. C. Hambly, and S. Dye. Measurement of intrinsic alignments in galaxy ellipticities. *Monthly Notices of the Royal Astronomical Society*, 333(3):501–509, 07 2002.

- [18] S. M. Carroll. *Spacetime and geometry. An introduction to general relativity*. 2004.
- [19] S. M. Carroll, M. Hoffman, and M. Trodden. Can the dark energy equation-of-state parameter  $w$  be less than  $-1$ ? , 68(2):023509, July 2003.
- [20] P. Catelan, M. Kamionkowski, and R. D. Blandford. Intrinsic and extrinsic galaxy alignment. , 320(1):L7–L13, Jan. 2001.
- [21] D. Clowe, M. Bradač, A. H. Gonzalez, M. Markevitch, S. W. Randall, C. Jones, and D. Zaritsky. A Direct Empirical Proof of the Existence of Dark Matter. , 648(2):L109–L113, Sept. 2006.
- [22] P. Collaboration, N. Aghanim, Y. Akrami, M. Ashdown, J. Aumont, C. Bacigalupi, M. Ballardini, A. J. Banday, R. B. Barreiro, N. Bartolo, S. Basak, R. Battye, K. Benabed, J. P. Bernard, M. Bersanelli, P. Bielewicz, J. J. Bock, J. R. Bond, J. Borrill, F. R. Bouchet, F. Boulanger, M. Bucher, C. Burigana, R. C. Butler, E. Calabrese, J. F. Cardoso, J. Carron, A. Challinor, H. C. Chiang, J. Chluba, L. P. L. Colombo, C. Combet, D. Contreras, B. P. Crill, F. Cuttaia, P. de Bernardis, G. de Zotti, J. Delabrouille, J. M. Delouis, E. D. Valentino, J. M. Diego, O. Doré, M. Douspis, A. Ducout, X. Dupac, S. Dusini, G. Efstathiou, F. Elsner, T. A. Enßlin, H. K. Eriksen, Y. Fantaye, M. Farhang, J. Fergusson, R. Fernandez-Cobos, F. Finelli, F. Forastieri, M. Frailis, A. A. Fraisse, E. Franceschi, A. Frolov, S. Galeotta, S. Galli, K. Ganga, R. T.

Génova-Santos, M. Gerbino, T. Ghosh, J. González-Nuevo, K. M. Górski, S. Gratton, A. Gruppuso, J. E. Gudmundsson, J. Hamann, W. Handley, F. K. Hansen, D. Herranz, S. R. Hildebrandt, E. Hivon, Z. Huang, A. H. Jaffe, W. C. Jones, A. Karakci, E. Keihänen, R. Keskitalo, K. Kiiveri, J. Kim, T. S. Kisner, L. Knox, N. Krachmalnicoff, M. Kunz, H. Kurki-Suonio, G. Lagache, J. M. Lamarre, A. Lasenby, M. Lattanzi, C. R. Lawrence, M. L. Jéune, P. Lemos, J. Lesgourgues, F. Levrier, A. Lewis, M. Liguori, P. B. Lilje, M. Lilley, V. Lindholm, M. López-Cañiego, P. M. Lubin, Y. Z. Ma, J. F. Macías-Pérez, G. Maggio, D. Maino, N. Mandolesi, A. Mangilli, A. Marcos-Caballero, M. Maris, P. G. Martin, M. Martinelli, E. Martínez-González, S. Matarrese, N. Mauri, J. D. McEwen, P. R. Meinhold, A. Melchiorri, A. Mennella, M. Migliaccio, M. Millea, S. Mitra, M. A. Miville-Deschênes, D. Molinari, L. Montier, G. Morgante, A. Moss, P. Natoli, H. U. Nørgaard-Nielsen, L. Pagano, D. Paoletti, B. Partridge, G. Patanchon, H. V. Peiris, F. Perrotta, V. Pettorino, F. Piacentini, L. Polastri, G. Polenta, J. L. Puget, J. P. Rachen, M. Reinecke, M. Remazeilles, A. Renzi, G. Rocha, C. Rosset, G. Roudier, J. A. Rubiño-Martín, B. Ruiz-Granados, L. Salvati, M. Sandri, M. Savelainen, D. Scott, E. P. S. Shellard, C. Sirignano, G. Sirri, L. D. Spencer, R. Sunyaev, A. S. Suur-Uski, J. A. Tauber, D. Tavagnacco, M. Tenti, L. Toffolatti, M. Tomasi, T. Trombetti, L. Valenziano, J. Valiviita, B. V. Tent, L. Vibert, P. Vielva, F. Villa, N. Vittorio, B. D. Wandelt, I. K. Wehus, M. White,

- S. D. M. White, A. Zacchei, and A. Zonca. Planck 2018 results. vi. cosmological parameters, 2018.
- [23] R. Davé, D. N. Spergel, P. J. Steinhardt, and B. D. Wandelt. Halo Properties in Cosmological Simulations of Self-interacting Cold Dark Matter. *Phys. Rev. D*, 547(2):574–589, Feb. 2001.
- [24] S. Dodelson. *Modern Cosmology*. Academic Press, Amsterdam, 2003.
- [25] S. Dodelson. *Gravitational Lensing*. 2017.
- [26] S. Dodelson and M. D. Schneider. The effect of covariance estimator error on cosmological parameter constraints. *Phys. Rev. D*, 88:063537, Sep 2013.
- [27] A. Drlica-Wagner, I. Sevilla-Noarbe, E. S. Rykoff, R. A. Gruendl, B. Yanny, D. L. Tucker, B. Hoyle, A. C. Rosell, G. M. Bernstein, K. Bechtol, M. R. Becker, A. Benoit-Lévy, E. Bertin, M. C. Kind, C. Davis, J. de Vicente, H. T. Diehl, D. Gruen, W. G. Hartley, B. Leistedt, T. S. Li, J. L. Marshall, E. Neilsen, M. M. Rau, E. Sheldon, J. Smith, M. A. Troxel, S. Wyatt, Y. Zhang, T. M. C. Abbott, F. B. Abdalla, S. Allam, M. Banerji, D. Brooks, E. Buckley-Geer, D. L. Burke, D. Capozzi, J. Carretero, C. E. Cunha, C. B. D’Andrea, L. N. da Costa, D. L. DePoy, S. Desai, J. P. Dietrich, P. Doel, A. E. Evrard, A. F. Neto, B. Flaugher, P. Fosalba, J. Frieman, J. García-Bellido, D. W. Gerdes, T. Giannantonio, J. Gschwend, G. Gutierrez, K. Honscheid, D. J. James, T. Jeltema, K. Kuehn, S. Kuhlmann, N. Kuropatkin, O. Lahav,

- M. Lima, H. Lin, M. A. G. Maia, P. Martini, R. G. McMahon, P. Melchior, F. Menanteau, R. Miquel, R. C. Nichol, R. L. C. Ogando, A. A. Plazas, A. K. Romer, A. Roodman, E. Sanchez, V. Scarpine, R. Schindler, M. Schubnell, M. Smith, R. C. Smith, M. Soares-Santos, F. Sobreira, E. Suchyta, G. Tarle, V. Vikram, A. R. Walker, R. H. Wechsler, and J. Z. and. Dark energy survey year 1 results: The photometric data set for cosmology. *The Astrophysical Journal Supplement Series*, 235(2):33, apr 2018.
- [28] J. Dubinski and R. G. Carlberg. The Structure of Cold Dark Matter Halos. , 378:496, Sept. 1991.
- [29] X. Fang, J. A. Blazek, J. E. McEwen, and C. M. Hirata. FAST-PT II: an algorithm to calculate convolution integrals of general tensor quantities in cosmological perturbation theory. , 2017(2):030, Feb. 2017.
- [30] F. Feroz, M. P. Hobson, and M. Bridges. MULTINEST: an efficient and robust Bayesian inference tool for cosmology and particle physics. , 398(4):1601–1614, Oct. 2009.
- [31] P. G. Ferreira and C. Skordis. Linear growth rate of structure in parametrized post-Friedmannian universes. , 81(10):104020, May 2010.
- [32] B. Flaugher, H. T. Diehl, K. Honscheid, T. M. C. Abbott, O. Alvarez, R. Angstadt, J. T. Annis, M. Antonik, O. Ballester, L. Beaufore, G. M. Bernstein, R. A. Bernstein, B. Bigelow, M. Bonati, D. Boprie, D. Brooks,

E. J. Buckley-Geer, J. Campa, L. Cardiel-Sas, F. J. Castander, J. Castilla, H. Cease, J. M. Cela-Ruiz, S. Chappa, E. Chi, C. Cooper, L. N. da Costa, E. Dede, G. Derylo, D. L. DePoy, J. de Vicente, P. Doel, A. Drlica-Wagner, J. Eiting, A. E. Elliott, J. Emes, J. Estrada, A. F. Neto, D. A. Finley, R. Flores, J. Frieman, D. Gerdes, M. D. Gladders, B. Gregory, G. R. Gutierrez, J. Hao, S. E. Holland, S. Holm, D. Huffman, C. Jackson, D. J. James, M. Jonas, A. Karcher, I. Karliner, S. Kent, R. Kessler, M. Kozlovsky, R. G. Kron, D. Kubik, K. Kuehn, S. Kuhlmann, K. Kuk, O. Lahav, A. Lathrop, J. Lee, M. E. Levi, P. Lewis, T. S. Li, I. Mandrichenko, J. L. Marshall, G. Martinez, K. W. Merritt, R. Miquel, F. Muñoz, E. H. Neilsen, R. C. Nichol, B. Nord, R. Ogando, J. Olsen, N. Palaio, K. Patton, J. Peoples, A. A. Plazas, J. Rauch, K. Reil, J.-P. Rheault, N. A. Roe, H. Rogers, A. Roodman, E. Sanchez, V. Scarpine, R. H. Schindler, R. Schmidt, R. Schmitt, M. Schubnell, K. Schultz, P. Schurter, L. Scott, S. Serrano, T. M. Shaw, R. C. Smith, M. Soares-Santos, A. Stefanik, W. Stuermer, E. Suchyta, A. Sypniewski, G. Tarle, J. Thaler, R. Tighe, C. Tran, D. Tucker, A. R. Walker, G. Wang, M. Watson, C. Weaverdyck, W. Wester, R. Woods, and B. Y. and THE DARK ENERGY CAMERA. *The Astronomical Journal*, 150(5):150, oct 2015.

- [33] D. Foreman-Mackey, W. Farr, M. Sinha, A. Archibald, D. Hogg, J. Sanders, J. Zuntz, P. Williams, A. Nelson, M. de Val-Borro, T. Erhardt, I. Pashchenko,

- and O. Pla. emcee v3: A Python ensemble sampling toolkit for affine-invariant MCMC. *The Journal of Open Source Software*, 4(43):1864, Nov. 2019.
- [34] M. C. Fortuna, H. Hoekstra, B. Joachimi, H. Johnston, N. E. Chisari, C. Georgiou, and C. Mahony. The halo model as a versatile tool to predict intrinsic alignments. *arXiv e-prints*, page arXiv:2003.02700, Mar. 2020.
- [35] J. A. Frieman, M. S. Turner, and D. Huterer. Dark energy and the accelerating universe. *Annual Review of Astronomy and Astrophysics*, 46(1):385–432, 2008.
- [36] García-Ruiz, I., Sancisi, R., and Kuijken, K. Neutral hydrogen and optical observations of edge-on galaxies: Hunting for warps\*. *A&A*, 394(3):769–789, 2002.
- [37] S. Ghigna, B. Moore, F. Governato, G. Lake, T. Quinn, and J. Stadel. Dark matter haloes within clusters. , 300:146–162, Oct. 1998.
- [38] O. Y. Gnedin and J. P. Ostriker. Limits on Collisional Dark Matter from Elliptical Galaxies in Clusters. , 561(1):61–68, Nov. 2001.
- [39] W. J. Handley, M. P. Hobson, and A. N. Lasenby. POLYCHORD: next-generation nested sampling. , 453(4):4384–4398, Nov. 2015.
- [40] D. Harvey, R. Massey, T. Kitching, A. Taylor, and E. Tittley. The non-gravitational interactions of dark matter in colliding galaxy clusters. *Science*, 347(6229):1462–1465, Mar. 2015.



- [41] L. Hernquist. An analytical model for spherical galaxies and bulges. , 356:359–364, June 1990.
- [42] C. Hikage, M. Oguri, T. Hamana, S. More, R. Mandelbaum, M. Takada, F. Köhlinger, H. Miyatake, A. J. Nishizawa, H. Aihara, R. Armstrong, J. Bosch, J. Coupon, A. Ducout, P. Ho, B.-C. Hsieh, Y. Komiyama, F. Lanusse, A. Leauthaud, R. H. Lupton, E. Medezinski, S. Mineo, S. Miyama, S. Miyazaki, R. Murata, H. Murayama, M. Shirasaki, C. Sifón, M. Simet, J. Speagle, D. N. Spergel, M. A. Strauss, N. Sugiyama, M. Tanaka, Y. Utsumi, S.-Y. Wang, and Y. Yamada. Cosmology from cosmic shear power spectra with Subaru Hyper Suprime-Cam first-year data. , 71(2):43, Apr. 2019.
- [43] H. Hildebrandt, F. Köhlinger, J. L. van den Busch, B. Joachimi, C. Heymans, A. Kannawadi, A. H. Wright, M. Asgari, C. Blake, H. Hoekstra, S. Joudaki, K. Kuijken, L. Miller, C. B. Morrison, T. Tröster, A. Amon, M. Archidiacono, S. Brieden, A. Choi, J. T. A. de Jong, T. Erben, B. Giblin, A. Mead, J. A. Peacock, M. Radovich, P. Schneider, C. Sifón, and M. Tewes. KiDS+VIKING-450: Cosmic shear tomography with optical and infrared data. , 633:A69, Jan. 2020.
- [44] H. Hildebrandt, M. Viola, C. Heymans, S. Joudaki, K. Kuijken, C. Blake, T. Erben, B. Joachimi, D. Klaes, L. Miller, C. B. Morrison, R. Naka-

- jima, G. Verdoes Kleijn, A. Amon, A. Choi, G. Covone, J. T. A. de Jong, A. Dvornik, I. Fenech Conti, A. Grado, J. Harnois-Déraps, R. Herbonnet, H. Hoekstra, F. Köhlinger, J. McFarland, A. Mead, J. Merten, N. Napolitano, J. A. Peacock, M. Radovich, P. Schneider, P. Simon, E. A. Valentijn, J. L. van den Busch, E. van Uitert, and L. Van Waerbeke. KiDS-450: cosmological parameter constraints from tomographic weak gravitational lensing. *Monthly Notices of the Royal Astronomical Society*, 465(2):1454–1498, 10 2016.
- [45] C. M. Hirata, R. Mandelbaum, M. Ishak, U. Seljak, R. Nichol, K. A. Pimbblet, N. P. Ross, and D. Wake. Intrinsic galaxy alignments from the 2SLAQ and SDSS surveys: luminosity and redshift scalings and implications for weak lensing surveys. , 381(3):1197–1218, Nov. 2007.
- [46] C. M. Hirata and U. Seljak. Intrinsic alignment-lensing interference as a contaminant of cosmic shear. , 70(6):063526, Sept. 2004.
- [47] P. F. Hopkins. A new class of accurate, mesh-free hydrodynamic simulation methods. , 450:53–110, June 2015.
- [48] B. Hoyle, D. Gruen, G. M. Bernstein, M. M. Rau, J. De Vicente, W. G. Hartley, E. Gaztanaga, J. DeRose, M. A. Troxel, C. Davis, A. Alarcon, N. MacCrann, J. Prat, C. Sánchez, E. Sheldon, R. H. Wechsler, J. Asorey, M. R. Becker, C. Bonnett, A. C. Rosell, D. Carollo, M. C. Kind, F. J. Castander, R. Cawthon, C. Chang, M. Childress, T. M. Davis, A. Drlica-Wagner,

M. Gatti, K. Glazebrook, J. Gschwend, S. R. Hinton, J. K. Hoormann, A. G. Kim, A. King, K. Kuehn, G. Lewis, C. Lidman, H. Lin, E. Macaulay, M. A. G. Maia, P. Martini, D. Mudd, A. Möller, R. C. Nichol, R. L. C. Ogando, R. P. Rollins, A. Roodman, A. J. Ross, E. Rozo, E. S. Rykoff, S. Samuroff, I. Sevilla-Noarbe, R. Sharp, N. E. Sommer, B. E. Tucker, S. A. Uddin, T. N. Varga, P. Vielzeuf, F. Yuan, B. Zhang, T. M. C. Abbott, F. B. Abdalla, S. Allam, J. Annis, K. Bechtol, A. Benoit-Lévy, E. Bertin, D. Brooks, E. Buckley-Geer, D. L. Burke, M. T. Busha, D. Capozzi, J. Carretero, M. Crocce, C. B. D’Andrea, L. N. da Costa, D. L. DePoy, S. Desai, H. T. Diehl, P. Doel, T. F. Eifler, J. Estrada, A. E. Evrard, E. Fernandez, B. Flaugher, P. Fosalba, J. Frieman, J. García-Bellido, D. W. Gerdes, T. Giannantonio, D. A. Goldstein, R. A. Gruendl, G. Gutierrez, K. Honscheid, D. J. James, M. Jarvis, T. Jeltema, M. W. G. Johnson, M. D. Johnson, D. Kirk, E. Krause, S. Kuhlmann, N. Kuropatkin, O. Lahav, T. S. Li, M. Lima, M. March, J. L. Marshall, P. Melchior, F. Menanteau, R. Miquel, B. Nord, C. R. O’Neill, A. A. Plazas, A. K. Romer, M. Sako, E. Sanchez, B. Santiago, V. Scarpine, R. Schindler, M. Schubnell, M. Smith, R. C. Smith, M. Soares-Santos, F. Sobreira, E. Suchyta, M. E. C. Swanson, G. Tarle, D. Thomas, D. L. Tucker, V. Vikram, A. R. Walker, J. Weller, W. Wester, R. C. Wolf, B. Yanny, J. Zuntz, and D. Collaboration. Dark Energy Survey Year 1 Results: redshift distributions of the weak-lensing source galaxies. *Monthly Notices of*

*the Royal Astronomical Society*, 478(1):592–610, 04 2018.

- [49] E. Hubble. A Relation between Distance and Radial Velocity among Extra-Galactic Nebulae. *Proceedings of the National Academy of Science*, 15(3):168–173, Mar. 1929.
- [50] E. Huff and R. Mandelbaum. Metacalibration: Direct Self-Calibration of Biases in Shear Measurement. *arXiv e-prints*, page arXiv:1702.02600, Feb. 2017.
- [51] M. Jarvis, G. Bernstein, and B. Jain. The skewness of the aperture mass statistic. , 352(1):338–352, July 2004.
- [52] B. Joachimi, P. Schneider, and T. Eifler. Analysis of two-point statistics of cosmic shear. III. Covariances of shear measures made easy. , 477(1):43–54, Jan. 2008.
- [53] S. Joudaki, C. Blake, A. Johnson, A. Amon, M. Asgari, A. Choi, T. Erben, K. Glazebrook, J. Harnois-Déraps, C. Heymans, H. Hildebrandt, H. Hoekstra, D. Klaes, K. Kuijken, C. Lidman, A. Mead, L. Miller, D. Parkinson, G. B. Poole, P. Schneider, M. Viola, and C. Wolf. KiDS-450 + 2dFLenS: Cosmological parameter constraints from weak gravitational lensing tomography and overlapping redshift-space galaxy clustering. *Monthly Notices of the Royal Astronomical Society*, 474(4):4894–4924, 10 2017.

- [54] F. Kahlhoefer, K. Schmidt-Hoberg, M. T. Frandsen, and S. Sarkar. Colliding clusters and dark matter self-interactions. *Monthly Notices of the Royal Astronomical Society*, 437(3):2865–2881, 11 2013.
- [55] F. Kahlhoefer, K. Schmidt-Hoberg, J. Kummer, and S. Sarkar. On the interpretation of dark matter self-interactions in Abell 3827. *Monthly Notices of the Royal Astronomical Society: Letters*, 452(1):L54–L58, 07 2015.
- [56] R. E. Kass and A. E. Raftery. Bayes factors. *Journal of the American Statistical Association*, 90(430):773–795, 1995.
- [57] S. Y. Kim, A. H. G. Peter, and D. Wittman. In the wake of dark giants: new signatures of dark matter self-interactions in equal-mass mergers of galaxy clusters. , 469(2):1414–1444, Aug. 2017.
- [58] E. Krause and T. Eifler. cosmolike - cosmological likelihood analyses for photometric galaxy surveys. , 470(2):2100–2112, Sept. 2017.
- [59] E. Krause, T. F. Eifler, J. Zuntz, O. Friedrich, M. A. Troxel, S. Dodelson, J. Blazek, L. F. Secco, N. MacCrann, E. Baxter, C. Chang, N. Chen, M. Crocce, J. DeRose, A. Ferte, N. Kokron, F. Lacasa, V. Miranda, Y. Omori, A. Porredon, R. Rosenfeld, S. Samuroff, M. Wang, R. H. Wechsler, T. M. C. Abbott, F. B. Abdalla, S. Allam, J. Annis, K. Bechtol, A. Benoit-Levy, G. M. Bernstein, D. Brooks, D. L. Burke, D. Capozzi, M. Carrasco Kind, J. Carretero, C. B. D’Andrea, L. N. da Costa, C. Davis, D. L. DePoy, S. Desai,

H. T. Diehl, J. P. Dietrich, A. E. Evrard, B. Flaugher, P. Fosalba, J. Frieman, J. Garcia-Bellido, E. Gaztanaga, T. Giannantonio, D. Gruen, R. A. Gruendl, J. Gschwend, G. Gutierrez, K. Honscheid, D. J. James, T. Jeltema, K. Kuehn, S. Kuhlmann, O. Lahav, M. Lima, M. A. G. Maia, M. March, J. L. Marshall, P. Martini, F. Menanteau, R. Miquel, R. C. Nichol, A. A. Plazas, A. K. Romer, E. S. Rykoff, E. Sanchez, V. Scarpine, R. Schindler, M. Schubnell, I. Sevilla-Noarbe, M. Smith, M. Soares-Santos, F. Sobreira, E. Suchyta, M. E. C. Swanson, G. Tarle, D. L. Tucker, V. Vikram, A. R. Walker, and J. Weller. Dark Energy Survey Year 1 Results: Multi-Probe Methodology and Simulated Likelihood Analyses. *arXiv e-prints*, page arXiv:1706.09359, June 2017.

- [60] J. Kummer, F. Kahlhoefer, and K. Schmidt-Hoberg. Effective description of dark matter self-interactions in small dark matter haloes. *ArXiv e-prints*, June 2017.
- [61] J. Kummer, F. Kahlhoefer, and K. Schmidt-Hoberg. Effective description of dark matter self-interactions in small dark matter haloes. , 474(1):388–399, Feb. 2018.
- [62] C. Laigle, H. J. McCracken, O. Ilbert, B. C. Hsieh, I. Davidzon, P. Capak, G. Hasinger, J. D. Silverman, C. Pichon, J. Coupon, H. Aussel, D. Le Borgne, K. Caputi, P. Cassata, Y. Y. Chang, F. Civano, J. Dunlop, J. Fynbo, J. S.

- Kartaltepe, A. Koekemoer, O. Le Fèvre, E. Le Floch, A. Leauthaud, S. Lilly, L. Lin, S. Marchesi, B. Milvang-Jensen, M. Salvato, D. B. Sanders, N. Scoville, V. Smolcic, M. Stockmann, Y. Taniguchi, L. Tasca, S. Toft, M. Vaccari, and J. Zabl. The COSMOS2015 Catalog: Exploring the  $1 < z < 6$  Universe with Half a Million Galaxies. , 224(2):24, June 2016.
- [63] E. V. Linder. Exploring the Expansion History of the Universe. , 90(9):091301, Mar. 2003.
- [64] L. Lombriser and A. Taylor. Breaking a dark degeneracy with gravitational waves. *Journal of Cosmology and Astroparticle Physics*, 2016(03):031–031, Mar 2016.
- [65] M. Markevitch, A. H. Gonzalez, D. Clowe, A. Vikhlinin, W. Forman, C. Jones, S. Murray, and W. Tucker. Direct Constraints on the Dark Matter Self-Interaction Cross Section from the Merging Galaxy Cluster 1E 0657-56. , 606(2):819–824, May 2004.
- [66] I. G. McCarthy, J. Schaye, T. J. Ponman, R. G. Bower, C. M. Booth, C. D. Vecchia, R. A. Crain, V. Springel, T. Theuns, and R. P. C. Wiersma. The case for AGN feedback in galaxy groups. *Monthly Notices of the Royal Astronomical Society*, 406(2):822–839, 07 2010.
- [67] J. E. McEwen, X. Fang, C. M. Hirata, and J. A. Blazek. FAST-PT: a novel algorithm to calculate convolution integrals in cosmological perturbation the-

- ory. , 2016(9):015, Sept. 2016.
- [68] J. Miralda-Escude. A test of the collisional dark matter hypothesis from cluster lensing. *The Astrophysical Journal*, 564(1):60–64, jan 2002.
- [69] M. Miyamoto and R. Nagai. Three-dimensional models for the distribution of mass in galaxies. , 27:533–543, 1975.
- [70] J. F. Navarro, C. S. Frenk, and S. D. M. White. The Structure of Cold Dark Matter Halos. , 462:563, May 1996.
- [71] J. F. Navarro, C. S. Frenk, and S. D. M. White. A Universal Density Profile from Hierarchical Clustering. , 490(2):493–508, Dec. 1997.
- [72] S. Paulin-Henriksson, A. Amara, L. Voigt, A. Refregier, and S. L. Bridle. Point spread function calibration requirements for dark energy from cosmic shear. , 484(1):67–77, June 2008.
- [73] S. Perlmutter, G. Aldering, G. Goldhaber, R. A. Knop, P. Nugent, P. G. Castro, S. Deustua, S. Fabbro, A. Goobar, D. E. Groom, and et al. Measurements of  $\Omega_m$  and  $\Omega_\Lambda$  from 42 high-redshift supernovae. *The Astrophysical Journal*, 517(2):565–586, Jun 1999.
- [74] A. H. G. Peter, M. Rocha, J. S. Bullock, and M. Kaplinghat. Cosmological simulations with self-interacting dark matter – II. Halo shapes versus obser-



vations. *Monthly Notices of the Royal Astronomical Society*, 430(1):105–120, 01 2013.

- [75] Planck Collaboration, Ade, P. A. R., Aghanim, N., Arnaud, M., Ashdown, M., Aumont, J., Baccigalupi, C., Banday, A. J., Barreiro, R. B., Bartlett, J. G., Bartolo, N., Battaner, E., Battye, R., Benabed, K., Benoît, A., Benoit-Lévy, A., Bernard, J.-P., Bersanelli, M., Bielewicz, P., Bock, J. J., Bonaldi, A., Bonavera, L., Bond, J. R., Borrill, J., Bouchet, F. R., Boulanger, F., Bucher, M., Burigana, C., Butler, R. C., Calabrese, E., Cardoso, J.-F., Catalano, A., Challinor, A., Chamballu, A., Chary, R.-R., Chiang, H. C., Chluba, J., Christensen, P. R., Church, S., Clements, D. L., Colombi, S., Colombo, L. P. L., Combet, C., Coulais, A., Crill, B. P., Curto, A., Cuttaia, F., Danese, L., Davies, R. D., Davis, R. J., de Bernardis, P., de Rosa, A., de Zotti, G., Delabrouille, J., Désert, F.-X., Di Valentino, E., Dickinson, C., Diego, J. M., Dolag, K., Dole, H., Donzelli, S., Doré, O., Douspis, M., Ducout, A., Dunkley, J., Dupac, X., Efstathiou, G., Elsner, F., Enßlin, T. A., Eriksen, H. K., Farhang, M., Fergusson, J., Finelli, F., Forni, O., Frailis, M., Fraisse, A. A., Franceschi, E., Frejsel, A., Galeotta, S., Galli, S., Ganga, K., Gauthier, C., Gerbino, M., Ghosh, T., Giard, M., Giraud-Héraud, Y., Giusarma, E., Gjerløw, E., González-Nuevo, J., Górski, K. M., Gratton, S., Gregorio, A., Gruppuso, A., Gudmundsson, J. E., Hamann, J., Hansen, F. K., Hanson, D., Harrison, D. L., Helou, G., Henrot-Versillé, S., Hernández-Monteagudo,

C., Herranz, D., Hildebrandt, S. R., Hivon, E., Hobson, M., Holmes, W. A., Hornstrup, A., Hovest, W., Huang, Z., Huppenberger, K. M., Hurier, G., Jaffe, A. H., Jaffe, T. R., Jones, W. C., Juvela, M., Keihänen, E., Keskitalo, R., Kisner, T. S., Kneissl, R., Knoche, J., Knox, L., Kunz, M., Kurki-Suonio, H., Lagache, G., Lähteenmäki, A., Lamarre, J.-M., Lasenby, A., Lattanzi, M., Lawrence, C. R., Leahy, J. P., Leonardi, R., Lesgourgues, J., Levrier, F., Lewis, A., Liguori, M., Lilje, P. B., Linden-Vørnle, M., López-Caniego, M., Lubin, P. M., Macías-Pérez, J. F., Maggio, G., Maino, D., Mandolesi, N., Mangilli, A., Marchini, A., Maris, M., Martin, P. G., Martinelli, M., Martínez-González, E., Masi, S., Matarrese, S., McGehee, P., Meinhold, P. R., Melchiorri, A., Melin, J.-B., Mendes, L., Mennella, A., Migliaccio, M., Millea, M., Mitra, S., Miville-Deschênes, M.-A., Moneti, A., Montier, L., Morgante, G., Mortlock, D., Moss, A., Munshi, D., Murphy, J. A., Naselsky, P., Nati, F., Natoli, P., Netterfield, C. B., Nørgaard-Nielsen, H. U., Noviello, F., Novikov, D., Novikov, I., Oxborrow, C. A., Paci, F., Pagano, L., Pajot, F., Paladini, R., Paoletti, D., Partridge, B., Pasian, F., Patanchon, G., Pearson, T. J., Perdureau, O., Perotto, L., Perrotta, F., Pettorino, V., Piacentini, F., Piat, M., Pierpaoli, E., Pietrobon, D., Plaszczynski, S., Pointecouteau, E., Polenta, G., Popa, L., Pratt, G. W., Prézeau, G., Prunet, S., Puget, J.-L., Rachen, J. P., Reach, W. T., Rebolo, R., Reinecke, M., Remazeilles, M., Renault, C., Renzi, A., Ristorcelli, I., Rocha, G., Rosset, C., Rossetti, M.,

Roudier, G., Rouillé d'Orfeuil, B., Rowan-Robinson, M., Rubiño-Martín, J. A., Rusholme, B., Said, N., Salvatelli, V., Salvati, L., Sandri, M., Santos, D., Savelainen, M., Savini, G., Scott, D., Seiffert, M. D., Serra, P., Shellard, E. P. S., Spencer, L. D., Spinelli, M., Stolyarov, V., Stompor, R., Sudiwala, R., Sunyaev, R., Sutton, D., Suur-Uski, A.-S., Sygnet, J.-F., Tauber, J. A., Terenzi, L., Toffolatti, L., Tomasi, M., Tristram, M., Trombetti, T., Tucci, M., Tuovinen, J., Türler, M., Umana, G., Valenziano, L., Valiviita, J., Van Tent, F., Vielva, P., Villa, F., Wade, L. A., Wandelt, B. D., Wehus, I. K., White, M., White, S. D. M., Wilkinson, A., Yvon, D., Zacchei, A., and Zonca, A. Planck 2015 results - xiii. cosmological parameters. *A&A*, 594:A13, 2016.

- [76] S. W. Randall, M. Markevitch, D. Clowe, A. H. Gonzalez, and M. Bradač. Constraints on the Self-Interaction Cross Section of Dark Matter from Numerical Simulations of the Merging Galaxy Cluster 1E 0657-56. , 679(2):1173–1180, June 2008.
- [77] V. Reshetnikov and F. Combes. Statistics of optical WARPS in spiral disks. , 337:9–16, Sept. 1998.
- [78] A. G. Riess, A. V. Filippenko, P. Challis, A. Clocchiatti, A. Diercks, P. M. Garnavich, R. L. Gilliland, C. J. Hogan, S. Jha, R. P. Kirshner, B. Leibundgut, M. M. Phillips, D. Reiss, B. P. Schmidt, R. A. Schommer, R. C. Smith, J. Spyromilio, C. Stubbs, N. B. Suntzeff, and J. Tonry. Observational

Evidence from Supernovae for an Accelerating Universe and a Cosmological Constant. , 116(3):1009–1038, Sept. 1998.

- [79] M. Rocha, A. H. G. Peter, J. S. Bullock, M. Kaplinghat, S. Garrison-Kimmel, J. Oñorbe, and L. A. Moustakas. Cosmological simulations with self-interacting dark matter – I. Constant-density cores and substructure. *Monthly Notices of the Royal Astronomical Society*, 430(1):81–104, 01 2013.
- [80] B. Rowe. Improving PSF modelling for weak gravitational lensing using new methods in model selection. *Monthly Notices of the Royal Astronomical Society*, 404(1):350–366, 04 2010.
- [81] J. Sakstein and B. Jain. Implications of the Neutron Star Merger GW170817 for Cosmological Scalar-Tensor Theories. , 119(25):251303, Dec. 2017.
- [82] S. Samuroff, J. Blazek, M. A. Troxel, N. MacCrann, E. Krause, C. D. Leonard, J. Prat, D. Gruen, S. Dodelson, T. F. Eifler, M. Gatti, W. G. Hartley, B. Hoyle, P. Larsen, J. Zuntz, T. M. C. Abbott, S. Allam, J. Annis, G. M. Bernstein, E. Bertin, S. L. Bridle, D. Brooks, A. Carnero Rosell, M. Carrasco Kind, J. Carretero, F. J. Castander, C. E. Cunha, L. N. da Costa, C. Davis, J. De Vicente, D. L. DePoy, S. Desai, H. T. Diehl, J. P. Dietrich, P. Doel, B. Flaugher, P. Fosalba, J. Frieman, J. García-Bellido, E. Gaztanaga, D. W. Gerdes, R. A. Gruendl, J. Gschwend, G. Gutierrez, D. L. Hollowood, K. Honscheid, D. J. James, K. Kuehn, N. Kuropatkin, M. Lima,

- M. A. G. Maia, M. March, J. L. Marshall, P. Martini, P. Melchior, F. Menanteau, C. J. Miller, R. Miquel, R. L. C. Ogando, A. A. Plazas, E. Sanchez, V. Scarpine, R. Schindler, M. Schubnell, S. Serrano, I. Sevilla-Noarbe, E. Sheldon, M. Smith, F. Sobreira, E. Suchyta, G. Tarle, D. Thomas, V. Vikram, and DES Collaboration. Dark Energy Survey Year 1 results: constraints on intrinsic alignments and their colour dependence from galaxy clustering and weak lensing. *MNRAS*, 489(4):5453–5482, Nov. 2019.
- [83] J. Schaye, C. Dalla Vecchia, C. M. Booth, R. P. C. Wiersma, T. Theuns, M. R. Haas, S. Bertone, A. R. Duffy, I. G. McCarthy, and F. van de Voort. The physics driving the cosmic star formation history. *MNRAS*, 402(3):1536–1560, Mar. 2010.
- [84] D. M. Schmitz, C. M. Hirata, J. Blazek, and E. Krause. Time evolution of intrinsic alignments of galaxies. *MNRAS*, 2018(7):030, July 2018.
- [85] P. Schneider, L. van Waerbeke, and Y. Mellier. B-modes in cosmic shear from source redshift clustering. *MNRAS*, 389:729–741, July 2002.
- [86] Schneider, P. and Lombardi, M. The three-point correlation function of cosmic shear - i. the natural components. *A&A*, 397(3):809–818, 2003.
- [87] Schneider, P., van Waerbeke, L., Kilbinger, M., and Mellier, Y. Analysis of two-point statistics of cosmic shear - i. estimators and covariances. *A&A*, 396(1):1–19, 2002.

- [88] D. M. Scolnic, D. O. Jones, A. Rest, Y. C. Pan, R. Chornock, R. J. Foley, M. E. Huber, R. Kessler, G. Narayan, A. G. Riess, and et al. The complete light-curve sample of spectroscopically confirmed sne ia from pan-starrs1 and cosmological constraints from the combined pantheon sample. *The Astrophysical Journal*, 859(2):101, May 2018.
- [89] L. F. Secco, A. Farah, B. Jain, S. Adhikari, A. Banerjee, and N. Dalal. Probing Self-interacting Dark Matter with Disk Galaxies in Cluster Environments. , 860(1):32, June 2018.
- [90] Z. Shang, Z. Zheng, E. Brinks, J. Chen, D. Burstein, H. Su, Yong-ik Byun, L. Deng, Z. Deng, X. Fan, Z. Jiang, Y. Li, W. Lin, F. Ma, Wei-hsin Sun, B. Wills, R. A. Windhorst, H. Wu, X. Xia, W. Xu, S. Xue, H. Yan, Xu Zhou, J. Zhu, and Z. Zou. Ring Structure and Warp of NGC 5907: Interaction with Dwarf Galaxies. *The Astrophysical Journal Letters*, 504(1):L23, 1998.
- [91] E. S. Sheldon and E. M. Huff. Practical weak-lensing shear measurement with metacalibration. *The Astrophysical Journal*, 841(1):24, may 2017.
- [92] A. Silvestri, L. Pogosian, and R. V. Buniy. Practical approach to cosmological perturbations in modified gravity. *Physical Review D*, 87(10), May 2013.
- [93] F. Simpson, C. Heymans, D. Parkinson, C. Blake, M. Kilbinger, J. Benjamin, T. Erben, H. Hildebrandt, H. Hoekstra, T. D. Kitching, and et al. Cfhtlens: testing the laws of gravity with tomographic weak lensing and

- redshift-space distortions. *Monthly Notices of the Royal Astronomical Society*, 429(3):2249–2263, Dec 2012.
- [94] R. E. Smith, J. A. Peacock, A. Jenkins, S. D. M. White, C. S. Frenk, F. R. Pearce, P. A. Thomas, G. Efstathiou, and H. M. P. Couchman. Stable clustering, the halo model and non-linear cosmological power spectra. , 341(4):1311–1332, June 2003.
- [95] D. N. Spergel and P. J. Steinhardt. Observational Evidence for Self-Interacting Cold Dark Matter. , 84(17):3760–3763, Apr. 2000.
- [96] V. Springel. The cosmological simulation code GADGET-2. , 364:1105–1134, Dec. 2005.
- [97] V. Springel, T. Di Matteo, and L. Hernquist. Modelling feedback from stars and black holes in galaxy mergers. , 361:776–794, Aug. 2005.
- [98] M. Takada and B. Jain. The impact of non-Gaussian errors on weak lensing surveys. , 395(4):2065–2086, June 2009.
- [99] R. Takahashi, M. Sato, T. Nishimichi, A. Taruya, and M. Oguri. Revising the Halofit Model for the Nonlinear Matter Power Spectrum. , 761(2):152, Dec. 2012.
- [100] A. Toomre. On the gravitational stability of a disk of stars. , 139:1217–1238, May 1964.

[101] M. A. Troxel, N. MacCrann, J. Zuntz, T. F. Eifler, E. Krause, S. Dodelson, D. Gruen, J. Blazek, O. Friedrich, S. Samuroff, J. Prat, L. F. Secco, C. Davis, A. Ferté, J. DeRose, A. Alarcon, A. Amara, E. Baxter, M. R. Becker, G. M. Bernstein, S. L. Bridle, R. Cawthon, C. Chang, A. Choi, J. De Vicente, A. Drlica-Wagner, J. Elvin-Poole, J. Frieman, M. Gatti, W. G. Hartley, K. Honscheid, B. Hoyle, E. M. Huff, D. Huterer, B. Jain, M. Jarvis, T. Kacprzak, D. Kirk, N. Kokron, C. Krawiec, O. Lahav, A. R. Liddle, J. Peacock, M. M. Rau, A. Refregier, R. P. Rollins, E. Rozo, E. S. Rykoff, C. Sánchez, I. Sevilla-Noarbe, E. Sheldon, A. Stebbins, T. N. Varga, P. Vielzeuf, M. Wang, R. H. Wechsler, B. Yanny, T. M. C. Abbott, F. B. Abdalla, S. Allam, J. Annis, K. Bechtol, A. Benoit-Lévy, E. Bertin, D. Brooks, E. Buckley-Geer, D. L. Burke, A. Carnero Rosell, M. Carrasco Kind, J. Carretero, F. J. Castander, M. Crocce, C. E. Cunha, C. B. D'Andrea, L. N. da Costa, D. L. DePoy, S. Desai, H. T. Diehl, J. P. Dietrich, P. Doel, E. Fernandez, B. Flaugher, P. Fosalba, J. García-Bellido, E. Gaztanaga, D. W. Gerdes, T. Giannantonio, D. A. Goldstein, R. A. Gruendl, J. Gschwend, G. Gutierrez, D. J. James, T. Jeltema, M. W. G. Johnson, M. D. Johnson, S. Kent, K. Kuehn, S. Kuhlmann, N. Kuropatkin, T. S. Li, M. Lima, H. Lin, M. A. G. Maia, M. March, J. L. Marshall, P. Martini, P. Melchior, F. Menanteau, R. Miquel, J. J. Mohr, E. Neilsen, R. C. Nichol, B. Nord, D. Petravick, A. A. Plazas, A. K. Romer, A. Roodman, M. Sako, E. Sanchez, V. Scarpine,



- R. Schindler, M. Schubnell, M. Smith, R. C. Smith, M. Soares-Santos, F. Sobreira, E. Suchyta, M. E. C. Swanson, G. Tarle, D. Thomas, D. L. Tucker, V. Vikram, A. R. Walker, J. Weller, Y. Zhang, and DES Collaboration. Dark Energy Survey Year 1 results: Cosmological constraints from cosmic shear. , 98(4):043528, Aug. 2018.
- [102] T. M. Tugendhat and B. M. Schäfer. Angular ellipticity correlations in a composite alignment model for elliptical and spiral galaxies and inference from weak lensing. , 476(3):3460–3477, May 2018.
- [103] S. Tulin and H.-B. Yu. Dark matter self-interactions and small scale structure. , 730:1–57, Feb. 2018.
- [104] M. P. van Daalen, J. Schaye, C. M. Booth, and C. Dalla Vecchia. The effects of galaxy formation on the matter power spectrum: a challenge for precision cosmology. *Monthly Notices of the Royal Astronomical Society*, 415(4):3649–3665, 08 2011.
- [105] F. C. van den Bosch, G. Ogiya, O. Hahn, and A. Burkert. Disruption of Dark Matter Substructure: Fact or Fiction? *ArXiv e-prints*, 2017.
- [106] V. Vikram, A. Cabré, B. Jain, and J. VanderPlas. Astrophysical tests of modified gravity: the morphology and kinematics of dwarf galaxies. *Journal of Cosmology and Astroparticle Physics*, 2013(08):020, 2013.

- [107] Z. Vlah, N. E. Chisari, and F. Schmidt. An EFT description of galaxy intrinsic alignments. *Phys. Rev. D*, 2020(1):025, Jan. 2020.
- [108] D. H. Weinberg, M. J. Mortonson, D. J. Eisenstein, C. Hirata, A. G. Riess, and E. Rozo. Observational probes of cosmic acceleration. *Physics Reports*, 530(2):87 – 255, 2013. Observational Probes of Cosmic Acceleration.
- [109] D. M. Wittman, J. A. Tyson, D. Kirkman, I. Dell’Antonio, and G. Bernstein. Detection of weak gravitational lensing distortions of distant galaxies by cosmic dark matter at large scales. *Astron. J.*, 405(6783):143–148, May 2000.
- [110] H. S. Xavier, F. B. Abdalla, and B. Joachimi. Improving lognormal models for cosmological fields. *MNRAS*, 459(4):3693–3710, July 2016.
- [111] D. Yurin and V. Springel. An iterative method for the construction of N-body galaxy models in collisionless equilibrium. *MNRAS*, 444:62–79, Oct. 2014.
- [112] J. Zuntz, M. Paterno, E. Jennings, D. Rudd, A. Manzotti, S. Dodelson, S. Bridle, S. Sehrish, and J. Kowalkowski. CosmoSIS: Modular cosmological parameter estimation. *Astronomy and Computing*, 12:45–59, Sept. 2015.
- [113] J. Zuntz, E. Sheldon, S. Samuroff, M. A. Troxel, M. Jarvis, N. MacCrann, D. Gruen, J. Prat, C. Sánchez, A. Choi, S. L. Bridle, G. M. Bernstein, S. Dodelson, A. Drlica-Wagner, Y. Fang, R. A. Gruendl, B. Hoyle, E. M. Huff, B. Jain, D. Kirk, T. Kacprzak, C. Krawiec, A. A. Plazas, R. P. Rollins,

E. S. Rykoff, I. Sevilla-Noarbe, B. Soergel, T. N. Varga, T. M. C. Abbott, F. B. Abdalla, S. Allam, J. Annis, K. Bechtol, A. Benoit-Lévy, E. Bertin, E. Buckley-Geer, D. L. Burke, A. Carnero Rosell, M. Carrasco Kind, J. Carretero, F. J. Castander, M. Crocce, C. E. Cunha, C. B. D’Andrea, L. N. da Costa, C. Davis, S. Desai, H. T. Diehl, J. P. Dietrich, P. Doel, T. F. Eifler, J. Estrada, A. E. Evrard, A. Fausti Neto, E. Fernandez, B. Flaugher, P. Fosalba, J. Frieman, J. García-Bellido, E. Gaztanaga, D. W. Gerdes, T. Giannantonio, J. Gschwend, G. Gutierrez, W. G. Hartley, K. Honscheid, D. J. James, T. Jeltema, M. W. G. Johnson, M. D. Johnson, K. Kuehn, S. Kuhlmann, N. Kuropatkin, O. Lahav, T. S. Li, M. Lima, M. A. G. Maia, M. March, P. Martini, P. Melchior, F. Menanteau, C. J. Miller, R. Miquel, J. J. Mohr, E. Neilsen, R. C. Nichol, R. L. C. Ogando, N. Roe, A. K. Romer, A. Roodman, E. Sanchez, V. Scarpine, R. Schindler, M. Schubnell, M. Smith, R. C. Smith, M. Soares-Santos, F. Sobreira, E. Suchyta, M. E. C. Swanson, G. Tarle, D. Thomas, D. L. Tucker, V. Vikram, A. R. Walker, R. H. Wechsler, Y. Zhang, and DES Collaboration. Dark Energy Survey Year 1 results: weak lensing shape catalogues. , 481(1):1149–1182, Nov. 2018.

- [114] F. Zwicky. Die Rotverschiebung von extragalaktischen Nebeln. *Helv. Phys. Acta*, 6:110–127, 1933.